

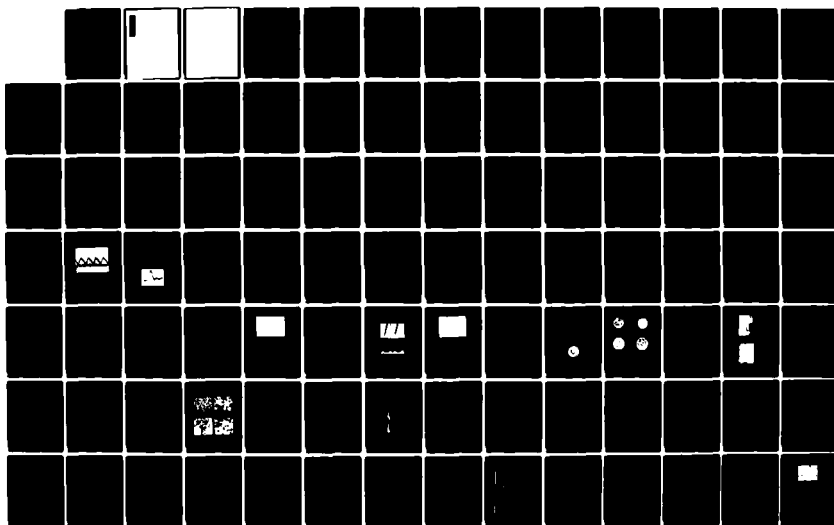
AD-A140 027

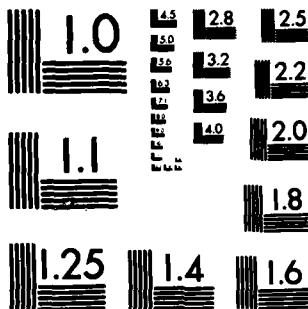
SOLID STATE RESEARCH(U) MASSACHUSETTS INST OF TECH
LEXINGTON LINCOLN LAB A L MCWHORTER 15 AUG 83 1983:3
ESD-TR-83-051 F19628-80-C-0002

1/ 2

UNCLASSIFIED

F/G 20/12 NL





MICROCOPY RESOLUTION TEST CHART
NATIONAL BUREAU OF STANDARDS-1963-A

AD A140027

**MASSACHUSETTS INSTITUTE OF TECHNOLOGY
LINCOLN LABORATORY**

SOLID STATE RESEARCH

QUARTERLY TECHNICAL SUMMARY REPORT

1 MAY — 31 JULY 1963

ISSUED 30 DECEMBER 1963

Approved for public release; distribution unlimited.

LEXINGTON

MASSACHUSETTS

ABSTRACT

This report covers in detail the solid state research work of the Solid State Division at Lincoln Laboratory for the period 1 May through 31 July 1983. The topics covered are Solid State Device Research, Quantum Electronics, Materials Research, Microelectronics, and Analog Device Technology. Funding is primarily provided by the Air Force, with additional support provided by the Army, DARPA, Navy, NASA, and DOE.

Accession For	
NTIS GRA&I	<input checked="" type="checkbox"/>
DTIC TAB	<input type="checkbox"/>
Unannounced	<input type="checkbox"/>
Justification	
By	
Distribution/	
Availability Codes	
Dist	Avail and/or Special
AI	



TABLE OF CONTENTS

Abstract	iii
List of Illustrations	vii
List of Tables	xi
Introduction	xiii
Reports on Solid State Research	xvii
Organization	xxxi
 1. SOLID STATE DEVICE RESEARCH,	 1
1.1 GaInAsP Buried-Heterostructure Waveguide Devices	1
1.2 Linearity Measurements of High-Speed InP Optoelectronic Switches	5
1.3 Continuous Multi-Gigahertz Modulation of Q-Switched GaInAsP Diode Lasers	11
1.4 Semi-insulating InGaAs Optoelectronic Switches	14
1.5 Broadly Tunable Mode-Locked HgCdTe Lasers	15
 2. QUANTUM ELECTRONICS,	 17
2.1 Ti:Al ₂ O ₃ Laser: Recent Advances	17
2.2 Gain in V:KMgF ₃	19
2.3 Continuous-Wave Actively Mode-Locked Co:MgF ₂ and Ni:MgF ₂ Lasers	23
2.4 UV Laser Photopolymerization of Volatile Surface-Adsorbed Methyl Methacrylate	28
2.5 Self-Developing UV Photoresist Using Excimer Laser Exposure	31
 3. MATERIALS RESEARCH,	 35
3.1 Zone-Melting Recrystallization of Si Films on SiO ₂ -Coated Si Substrates	35
3.2 Pd ₂ Si/Poly-Si Contacts for Si Devices	41
3.3 Plasma-Deposited Si ₃ N ₄ as an Oxidation Mask in the Fabrication of GaAs Solar Cells	47
3.4 Depth Profile of Traps Introduced by Dry Etching of GaAs	49

4. MICROELECTRONICS	61
4.1 A Technique for the Determination of Stress in Thin Films	61
4.2 Charge-Coupled Devices: Time Integrating Correlator	64
4.3 Submillimeter-Wave Mixers for Space Applications	68
4.4 Charge-Coupled Devices: Matrix-Matrix Product Device	71
5. ANALOG DEVICE TECHNOLOGY	79
5.1 Superconductive Ring Mixers	79
5.2 Convolver-Based Wideband Programmable Matched Filter	83

LIST OF ILLUSTRATIONS

Figure No.		Page
1-1	Schematic Illustration of Waveguide Fabrication Showing (a) Double-Heterostructure Wafer with Ti Etch Mask, (b) Wafer Following Selective Chemical Etching, and (c) Waveguide Sample Following LPE Regrowth	2
1-2	(a) Schematic Illustration of Waveguide Branch and (b) Measured Branch Transmission as a Function of Branch Angle θ	3
1-3	(a) Schematic Illustration of Waveguide Bend Structure and (b) Measured Transmission per Single Bend as a Function of Bend Angle ϕ	4
1-4	I-V Curves of InP Switch for Both Symmetric Illumination (Solid Curves) and Highly Asymmetric Illumination (Dashed Curve)	6
1-5	Block Diagram of Test Setup for Measuring Intermodulation Out- puts Produced by InP Switch	7
1-6	Plot of Three RF Outputs: The Fundamental, Second, and Third Order vs RF Inputs at 97 and 103 MHz. Laser Power Constant at 4.5 mW	8
1-7	Plot of Second- and Third-Order Intercept Points vs Frequency for Constant Laser Power of 4.5 mW	9
1-8	Plot of Second- and Third-Order Intercept Points vs Laser Power for Input Frequencies of 197 and 203 MHz	10
1-9	Schematic Cross Section of a Q-Switched Diode Laser. The Proton Bombarded Region Extends Below the Active Region to Isolate the Amplifier and the Modulator	12
1-10	Detected Output from a Q-Switched Diode Laser with a Proton- Isolated Modulator at 3 GHz. About 10 mW of Microwave Power Is Required for Full Off/On Modulation	13
1-11	Pulse Response of InGaAs:Fe Optoelectronic Switch to AlGaAs Laser ($\lambda = 0.86 \mu\text{m}$) Driven by a 100-MHz Comb Generator. Horizontal Scale Is 20 ps/div	14

Figure No.		Page
2-1	Output Energy vs Absorbed Input Energy for Pulsed $\text{Ti:Al}_2\text{O}_3$ Laser, for Two Different Output-Mirror Transmissions. The Pump and Laser Wavelengths were 587 and 750 nm, Respectively	18
2-2	Percentage Gain in V:KMgF_3 as a Function of Pump Power for a Chopper Frequency of 55 Hz. The Lighter Section of the Curve Is a Best-Fit Straight Line to the Points Shown	20
2-3	Gain and Fluorescence Signal Levels as a Function of Chopper Frequency, for Constant Pump Power	21
2-4	Plot of Pulse Width vs Wavelength for Co:MgF_2 Laser. The Two Datapoint Symbols Represent Data with Different Sets of Cavity Mirrors	24
2-5	Plot of Pulse Width vs Wavelength for Ni:MgF_2 Laser	25
2-6	Autocorrelation Trace of Shortest Pulse from the Co:MgF_2 Laser	26
2-7	Two-Component Adsorbed Multilayer Used in Laser Photopolymerization. The Volatile MMA Layers Equilibrate Rapidly with the MMA-Vapor Ambient	29
2-8	Electron Micrograph of Positive Relief in (100) Si. Laser-Deposited PMMA Was Used to Mask a Two-Step Wet and Dry Etching Sequence (See Text)	30
2-9	(Top) Optical Micrograph of a Grating Pattern in Nitrocellulose Obtained Using 193-nm ArF Laser Radiation and a $3.8\text{-}\mu\text{m}$ -Period Chrome-on-Quartz Mask Contacted to the Si Substrate. (Bottom) Grating Pattern Obtained When the Mask Is Spaced Away from the Substrate in Order to Obtain Spatial Period Division Effects	32
2-10	Optical Micrograph of a Grating Pattern in Nitrocellulose Produced by Diffraction from the Edge of a $100\text{-}\mu\text{m}$ -Thick Si Wafer Contacted to the Substrate	33
3-1	Interference Pattern Showing the Flatness of an SOI Sample Before Zone-Melting Recrystallization	35
3-2	Interference Patterns Showing the Flatness of an SOI Sample: (a) As Recrystallized; (b) Back-Side Lapped; (c) and (d) After High-Temperature Anneals	36
3-3	Photomicrographs of Recrystallized Si Films Illustrating the Correlation Between Protrusion Density and Sub-boundary Spacing	38

Figure No.		Page
3-4	Plot of Sub-boundary Spacing vs Protrusion Density. Data Points for 85 Percent of the Samples Examined Fall in the Shaded Region	39
3-5	Power Incident on a Sample from the Upper Strip Heater as a Function of Position X Along the Sample Surface. D Is the Heater-Sample Separation	40
3-6	RBS Spectra Showing Intermixing of Pd_2Si with (a) Undoped Poly-Si Film and (b) P-Doped Poly-Si Film	42
3-7	TEM Micrographs for (a) Undoped Poly-Si Film and (b) Doped Poly-Si Film	43
3-8	TEM Micrographs for Pd_2Si Formed on (a) Undoped Poly-Si Film and (b) Doped Poly-Si Film	43
3-9	Sheet Resistance of Pd_2Si /Poly-Si Layers as a Function of Annealing Temperature	44
3-10	Histogram of Leakage Current Density for Shallow-Junction Diodes with Pd_2Si /Poly-Si or Al/Poly-Si Contacts	46
3-11	Solar Cell Fabrication Procedure Using Si_3N_4 Protection Mask	50
3-12	Photocurrent Density as a Function of Voltage for GaAs Cell with 20-Percent Conversion Efficiency at AM1	51
3-13	Short-Circuit Current Density J_{sc} as a Function of Open-Circuit Voltage V_{oc} for a 0.0925-cm^2 Cell Fabricated on the Same Wafer as the Cell of Figure 3-12	52
3-14	Depth Profiles of Net Donor Concentration Deduced from C-V Measurements on a Control Sample (Solid Line) and a Sample Etched by Reactive-Ion Etching in CF_4 at 250 V Followed by Ar Ion Beam Etching at 500 V (Dashed Line)	54
3-15	Capacitance vs Temperature for a Back-Biased Schottky Diode for Various Values of Bias V_b	55
3-16	DLTS Signals $\Delta C/C$ for a 1-ms-Wide Filling Pulse, $V_p = 0.14\text{ V}$, and Various Values of Back Bias. Emission $\tau = 7.4\text{ ms}$	56

Figure No.		Page
3-17	DLTS Signals $\Delta C/C$ for Back Bias $V_p = 0.70$ V and 1-ms-Wide V_p Filling Pulses of 0.14 V (Solid Line) and 0.70 V (Dashed Line). Emission $\tau = 7.4$ ms	58
3-18	ODLTS Signals $\Delta C/C$ for $H\nu = 0.95$ μm and Various Values of Back Bias V_b . Emission $\tau = 7.8$ ms	59
4-1	Diagram of the Deflection of a Free-Standing Membrane Used for Stress Calculation	62
4-2	Bulge Test Data and Fit for LPCVD SiN_x Deposited at 850°C with a Gas Volume Ratio of 5:1 ($\text{SiH}_2\text{Cl}_2:\text{NH}_3$)	63
4-3	(a) Diagram of the Integrator and Skimming Circuits, (b) Potential Diagram When Integrator Gate Is High and Holding Gate Is Low, and (c) When Integrator Gate Is Low, Holding Gate Is High, and Charge Skimming Occurs	66
4-4	Example of Correlator Performance at a 20-MHz Clock Rate. Upper Trace Is a 511-Bit m-Sequence at 20 Mb/s and the Lower Trace Is the CCD Output at 1.4 MHz After Integrating for 511 Clock Periods (25.6 μs)	67
4-5	Illustration of a Method of Removing Pattern Noise Arising from Offsets	67
4-6	Experimental Demonstration of Pattern Noise Removal Technique of Figure 4-5. Upper Trace Is CCD Output of Two Successive Integration Periods. Lower Trace Is the Result of Subtracting the Second Half of the Upper Trace from the First Half	68
4-7	Corner Reflector Mixer Showing Location of Nanoliter Epoxy Droplet Bonding Whisker Antenna to GaAs Chip	69
4-8	Schematic of a General-Purpose MMP Device	72
4-9	Photomicrograph of a CCD MMP Device	73
4-10	Simulated Serial Radar Video Which Consists of 28 Returns, Each To Be Sampled into 32 Range-Cell Resolution. The Waveform Can Be Represented as $f_{nj} = -\cos(8\pi n/28)$ for $j = 4$, $j = 28$, and $0 \leq n \leq 27$; $f_{nj} = 0$ Otherwise	74
4-11	The Same Video as in Figure 4-10 Displayed in Two-Dimensional Format, with the Horizontal Axis Corresponding to Range Bins and the Vertical Axis to PRIs	74

Figure No.		Page
4-12	Discrete Cosine Transform of the Input Waveform Shown in Figure 4-10, Computed by the MMP Device. Serial Output Data Stream from the Device Is Displayed in Two-Dimensional Format (i.e., the Horizontal Axis Corresponds to Range Bin Resolution and the Vertical Axis to Doppler Resolution)	76
5-1	Cutoff Frequency of 50- Ω Mixer Rings as a Function of Individual Superconductive Junction Area	80
5-2	Schematic of the Diode Mixer Ring	80
5-3	Photograph of a 16-Junction Diode Mixer Ring	81
5-4	Current-Voltage Characteristic of a 16-Junction Ring Mixer at 4.2 K. Horizontal Scale Is 10 mV/div; Vertical Scale Is 0.1 mA/div	82
5-5	Diode Ring Output Level as a Function of Input Signal Level	82
5-6	Code Sequence Generator	84
5-7	Minimum-Shift-Keyed Modulator	85
5-8	Compressed Pulse Output of Convolver. Horizontal Scale: (a) 5 ns/div, (b) 50 ns/div	85

LIST OF TABLES

Table No.		Page
4-1	Experimental Data for Several Thin Films Deposited onto SiN _x Membranes	64

INTRODUCTION

1. SOLID STATE DEVICE RESEARCH

Low-loss single-mode GaInAsP optical waveguide branches and bends have been fabricated utilizing a buried-heterostructure geometry to achieve tight optical confinement. Branching losses as low as 0.4 dB have been obtained at 1.3 μm for branch angles of 1° .

The linearity of InP optoelectronic switches under constant semiconductor laser illumination is characterized by measurement of the second- and third-order intermodulation outputs. Correlation between the devices' I-V curve and intermodulation levels is obtained for variations in laser power, RF input frequency, and optical illumination symmetry.

GaInAsP diode lasers with a proton-isolated modulator have been operated with full on/off modulation at rates of 3 GHz. Both the gain and loss are actively varied in the modulator in order to Q-switch the laser.

The first high-speed semi-insulating InGaAs optoelectronic switches have been fabricated and evaluated at wavelengths up to 1.24 μm . They exhibit on-state resistance as low as 300 Ω and response times with FWHM equal to 40 ps. Material characteristics and performance of these photoconductive devices have been investigated.

Near-bandwidth-limited pulses of 6-ps duration lasing at $\lambda = 1.2 \mu\text{m}$ have been obtained from 4- to 8- μm -thick LPE HgCdTe layers which have been pumped longitudinally by a Nd:YAG laser. Tuning from $\lambda = 1.82$ to 2.0 μm via the Burstein-Moss shift has been accomplished on a single epilayer by varying the loss in the external cavity.

2. QUANTUM ELECTRONICS

A pulsed, laser-pumped Ti:Al₂O₃ laser has been operated with 50-percent quantum efficiency and has been tuned over a 687- to 821-nm wavelength range. Quasi-CW, room-temperature operation also has been observed.

Optical gain from room-temperature V:KMgF₃ has been measured by a pump-probe technique. The observed cross section indicates the possible existence of excited-state absorption.

Tunable CW mode-locked operation has been demonstrated from 1.65 to 2.01 μm for a Co:MgF₂ laser, and 1.61 to 1.73 μm for a Ni:MgF₂ laser. Variations in pulse width as a function of wavelength have been observed, and pulses as short as 36 ps for Co:MgF₂ and 23 ps for Ni:MgF₂ have been obtained.

The localized UV laser photopolymerization of surface-adsorbed methyl methacrylate has been used to deposit poly (methyl methacrylate) films for direct patterning of wet and dry chemical etching processes. With this negative resist process, submicrometer linewidths have been demonstrated both in polymer deposition and in pattern transfer into Si and SiO₂.

Nitrocellulose, which functions as a self-developing photoresist, has been patterned using pulsed excimer laser radiation. The resolution of the resist has been found to be less than 0.3 μm .

3. MATERIALS RESEARCH

Development of the graphite-strip-heater technique for zone-melting recrystallization of Si films on SiO₂-coated Si substrates has been continued. Wafer flatness has been improved to a level approaching that required for VLSI applications, the surface protrusion density and the sub-boundary spacing have been shown to decrease as the temperature gradient at the growth interface increases, and the effect of parameters such as SiO₂ coating thickness and heater-sample spacing on the temperature gradient has been demonstrated.

With the objective of fabricating stable, low-resistance ohmic contacts to shallow p-n junctions (an important requirement for small-dimension Si transistors), an Al/W/Pd₂Si/poly-Si metallization scheme is being investigated. Initial annealing experiments indicate that at 450°C, Pd₂Si/poly-Si contacts are stable and W forms an effective diffusion barrier between Pd₂Si and Al.

A film of plasma-deposited Si₃N₄ has been employed to protect the gold front contact grid during the anodic oxidation steps in the fabrication of GaAs shallow-homojunction solar cells. The plasma deposition process can be performed on shallow (~500 Å) GaAs n⁺/p junctions with no degradation of junction properties, permitting cells with conversion efficiencies exceeding 20 percent (AM1) to be fabricated by this process.

Deep-level transient spectroscopy (DLTS) has been used to investigate the depth profile of electron traps in a GaAs sample prepared by vapor-phase growth of an epitaxial layer on a substrate that had been dry etched by reactive ion etching in CF₄ followed by Ar ion-beam etching. The epitaxial layer contains a significant concentration of electron traps that peak at a level somewhat above the layer-substrate interface. These traps can be attributed to the effect on the epitaxial growth process of damage to the substrate surface produced by dry etching.

4. MICROELECTRONICS

A technique has been developed for determining intrinsic stress, elastic bulk modulus, and yield strength of thin films by measuring the deformation vs pressure of circular membranes of the materials. Data for silicon-rich silicon nitride (SiN_x) membranes have been obtained, and it has been shown that the stress measurement technique can be extended to determine intrinsic stress in thin films deposited onto SiN_x membranes.

A 32-stage CCD binary-analog time-integrating correlator has been operated at a 20-MHz clock rate with an integration time of 25 μs. A simple post-processing technique has been demonstrated which removes the fixed-pattern noise from the CCD output.

A simple technique has been developed to ruggedize the bond of a corner-cube whisker contact to the underlying Schottky diode using a small (approximately 10-nl) drop of silica-loaded epoxy at the whisker/chip interface. The technique does not affect mixer performance, at least up to 2.5 THz, and allows the mixer assembly to survive a satellite-launch vibration qualification test.

A single-chip, CCD matrix-matrix product device has been fabricated and used with simulated radar video as a pulsed radar signal processor for 32 range bins, each with 32 Doppler resolution cells. False targets caused by fixed-pattern noise are found in the output of the device, but improved processing on subsequent runs of wafers is expected to reduce the magnitude of this problem.

5. ANALOG DEVICE TECHNOLOGY

Superconductor-insulator-superconductor tunnel junctions have been configured as a ring mixer in which a series array of four junctions is used in each of the four ring sections. This design provides higher output power, improved suppression of undesired mixing products, and increased RF impedance over those of the single-junction mixer. These mixer rings can therefore enhance the dynamic range of programmable analog-signal-processing devices, such as the superconductive convolver.

Pulse compression of a 200-MHz-bandwidth, 5- μ s-duration, pseudonoise-modulated radar waveform has been demonstrated with a programmable-matched-filter subsystem. This subsystem incorporates a previously reported air-gap acoustoelectric convolver with newly constructed digital-code generators and RF minimum-shift-keyed modulators; it provides twice the bandwidth of the best previous subsystem. The peak output of the compressed pulse is 35 dB above the rms level of the time sidelobes, and is only 2.5 dB less than the predicted ratio.

REPORTS ON SOLID STATE RESEARCH

15 June through 15 August 1983

PUBLISHED REPORTS

Journal Articles

JA No.

- | | | | |
|------|--|---|--|
| 5397 | Multigigahertz-Bandwidth Linear-Frequency-Modulated Filters Using a Superconductive Stripline | J.T. Lynch
R.S. Withers
A.C. Anderson
P.V. Wright
S.A. Reible | Appl. Phys. Lett. 43, 319
(1983) |
| 5402 | Solidification-Front Modulation to Entrain Subboundaries in Zone-Melting Recrystallization of Si on SiO ₂ | M.W. Geis
H.I. Smith*
D.J. Silversmith
R.W. Mountain
C.V. Thompson* | J. Electrochem. Soc. 130,
1178 (1983) |
| 5405 | Transmission Electron Microscopy of GaAs Permeable Base Transistor Structures Grown by Vapor Phase Epitaxy | B.A. Vojak
J.P. Salerno
D.C. Flanders
G.D. Alley
C.O. Bozler
K.B. Nichols
R.W. McClelland
N.P. Economou
G.A. Lincoln
R.A. Murphy
W.T. Lindley
G.D. Johnson | J. Appl. Phys. 54, 3554
(1983) |
| 5420 | Collisional Effects on the Rovibrational Transitions of the HD Fundamental Band | S. Nazemi*
A. Javan*
A.S. Pine | J. Chem. Phys. 78,
4797 (1983) |

* Author not at Lincoln Laboratory.

JA No.

- | | | | |
|------|--|--|--|
| 5423 | UV Laser Photopolymerization of Volatile Surface-Adsorbed Methyl Methacrylate | J.Y. Tsao
D.J. Ehrlich | Appl. Phys. Lett. 42 , 997 (1983) |
| 5430 | Low-Loss LiNbO ₃ Waveguide Bends with Coherent Coupling | L.M. Johnson
F.J. Leonberger | Opt. Lett. 8 , 111 (1983) |
| 5431 | Broadband Guided-Wave Optical Frequency Translator Using an Electro-Optical Bragg Array | R.H. Kingston
R.A. Becker
F.J. Leonberger | Appl. Phys. Lett. 42 , 759 (1983) |
| 5435 | Developing a Technology Base for Advanced Devices and Circuits | N.P. Economou | Proc. IEEE 71 , 601 (1983) |
| 5436 | Diffusion Length of Holes in <u>n</u> -InP | V. Diadiuk
S.H. Groves
C.A. Armiento
C.E. Hurwitz | Appl. Phys. Lett. 42 , 892 (1983) |
| 5437 | Three-Guide Optical Couplers in GaAs | J.P. Donnelly
N.L. DeMeo, Jr.
G.A. Ferrante | J. Lightwave Technol. LT-1 , 417 (1983) |
| 5438 | Electron-Beam Programmable 128K-Bit Wafer-Scale EPROM | D.C. Shaver
R.W. Mountain
D.J. Silversmith | IEEE Electron Device Lett. EDL-4 , 153 (1983) |
| 5444 | Damage Induced in Si by Ion Milling or Reactive Ion Etching | S.W. Pang
D.D. Rathman
D.J. Silversmith
R.W. Mountain
P.D. DeGraff | J. Appl. Phys. 54 , 3272 (1983) |
| 5447 | An Investigation of GaAs Films Grown by MBE at Low Substrate Temperatures and Growth Rates | G.M. Metz
A.R. Calawa
J.G. Mavroides | J. Vac. Sci. Technol. B 1 , 166 (1983) |
| 5469 | Comparison of Guided-Wave Interferometric Modulators Fabricated on LiNbO ₃ via Ti Indiffusion and Proton Exchange | R.A. Becker | Appl. Phys. Lett. 43 , 131 (1983) |
| 5473 | Impact Ionization in (100)-, (110)-, and (111)-Oriented InP Avalanche Photodiodes | C.A. Armiento
S.H. Groves | Appl. Phys. Lett. 43 , 198 (1983) |

JA No.

- | | | | |
|------|---|---|-------------------------------------|
| 5478 | Surface Photoacoustic Wave Spectroscopy of Thin Films | S.R.J. Brueck
T.F. Deutsch
D.E. Oates | Appl. Phys. Lett. 43, 157
(1983) |
| 5479 | Self-Developing Resist with Submicrometer Resolution and Processing Stability | M.W. Geis
J.N. Randall
T.F. Deutsch
P.D. DeGraff
K.E. Krohn
L.A. Stern | Appl. Phys. Lett. 43, 74
(1983) |
| 5483 | New Developments in Solid-State Lasers | P.F. Moulton | Laser Focus 19, 83 (1983) |
| 5484 | Laser-Controlled Chemical Etching of Aluminum | J.Y. Tsao
D.J. Ehrlich | Appl. Phys. Lett. 43, 146
(1983) |

Meeting Speeches**MS No.**

- | | | | |
|-------|---|---|--|
| 57071 | Laser Fabrication of Microstructures: Effect of Geometrical Scaling on Chemical Reaction Rates | D.J. Ehrlich
J.Y. Tsao | <i>In Laser Diagnostics and Photochemical Processing for Semiconductor Devices</i> , edited by R.M. Osgood, S.R.J. Brueck, and H.R. Schlossberg (North-Holland, New York, 1983), Vol. 17, p. 3 |
| 6076 | Electrical Characteristics of Zone-Melting-Recrystallized Si Films on Insulators | B-Y. Tsaur
J.C.C. Fan
M.W. Geis
R.L. Chapman
S.R.J. Brueck
D.J. Silversmith
R.W. Mountain | Proc. Materials Research Society Symp., Boston, 1-4 November 1982, Vol. 13, pp. 593-604 |
| 6077 | Ion Implantation Technique for Simultaneous Formation of Shallow Silicide/Silicon Ohmic Contact | B-Y. Tsaur
C.H. Anderson, Jr. | Thin Solid Films 104, 383
(1983) |

MS No.

- | | | | |
|------|---|---|--|
| 6081 | UV Laser-Initiated Formation of Si_3N_4 | T.F. Deutsch
D.J. Silversmith
R.W. Mountain | In <i>Laser Diagnostics and Photochemical Processing for Semiconductor Devices</i> , edited by R.M. Osgood, S.R.J. Brueck, and H.R. Schlossberg (North-Holland, New York, 1983), Vol. 17, p. 129 |
| 6084 | Submicrometer-Linewidth Laser Doping | J.Y. Tsao
D.J. Ehrlich | In <i>Laser Diagnostics and Photochemical Processing for Semiconductor Devices</i> , edited by R.M. Osgood, S.R.J. Brueck, and H.R. Schlossberg (North-Holland, New York, 1983), Vol. 17, p. 235 |
| 6091 | Summary Abstract: Zone-Melting Recrystallization of Si Films with a Movable Strip-Heater Oven | M.W. Geis | J. Vac. Sci. Technol. A 1, 716 (1983) |
| 6092 | Optical Microanalysis of Small Semiconductor Structures | D.V. Murphy
S.R.J. Brueck | In <i>Laser Diagnostics and Photochemical Processing for Semiconductor Devices</i> , edited by R.M. Osgood, S.R.J. Brueck, and H.R. Schlossberg (North-Holland, New York, 1983), Vol. 17, p. 81 |
| 6108 | Pulsed UV Excimer Laser Doping of Semiconductors | T.F. Deutsch | In <i>Laser Diagnostics and Photochemical Processing for Semiconductor Devices</i> , edited by R.M. Osgood, S.R.J. Brueck, and H.R. Schlossberg (North-Holland, New York, 1983), Vol. 17, p. 225 |
| 6204 | Fabrication of Submicrometer Structures in Si Using SiCl_4/O_2 Reactive Ion Etching | S.M. Cabral
D.D. Rathman
N.P. Economou | Electrochemical Society Extended Abstracts, Vol. 83-1, No. 153, p. 246 |

MS No.

- | | | | |
|------|--|--|---|
| 6205 | The Effect of Chamber Configuration and Bias Voltage on Damage Induced in Si by Reactive Ion Etching | S.W. Pang
C.M. Horwitz*
D.D. Rathman
S.M. Cabral
D.J. Silversmith
R.W. Mountain | Electrochemical Society
Extended Abstracts,
Vol. 83-1, No. 172, p. 278 |
| 6207 | Limitations of Laser Transmission Measurements Due to Correlated Atmospheric Effects | N. Menyuk
D.K. Killinger | <i>Laser Beam Propagation in the Atmosphere</i> ,
J.C. Leader, Ed., Proc.
SPIE 410, 32-36 (1983) |
| 6259 | Zone-Melting Recrystallization of InSb on Oxidized Si Wafers | C.J. Keavney*
H.A. Atwater*
H.I. Smith*
M.W. Geis | Electrochemical Society
Extended Abstracts,
Vol. 83-1, No. 331, p. 520 |
| 6271 | Monolithic Frequency Doublers | A. Chu
W.E. Courtney
L.J. Mahoney
R.A. Murphy
R.W. McClelland | <i>IEEE 1983 Microwave and Millimeter-Wave Monolithic Circuits Symposium</i> , Digest of Papers, B.E. Spielman, Ed. (IEEE, New York, 1983), pp. 45-49 |

* * * * *

UNPUBLISHED REPORTS**Journal Articles****JA No.**

- | | | | |
|------|--|--|---------------------------------------|
| 5429 | 20 GHz Optical Waveguide Sampler | L.A. Molter-Orr
H.A. Haus*
F.J. Leonberger | Accepted by IEEE J. Quantum Electron. |
| 5449 | Broadly Tunable Modelocked HgCdTe Lasers | R.S. Putnam*
M.M. Salour*
T.C. Harman | Accepted by Appl. Phys. Lett. |

* Author not at Lincoln Laboratory.

JA No.

5466	Enhanced Raman Scattering from Si Microstructures	S.R.J. Brueck D.V. Murphy	Accepted by Opt. Lett.
5472	An Ultrafast All-Optical Gate	A. Lattes* H.A. Haus* F.J. Leonberger E.P. Ippen*	Accepted by IEEE J. Quantum Electron.
5481	An Assessment of Relative Error Sources on Infrared DIAL Measurement Accuracy	N. Menyuk D.K. Killinger	Accepted by Appl. Opt.
5486	InP Optoelectronic Switches	A.G. Foyt F.J. Leonberger	Accepted as Chapter in <i>Picosecond Optoelectronic Devices</i> , C.H. Lee, Ed. (Academic Press, New York)
5489	Laser Direct Writing for VLSI	D.J. Ehrlich J.Y. Tsao	Accepted as Chapter in <i>VLSI Electronics</i> (Academic Press, New York)
5490	Fully Isolated Lateral Bipolar/MOS Transistors Fabricated in Zone-Melting-Recrystallized Si Films on SiO ₂	B-Y. Tsaur D.J. Silversmith J.C.C. Fan R.W. Mountain	Accepted by IEEE Electron Device Lett.
5494	Resonant Tunneling Through Quantum Wells at Frequencies Up to 2.5 THz	T.C. Sollner W.D. Goodhue P.E. Tannenwald C.D. Parker D.D. Peck	Accepted by Appl. Phys. Lett.
5509	Optimal Design of Amorphous Single-Junction and Tandem Solar Cells	J.C.C. Fan B.J. Palm	Accepted by Solar Cells
5524	Effect of Substrate Annealing and V-III Flux on the Molecular Beam Epitaxial Growth of AlGaAs-GaAs Single Quantum Wells	P.A. Maki* S.C. Palmateer* G.W. Wicks* A.R. Calawa L.F. Eastman*	Accepted by J. Electron. Mater.

* Author not at Lincoln Laboratory.

Meeting Speeches*

MS No.

5264E	Recent Advances in Tunable Lasers and Applications	A. Mooradian	Seminar, General Motors Company, Dearborn, Michigan, 23 May 1983
5707J	Laser Direct-Write Processing	J.Y. Tsao D.J. Ehrlich D.J. Silversmith	Custom Integrated Circuits Conf., Rochester, New York, 23-25 May 1983
5934A	Thin Films of III-V Compounds and Their Applications	J.C.C. Fan	} The 2nd Republic of China Solar Cell Workshop, Hinschu, Taiwan, 7-8 June 1983
6094A	High-Efficiency Cells	J.C.C. Fan	
6008A	High-Efficiency, Low-Cost Crystalline Tandem Cells	J.C.C. Fan	The Electrochemical Society, San Francisco, 8-13 May 1983
6008C	High-Efficiency Tandem Cells	J.C.C. Fan	Seminar, Polaroid Corporation, Cambridge, Massachusetts, 14 July 1983
6078A	Excitation of Surface Optical Waves and Material Ripples by Stimulated Scattering	S.R.J. Brueck D.J. Ehrlich J.Y. Tsao	Seminar, Technical University of Vienna, Austria, 4 July 1983
6079B	Wideband Analog Signal Processing with Superconductive Circuits	R.W. Ralston	Seminar, IBM Zurich Research Laboratory, Ruschlikon, Switzerland, 27 July 1983
6106A; B	Preparation of High-Quality Silicon Films on Insulators by Zone-Melting Recrystallization	B-Y. Tsaur	Joint U.S.-Japan Seminar on Epitaxy and Interface Kinetics, Oiso, Japan, 20-24 June 1983; Seminar, National Taiwan University, 30 June 1983
6184A	Optically Pumped Mode-Locked LPE-Grown HgCdTe Lasers	R.S. Putnam† M.M. Salour† T.C. Harman	CLEO '83, Baltimore, Maryland, 17-20 May 1983

* Titles of Meeting Speeches are listed for information only. No copies are available for distribution.

† Author not at Lincoln Laboratory.

MS No.

6216	2-Bit 1-GSample/s Electrooptic Guided-Wave Analog-to-Digital Converter System	R.A. Becker C.E. Woodward F.J. Leonberger	CLEO '83, Baltimore, Maryland, 17-20 May 1983
6217	Fourier Transformation Using an Electroabsorption CCD Spatial Light Modulator	R.H. Kingston F.J. Leonberger	
6223	Linearity Measurements of High-Speed InP Optoelectronic Switches	C.H. Cox A.G. Foyt V. Diadiuk R.C. Williamson	
6226	Laser Remote Sensing Using Heterodyne and Direct Detection IR LIDAR	D.K. Killinger N. Menyuk	
6255	Applications of Excimer Lasers to Semiconductor Processing	T.F. Deutsch	
6283	New Solid State Tunable Lasers	P.F. Moulton	1983 Electronic Materials Conference, Burlington, Vermont, 22-24 June 1983
6192A	Advances in LEC Growth of InP Crystals	G.W. Iseler	
6295	Growth of GaAs at 550°C Using Chloride Transport Vapor Phase Epitaxy	K.B. Nichols C.O. Bozler	
6300	Orientation Filtering by Growth-Velocity Competition in Zone Melting Recrystallization of Silicon on SiO ₂	H.A. Atwater* H.I. Smith* C.V. Thompson* M.W. Geis	
6301	Laser-Controlled Chemical Etching of Aluminum	J.Y. Tsao D.J. Ehrlich D.J. Silversmith R.W. Mountain	
6304	Surface Defects in GaAs MBE Growth	A.R. Calawa G.M. Metze M.J. Manfra	

* Author not at Lincoln Laboratory.

MS No.

6305	Zone-Melting Recrystallization of Silicon-on-Insulator Films by the Graphite Strip-Heater Technique: Recent Advances	C.K. Chen M.W. Geis B-Y. Tsaur R.L. Chapman J.C.C. Fan	1983 Electronic Materials Conference, Burlington, Vermont, 22-24 June 1983
6218	Integrated Optics Wavefront Measurement Sensor	R.H. Rediker T.A. Lind F.J. Leonberger	4th International Conference on Integrated Optics and Optical Fiber Communication (IOOC '83), Tokyo, Japan, 27-30 June 1983
6227	New Developments in Mass-Transported GaInAsP/InP Buried-Heterostructure Lasers	Z.L. Liao J.N. Walpole D.Z. Tsang	
6228	GaInAsP Buried-Heterostructure Optical Waveguide Devices	L.M. Johnson Z.L. Liao S.H. Groves J.P. Donnelly	
6279	Progress in Ti:LiNbO ₃ and InP Waveguide Devices for Signal Processing Applications	F.J. Leonberger	
6336	Active Q-Switching of a Low Threshold Buried-Heterostructure Diode Laser	D.Z. Tsang J.N. Walpole Z.L. Liao S.H. Groves	
6233A	Superconductive Tapped Delay Lines for Low-Insertion-Loss Wideband Analog Signal-Processing Filters	R.S. Withers P.V. Wright	Frequency Control Symp., Philadelphia, 1 June 1983
6234	Diagnostics and Processing of Semiconductors with Lasers	P.L. Kelley	Los Alamos Conference on Optics '83, Santa Fe, New Mexico, 11-15 April 1983
6240	LiNbO ₃ Guided-Wave Interferometric Modulators	F.J. Leonberger	1983 IEEE International Symposium on Applications of Ferroelectrics (ISAF), Gaithersburg, Maryland, 1-3 June 1983

MS No.

6241	Monolithic Integrated Circuit Mixers for the Millimeter and Sub-millimeter Wave Regions	B.J. Clifton	8th European Specialists Workshop on Microwave Devices, Maidenhead, Berks, UK, 4-6 May 1983
6277	Surface Photoacoustic Wave Spectroscopy of Adsorbed Molecules	S.R.J. Brueck T.F. Deutsch D.E. Oates	SICOLS '83, Interlaken, Switzerland, 27 June - 1 July 1983
6281	Laser Direct-Write Processing	D.J. Ehrlich J.Y. Tsao	
6291	A Technique for the Determination of Stress in Thin Films	E.I. Bromley J.N. Randall D.C. Flanders R.W. Mountain	
6292	A Precision Wide-Range Optical Gap Measurement Technique	D.C. Flanders T.M. Lyszczarz	
6299	Nitrocellulose as a Self-Developing Resist with Submicrometer Resolution and Processing Stability	M.W. Geis J.N. Randall T.F. Deutsch N.N. Efremow J.P. Donnelly J.D. Woodhouse	1983 International Symposium on Electron, Ion, and Photon Beams, Los Angeles, 30 May - 3 June 1983
6307	Effects of Dry Etching on GaAs	S.W. Pang G.A. Lincoln R.W. McClelland P.D. DeGraff M.W. Geis W.J. Piacentini	
6308	Silicon Nitride Stencil Masks for High Resolution Ion Lithography Proximity Printing	J.N. Randall D.C. Flanders N.P. Economou J.P. Donnelly E.I. Bromley	
6309	Read-Only Memory with Electron-Beam Programmable Floating-Gate Transistors	D.C. Shaver	

MS No.

6318	Deep UV Spatial-Period-Division by Combining Multilayer Mirrors with Diffraction Gratings	A.M. Hawryluk* H.I. Smith* D.J. Ehrlich	1983 International Symposium on Electron, Ion, and Photon Beams, Los Angeles, 30 May - 3 June 1983
6319	Ion Beam Assisted Etching of GaAs Over Large Areas at High Etch Rates and Controlled Anisotropy	G.A. Lincoln M.W. Geis S. Pang N.N. Efremow	
6287	Laser Excitation Fluorescence Measurements of CF ₂ Concentra- tions and Vibrational and Rota- tional Temperatures in a CF ₄ Plasma Reactor	S.R.J. Brueck S. Pang	6th International Confer- ence on Plasma Chemistry, Montreal, Quebec, 24-28 June 1983
6289	Applications of LiNbO ₃ Guided- Wave Interferometric Modulators	F.J. Leonberger	29th International Instru- mentation Symposium, Albuquerque, New Mexico, 2-5 May 1983
6294	Impact Ionization in (100)-, (110)-, and (111)-Oriented InP Avalanche Photodiodes	C.A. Armiento S.H. Groves	41st Annual Device Research Conference, Burlington, Vermont, 20-22 June 1983
6302	Recent Experimental Results of Si Permeable Base Transistors	D.D. Rathman N.P. Economou D.J. Silversmith R.W. Mountain S.M. Cabral	
6312	High-Speed Performance of InGaAs Photodiodes	V. Diadiuk S.H. Groves D.Z. Tsang J.N. Walpole	
6313	Submicrometer Laser-Direct-Write Processing	D.J. Ehrlich J.Y. Tsao	
6314	Fully Isolated Lateral Bipolar/ MOS Transistors Fabricated in Zone-Melting-Recrystallized Si Films on SiO ₂	B-Y. Tsaur D.J. Silversmith J.C.C. Fan R.W. Mountain	

* Author not at Lincoln Laboratory.

MS No.

6325	Single-Mode GaInAsP Buried-Heterostructure Optical Waveguide Devices	L.M. Johnson Z.L. Liao S.H. Groves J.P. Donnelly	41st Annual Device Research Conference, Burlington, Vermont, 20-22 June 1983
6329	Resonant Tunneling Through Quantum Wells at 2.5 THz	T.C. Sollner W.D. Goodhue P.E. Tannenwald C.D. Parker D.D. Peck	
6331	Continuous Multi-Gigahertz Modulation of Q-Switched GaInAsP Diode Lasers at High Modulation Rates	D.Z. Tsang J.N. Walpole Z.L. Liao S.H. Groves	
6299A	Nitrocellulose as a Self-Developing Resist with Submicrometer Resolution and Processing Stability	M.W. Geis J.N. Randall T.F. Deutsch N.N. Efremow J.P. Donnelly J.D. Woodhouse	New England Annual AVS Symposium, Danvers, Massachusetts, 20-21 June 1983
6340	Laser Photodeposition	D.J. Ehrlich J.Y. Tsao	
6334	Quartz Rotary-Table Substrate Holder for Epitaxial Growth Reactor	D.L. Hovey	28th Annual ASGS Symposium '83, Philadelphia, 13-17 June 1983
6343	High-Quality Silicon Films Prepared by Zone-Melting Recrystallization	C.K. Chen M.W. Geis B-Y. Tsaur J.C.C. Fan	High Speed Growth and Characterization of Crystals for Solar Cells - Research Forum, Port St. Lucie, Florida, 25-27 July 1983
6344	Analog Signal Processing	E. Stern	Seminar, Columbia University, New York City, 13 May 1983
6353	Analytical Comparison of Optimized Heterodyne and Direct-Detection CO ₂ LIDAR for Atmospheric Remote Sensing	D.K. Killinger N. Menyuk	Optical Society of America Topical Mtg., Aspen, Colorado, 1-4 August 1983

MS No.

6357	X-Ray Lithography	D.C. Flanders	Lithography and Dry Etch Short Course, Cornell Uni- versity, 15 June 1983
6361	Damage in Si and GaAs Induced by Reactive Ion Etching	S.W. Pang	Seminar, Materials Research Corporation, Orangeburg, New York, 9 June 1983
6387	Physics and Device Implications of Silicon-on-Insulator Substrates	D.J. Silversmith	Seminar, GTE Laboratories, Waltham, Massachusetts, 21 July 1983

ORGANIZATION

SOLID STATE DIVISION

A.L. McWhorter, *Head*
I. Melngailis, *Associate Head*
J.F. Goodwin, *Assistant*

P.E. Tannenwald, *Senior Staff*

QUANTUM ELECTRONICS

A. Mooradian, *Leader*
P.L. Kelley, *Associate Leader*

Barch, W.E.	Johnson, B.C.*
Belanger, L.J.	Killinger, D.K.
Brueck, S.R.J.	Lenth, W.
Burke, J.W.	Lovold, S.H.G.
Bushee, J.F., Jr.	Menyuk, N.
DeFeo, W.E.	Moulton, P.F.
Deutsch, T.F.	Murphy, D.V.
Ehrlich, D.J.	Rosenbluh, M.†
Feldman, B.	Sedlacek, J.H.C.
Force, A.	Sharpe, K.A.
Hancock, R.C.	Sullivan, D.J.
Harrison, J.*	Tsao, J.Y.

ELECTRONIC MATERIALS

A.J. Strauss, *Leader*
J.C.C. Fan, *Assistant Leader*
J.G. Mavroides, *Senior Staff*
H.J. Zeiger, *Senior Staff*

Anderson, C.H., Jr.	Kolesar, D.F.
Branz, H.M.*	Krohn, L., Jr.
Button, M.J.	Mastromattei, E.L.
Chapman, R.L.	McClelland, R.W.
Chen, C.K.	Metze, G.M.
Connors, M.K.	Nitishin, P.M.
Davis, F.M.	Palm, B.J.
Delaney, E.J.	Pantano, J.V.
Fahey, R.E.	Taylor, M.S.†
Finn, M.C.	Tracy, D.M.
Gale, R.P.	Tsaur, B-Y.
Iseler, G.W.	Turner, G.W.
King, B.D.	Windhorn, T.H.

APPLIED PHYSICS

R.C. Williamson, *Leader*
F.J. Leonberger, *Assistant Leader*
T.C. Harman, *Senior Staff*
R.H. Kingston, *Senior Staff*
R.H. Rediker, *Senior Staff*

Becker, R.A.
Carter, F.B.
Chinnock, C.B.
Cox, C.H., III
DeMeo, N.L., Jr.
Diadiuk, V.
Donnelly, J.P.
Ferrante, G.A.
Groves, S.H.

Hakimi, F.*
Hovey, D.L.
Johnson, L.M.
Liau, Z.L.
Lind, T.A.
McBride, W.F.
Molter-Orr, L.*
O'Donnell, F.J.
Paladino, A.E.

Plonko, M.C.
Schloss, R.P.*
Spears, D.L.
Tsang, D.Z.
Walpole, J.N.
Whitaker, N.*
Woodhouse, J.D.
Yap, D.*

* Research Assistant

† Summer Staff

ANALOG DEVICE TECHNOLOGY

E. Stern, *Leader*
J.H. Cafarella, *Assistant Leader*
R.W. Ralston, *Assistant Leader*

Anderson, A.C.
Arsenault, D.R.
Boisvert, R.R.
Bouman, C.A.
Brogan, W.T.
Dolat, V.S.
Fischer, J.H.
Flynn, G.T.

Gottschalk, P.G.*
Green, J.B.
Hauser, E.M.
Holtham, J.H.
Kernan, W.C.
Lattes, A.L.
Leung, I.
Macedo, E.M., Jr.

Macropoulos, W.
Melngailis, J.†
Oates, D.E.
Reible, S.A.
Sage, J.P.
Slattery, R.L.
Withers, R.S.
Yao, I.

MICROELECTRONICS

W.T. Lindley, *Leader*
F.J. Bachner, *Associate Leader*
N.P. Economou, *Assistant Leader*
R.A. Murphy, *Assistant Leader*

Bozler, C.O.
Bromley, E.I.
Burke, B.E.
Cabral, S.M.
Calawa, A.R.
Chen, C.L.
Chiang, A.M.
Chu, A.
Clifton, B.J.
Daniels, P.J.
Durant, G.L.
Efremow, N.N., Jr.
Felton, B.J.
Flanders, D.C.

Geis, M.W.
Gray, R.V.
Hollis, M.A.
Lax, B.†
Lincoln, G.A., Jr.
Lyszczarz, T.M.
Mahoney, L.J.
Manfra, M.J.
McGonagle, W.H.
Mountain, R.W.
Mroczkowski, I.H.
Nichols, K.B.
Pang, S.W.
Parker, C.D.

Peck, D.D.
Piacentini, W.J.
Pichler, H.H.
Rabe, S.
Randall, J.N.
Rathman, D.D.
Shaver, D.C.
Silversmith, D.J.
Smythe, D.L., Jr.
Sollner, T.C.L.G.
Taylor, J.A.*
Vera, A.
Vojak, B.A.
Wilde, R.E.

* Research Assistant

† Part Time

1. SOLID STATE DEVICE RESEARCH

1.1 GaInAsP BURIED-HETEROSTRUCTURE WAVEGUIDE DEVICES

Low-loss single-mode GaInAsP optical waveguide branches and bends have been demonstrated. These devices utilize a buried-heterostructure geometry to obtain tight optical confinement and low scattering loss and are fabricated using a novel etch and LPE regrowth technique. Such structures are required for a wide variety of integrated optical components, including multiple-branching circuits and interferometric modulators. Branching losses as low as 0.4 dB have been obtained at 1.3 μm for branch angles of 1° .

The waveguide fabrication procedure is illustrated in Figure 1-1. A double-heterostructure wafer was first prepared using conventional LPE techniques on a (100) n-InP substrate. The grown layers were n-type with low 10^{17} cm^{-3} carrier concentration. The GaInAsP layer and InP cap layer were $\approx 2000 \text{ \AA}$ and $\approx 5000 \text{ \AA}$ thick, respectively. The InP buffer layer was $\approx 4 \text{ }\mu\text{m}$ thick. An etch mask, as shown in Figure 1-1(a), was formed by patterning e-beam-evaporated 3.5- μm -wide, 500- \AA -thick Ti strips. Selective chemical etching¹ as illustrated in Figure 1-1(b) was then used to form the waveguide pattern in the quaternary. By starting with the thin InP cap layer and carefully prepared Ti etch mask, precise dimensional control of the quaternary region can be obtained along with very smooth sidewalls. Additional dimensional control can be achieved by undercutting the quaternary layer. After completion of the etching steps, a $\approx 3\text{-}\mu\text{m}$ -thick LPE InP layer was grown over the entire wafer yielding buried-heterostructure waveguides as shown in Figure 1-1(c). Good surface morphology was obtained over the entire wafer of $\approx 1 \times 1 \text{ cm}$. Prior to testing, the devices were cleaved to a length of $\approx 8 \text{ mm}$.

Waveguide branches and bends were formed using this fabrication technique. Branching structures were formed using the quaternary, $\text{Ga}_{0.17}\text{In}_{0.83}\text{As}_{0.4}\text{P}_{0.6}$, with $\lambda_g = 1.15 \text{ }\mu\text{m}$ and a refractive index difference with respect to InP of $\Delta n = 0.22$. The bend structures were fabricated from $\text{Ga}_{0.21}\text{In}_{0.79}\text{As}_{0.49}\text{P}_{0.51}$ ($\lambda_g = 1.21 \text{ }\mu\text{m}$) with $\Delta n = 0.26$. The quaternary channels were etched to widths of 1.5 and 2.0 μm for the bending and branching structures, respectively, to assure single-mode operation at 1.3 μm . The devices were tested by endfire coupling TE polarized 1.3- μm input light from a diode laser. Single-mode operation was confirmed by viewing the output on an infrared vidicon.

The branch-structure geometry is shown in Figure 1-2(a). The branch angle θ ranged from 0.6° to 3.0° . The waveguide branch transmission is plotted in Figure 1-2(b) as a function of θ by taking the ratio of the sum of the output powers of the two arms relative to straight guides fabricated on the same substrate. There was less than 10-percent variation between the output powers of the two arms of each branch. The branch loss varies from 0.2 dB at $\theta = 0.6^\circ$ to 3.3 dB at $\theta = 3.0^\circ$. A sample consisting of straight waveguides, which were otherwise identical to the branch structures, was also fabricated. By successively measuring the waveguide optical output for three different sample lengths, it was determined that the straight-waveguide propagation loss is not higher than 1.5 cm^{-1} .

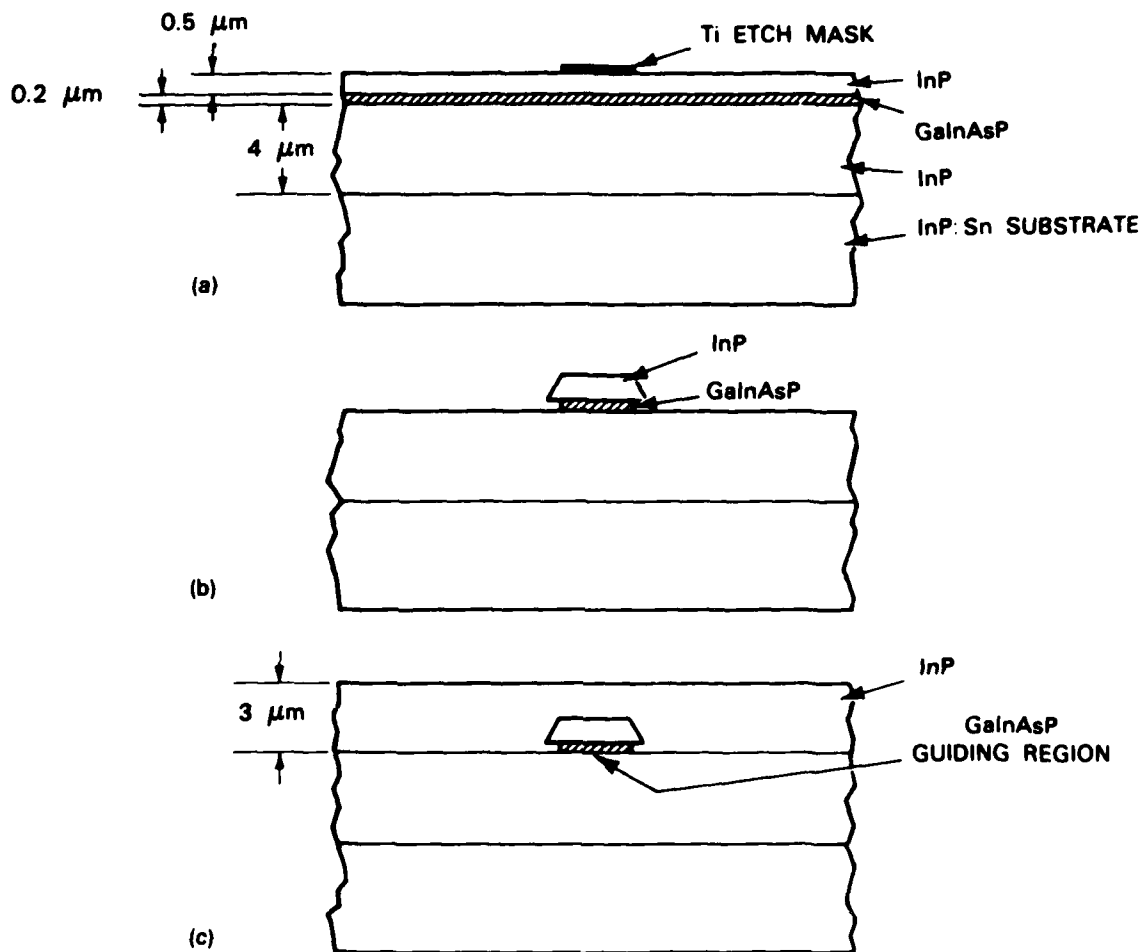


Figure 1-1. Schematic illustration of waveguide fabrication showing (a) double-heterostructure wafer with Ti etch mask, (b) wafer following selective chemical etching, and (c) waveguide sample following LPE regrowth.

128049-N-02

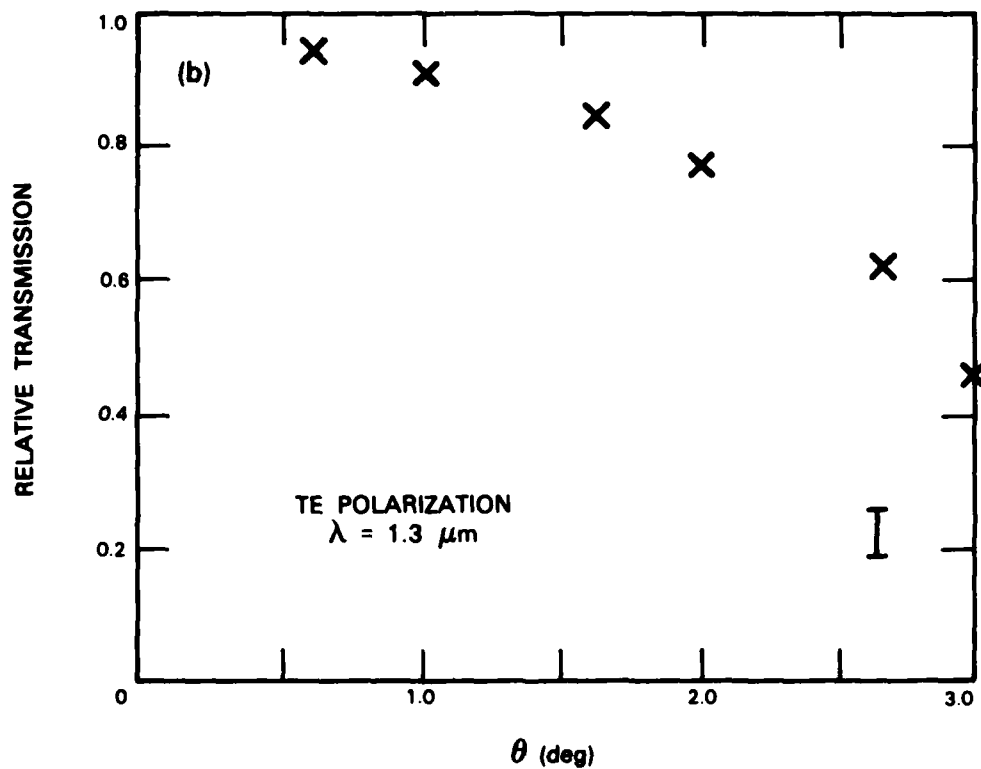
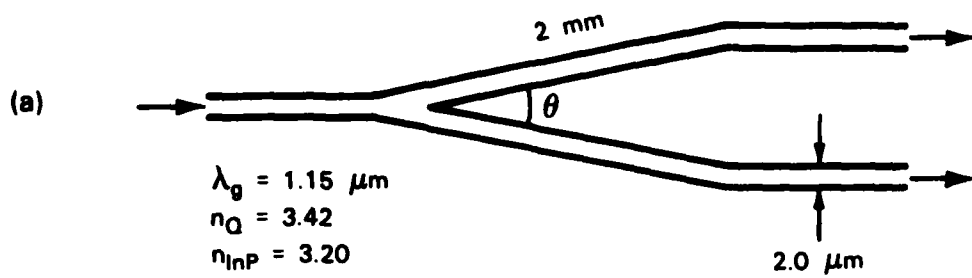


Figure 1-2. (a) Schematic illustration of waveguide branch and (b) measured branch transmission as a function of branch angle θ .

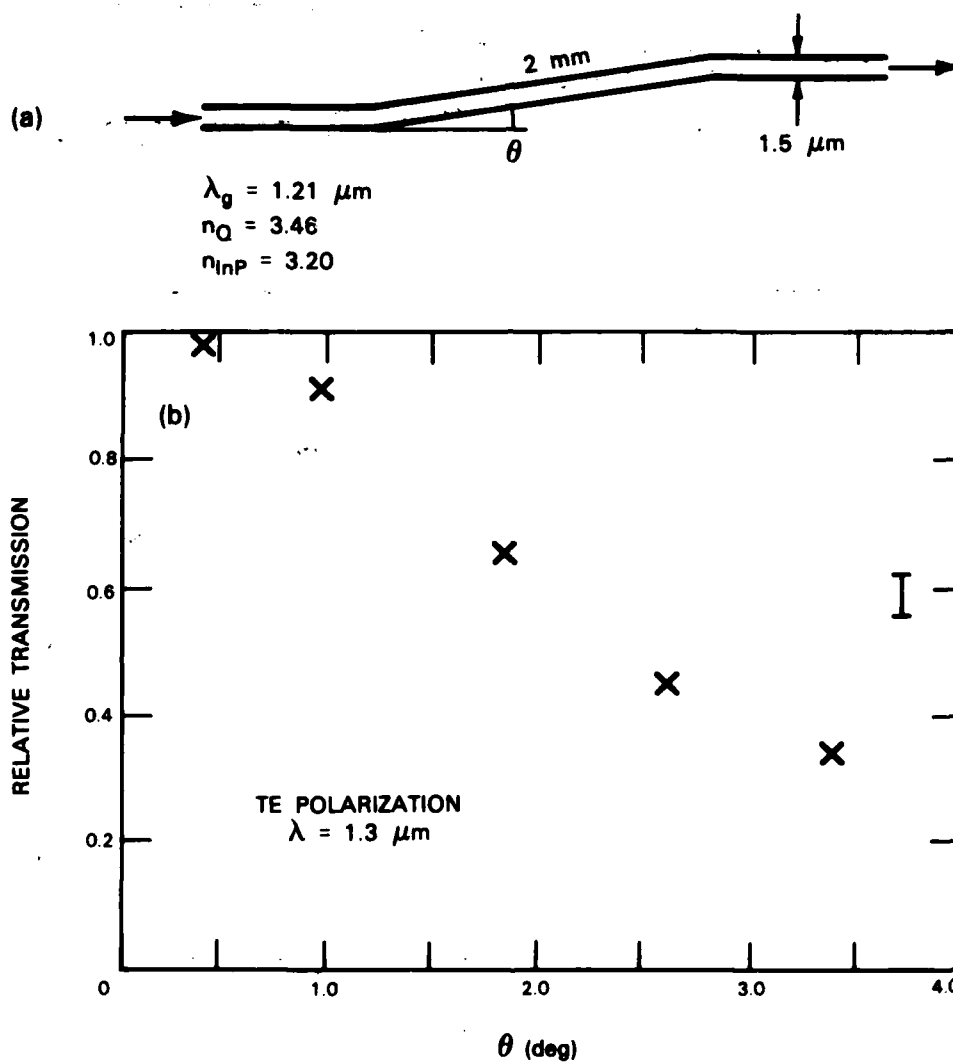


Figure 1-3. (a) Schematic illustration of waveguide bend structure and (b) measured transmission per single bend as a function of bend angle ϕ .

128054-N-03

The bend-structure geometry is shown in Figure 1-3(a). The bend angle ϕ ranged from 0.5° to 3.4° . The measured transmission through a single bend as a function of ϕ is plotted in Figure 1-3(b) by taking the square root of the ratio of the output power of the bend structure relative to straight guides on the same substrate. The bend loss ranged from 0.1 dB at $\phi = 0.5^\circ$ to 4.2 dB at $\phi = 3.4^\circ$.

In summary, low-loss single-mode GaInAsP waveguide branches and bends have been demonstrated. Work is in progress to further improve device performance.

L.M. Johnson
Z.L. Liao

S.H. Groves
J.P. Donnelly

1.2 LINEARITY MEASUREMENTS OF HIGH-SPEED InP OPTOELECTRONIC SWITCHES

The development of high-speed optoelectronic switches has progressed to the point where it is now appropriate to conduct some detailed investigations of the various switch parameters. One important parameter is linearity, as this will play a central role in various RF applications of the switch, such as mixers.

Ideally there should be a linear relationship between the laser power incident on the switch and the switch conductance. Experimentally the degree of nonlinearity is expected to be small. Thus, it is not feasible to make direct measurements of the degree of nonlinearity. A standard technique for measuring small nonlinearities in RF devices, such as amplifiers and mixers, is to measure the level of the intermodulation outputs produced by two equal-amplitude sinusoidal inputs closely spaced in frequency. Although intermodulation products of all orders are present at the output, attention is usually focused on only the second and third orders, i.e., those outputs that result from the quadratic and cubic terms in a power series expansion of the device's transfer function. If f_1 and f_2 are the input frequencies, then the quadratic term generates outputs at frequencies $2f_1$, $2f_2$ and $f_1 \pm f_2$. The cubic term generates outputs at $3f_1$, $3f_2$, $2f_1 \pm f_2$ and $2f_2 \pm f_1$. As is customary, only the $f_1 \pm f_2$ terms are measured for the second order and only the $2f_1 - f_2$ and $2f_2 - f_1$ terms are used for the third-order measurements.

The basis for the intermodulation terms lies in the eventual saturation of the switch's I-V curve at high RF amplitudes. Figure 1-4 shows a typical I-V curve. The level of illumination is seen to affect the I-V curve in two ways: the slope around the origin and the saturation level. Further, if the illumination of the switch is highly asymmetric with respect to the switch gap, the saturation levels become highly asymmetric as well. Since it is unlikely that the switch would be used in this mode, investigation of the effects of asymmetric illumination on intermodulation levels has been deferred. The effects of the symmetric illumination are described below.

A block diagram of the test setup used to make the intermodulation measurements is shown in Figure 1-5. Following the RF combining and attenuating networks, two bias tees are included, one on each side of the switch. This arrangement permits measurements to be

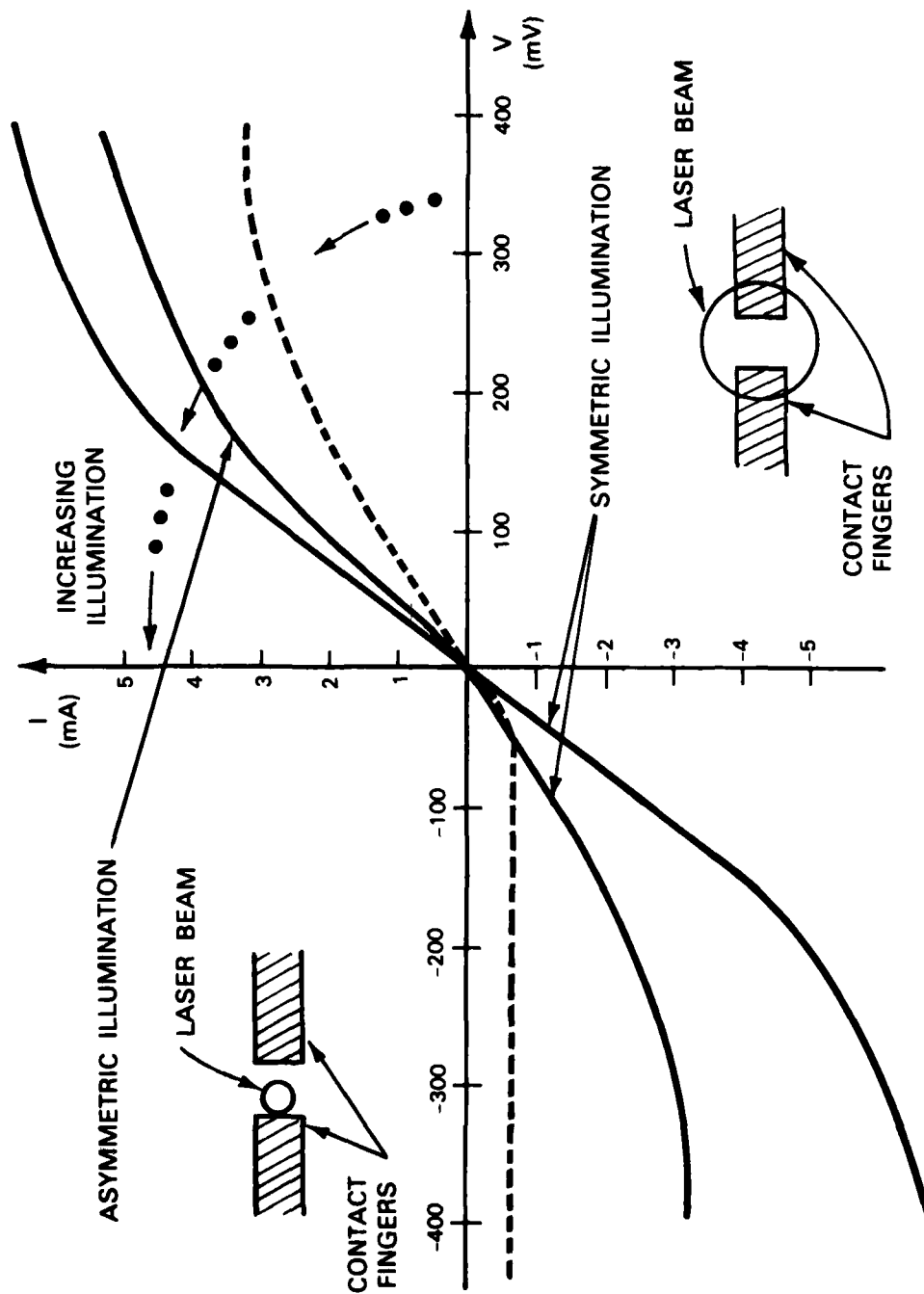


Figure 1-4. I-V curves of InP switch for both symmetric illumination (solid curves) and highly asymmetric illumination (dashed curve).

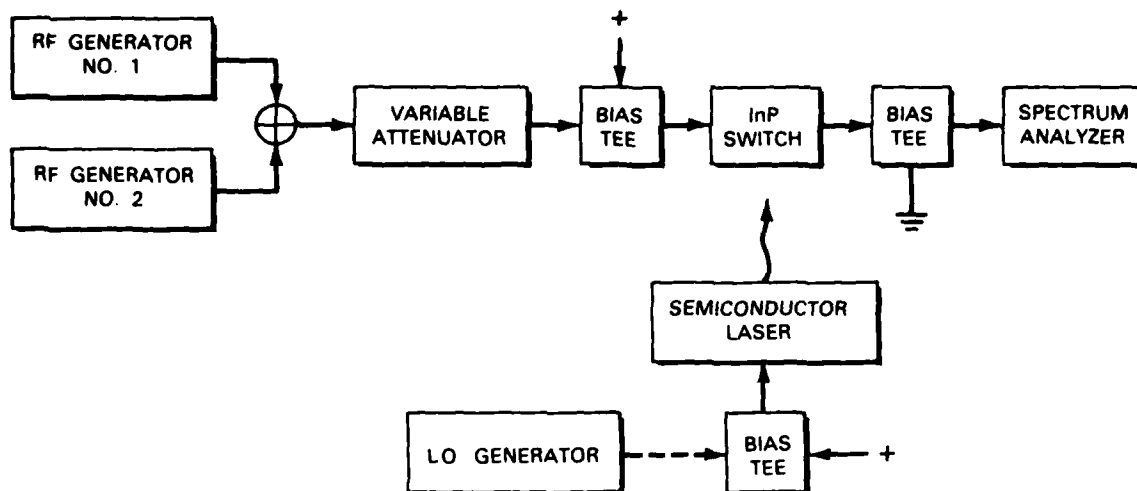


Figure 1-5. Block diagram of test setup for measuring intermodulation outputs produced by InP switch.

made as a function of location along the device's I-V curve, while isolating the DC bias from both the RF generators and the spectrum analyzer. The switch is activated via a semiconductor laser, whose bias is adjusted so as to produce the desired switch I-V curve. The laser also can be modulated, if desired, but this feature was not used in the present experiments.

A typical set of data is shown in Figure 1-6. The amplitudes of three RF outputs, i.e., the averages of the fundamental, the second- and the third-order pairs, are all plotted vs RF input power with zero DC bias on the switch. From the fundamental curve, the insertion loss of the switch can be determined; for this device it is ≈ 4 dB. This value is consistent with the insertion loss predicted from measurement of the switch's "on" resistance.

The second- and third-order amplitudes have a slope of 2 and 3, respectively, as expected. Note that the amplitude of the second-order term is lower than the third-order term. This is consistent with the odd symmetry [$f(-x) = -f(x)$] of the switch's I-V curve when operating at zero bias and under symmetric illumination. In the power series expansion for this I-V curve, the coefficients of the odd powers will dominate over the even power coefficients.

In order to examine the effects of other variables, e.g., input frequency or switch illumination, it is convenient to have a single number that characterizes the data. Such a number is usually obtained by extending all three curves and recording the output amplitude of the fundamental-second-order and fundamental-third-order intersection points, which are commonly referred to as intercepts. The intercept points from Figure 1-6 have been replotted as the left-most points in Figure 1-7. Also plotted in Figure 1-7 are the second- and

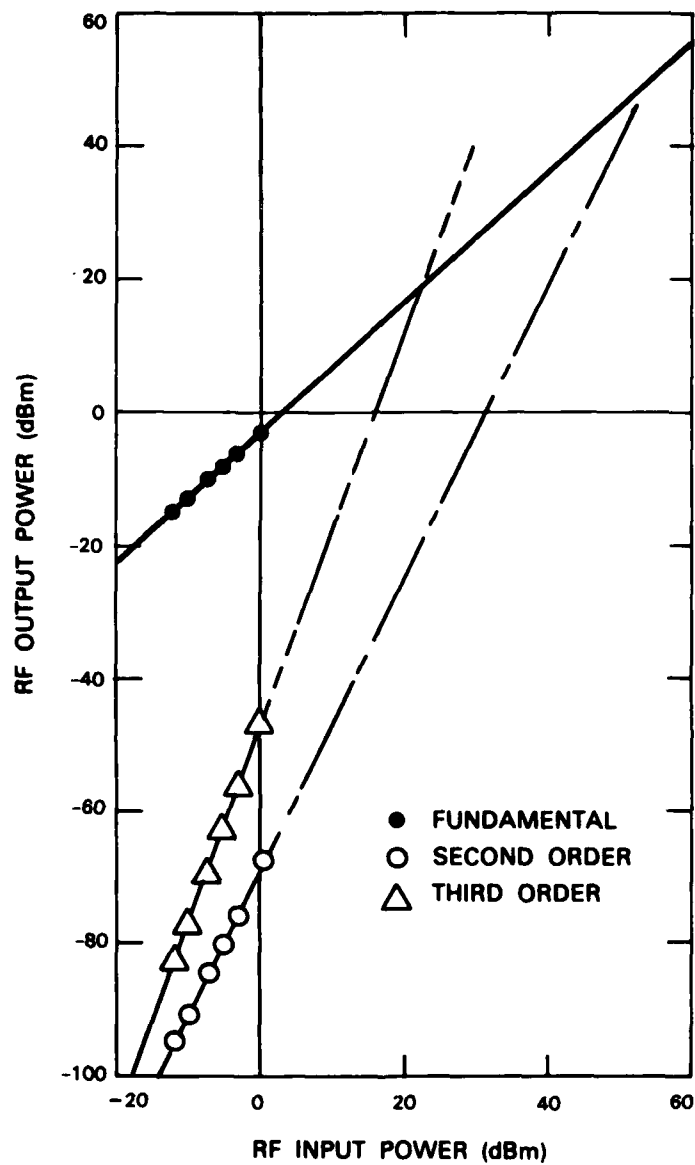


Figure 1-6. Plot of three RF outputs: the fundamental, second, and third order vs RF inputs at 97 and 103 MHz. Laser power constant at 4.5 mW.

131049-R

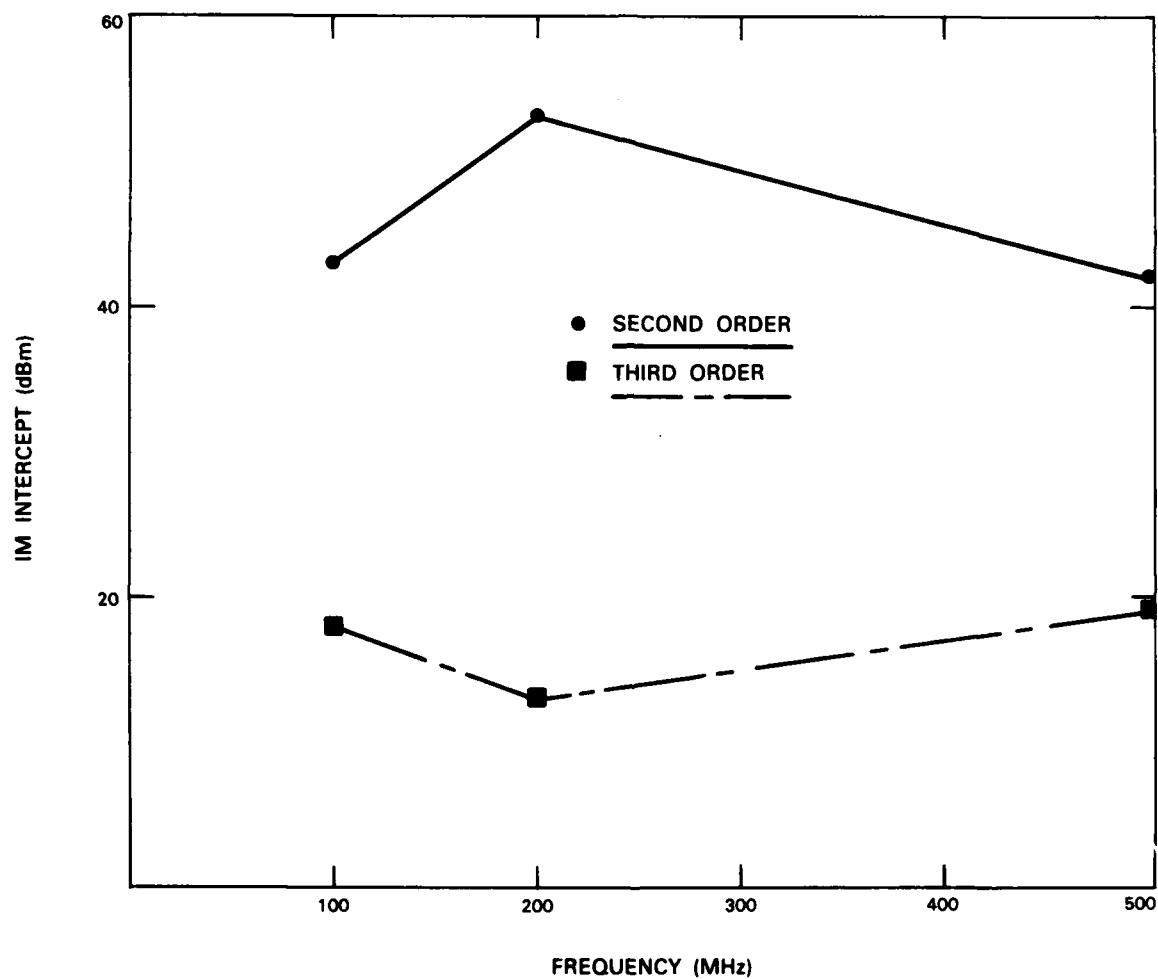


Figure 1-7. Plot of second- and third-order intercept points vs frequency for constant laser power of 4.5 mW.

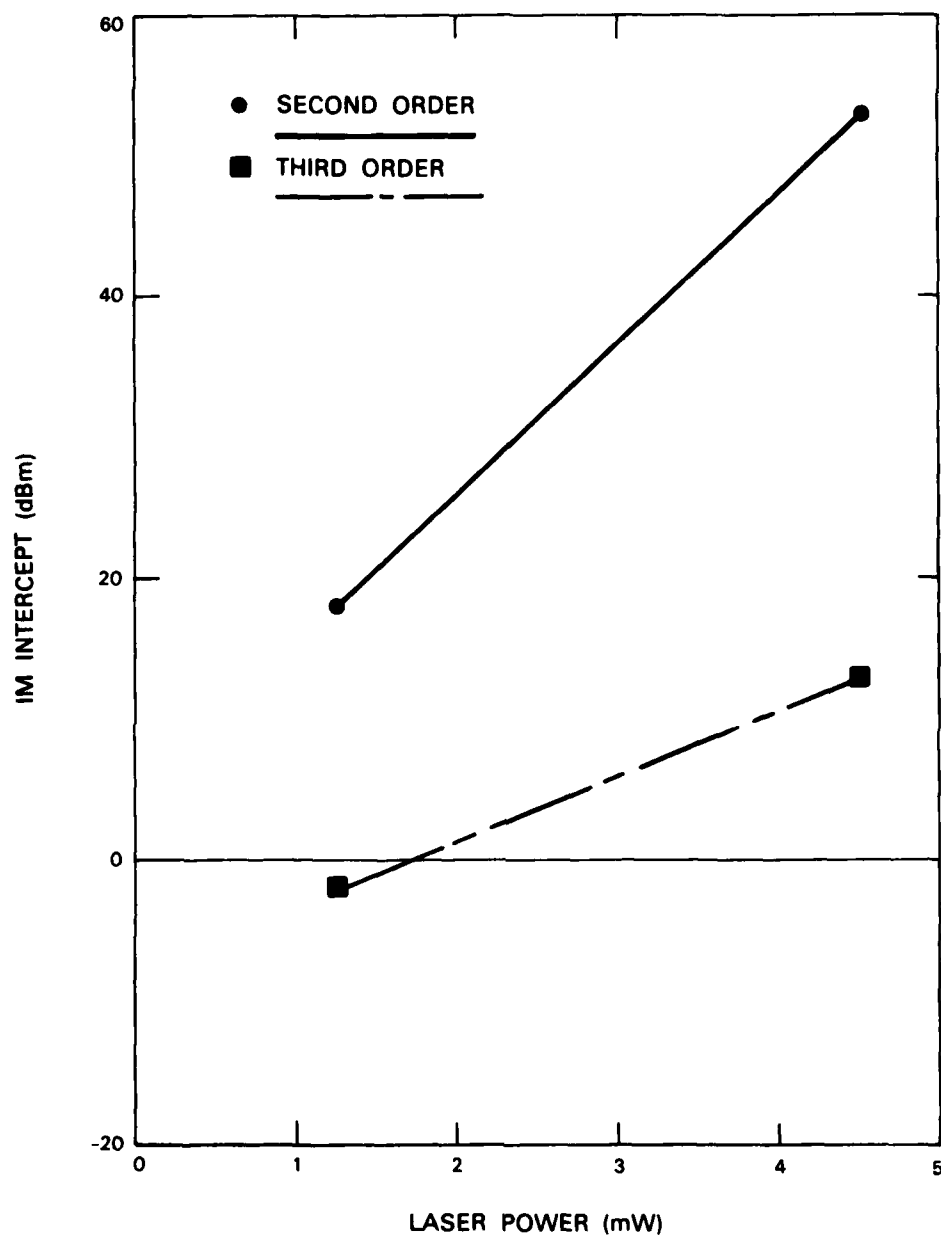


Figure 1-8. Plot of second- and third-order intercept points vs laser power for input frequencies of 197 and 203 MHz.

131051-R

third-order intercept points that result from a series of measurements identical to those shown in Figure 1-6 but for different RF input frequencies. The frequency coordinate of the intercept points used in Figure 1-6 is the arithmetic average of the input frequencies used. The relative independence of these initial measurements with respect to frequency suggests that the dynamic (RF) I-V curve is substantially the same as the static (DC) I-V curve shown in Figure 1-4.

The intercept points plotted in Figure 1-8 were measured at two different levels of illumination while the RF input frequency has held constant, ≈ 200 MHz. The increase in intercept level with increasing illumination is the combined result of two effects. At the higher illumination, the lower switch on-resistance reduces the insertion loss, thereby raising the amplitudes of the fundamental output. The higher illumination also increases the level at which the switch's I-V curve begins to saturate, thereby requiring a higher amplitude input in order to produce the same amplitude of intermodulation outputs.

C.H. Cox III
A.G. Foyt

V. Diadiuk
R.C. Williamson

1.3 CONTINUOUS MULTI-GIGAHERTZ MODULATION OF Q-SWITCHED GaInAsP DIODE LASERS

Diode lasers capable of producing short optical pulses at high rates are being developed for applications in communications and optical signal processing. Previously we have reported the pulsed operation of an intracavity-loss-modulated laser with a zinc-diffused stripe geometry amplifier section.^{2,3} We report here a CW diode laser with two electrically isolated buried-heterostructure sections that has been operated with full on/off modulation at 3 GHz. The device operation is based on a combination of gain switching and Q-switching in which both gain and loss are actively varied in a modulator section while an amplifier section is driven with a constant DC current.

The device, shown in Figure 1-9, is fabricated from a double-heterostructure wafer consisting of a p-InP cap layer, a nominally undoped GaInAsP active region, and an n⁺-InP buffer layer on an n⁺-InP substrate. The buried active region is formed by an etching and mass transport process.¹ The wafer is proton bombarded to produce a laser with a long amplifier section (≈ 200 μ m) and a short modulator section (≈ 50 to 100 μ m) electrically isolated by the high-resistivity bombarded region (20 μ m).

With uniform DC current density applied to each section, the laser threshold is as low as 17 mA. With a small forward voltage < 0.8 V in the modulator, such that no significant current injection occurs, the laser threshold for current through the amplifier is over 60 mA, three times that of the uniformly pumped laser.

Full on/off modulation up to 3 GHz has been seen at a forward bias of 0.8 V with only about 10 mW of microwave power applied to the modulator and about 60 mA of DC current applied to the amplifier (Figure 1-10). As the amplifier current was increased, subharmonic operation was seen at 1.5 GHz. A substantial increase in the peak signal level was noted at the subharmonic, an indication of energy storage and Q-switching.

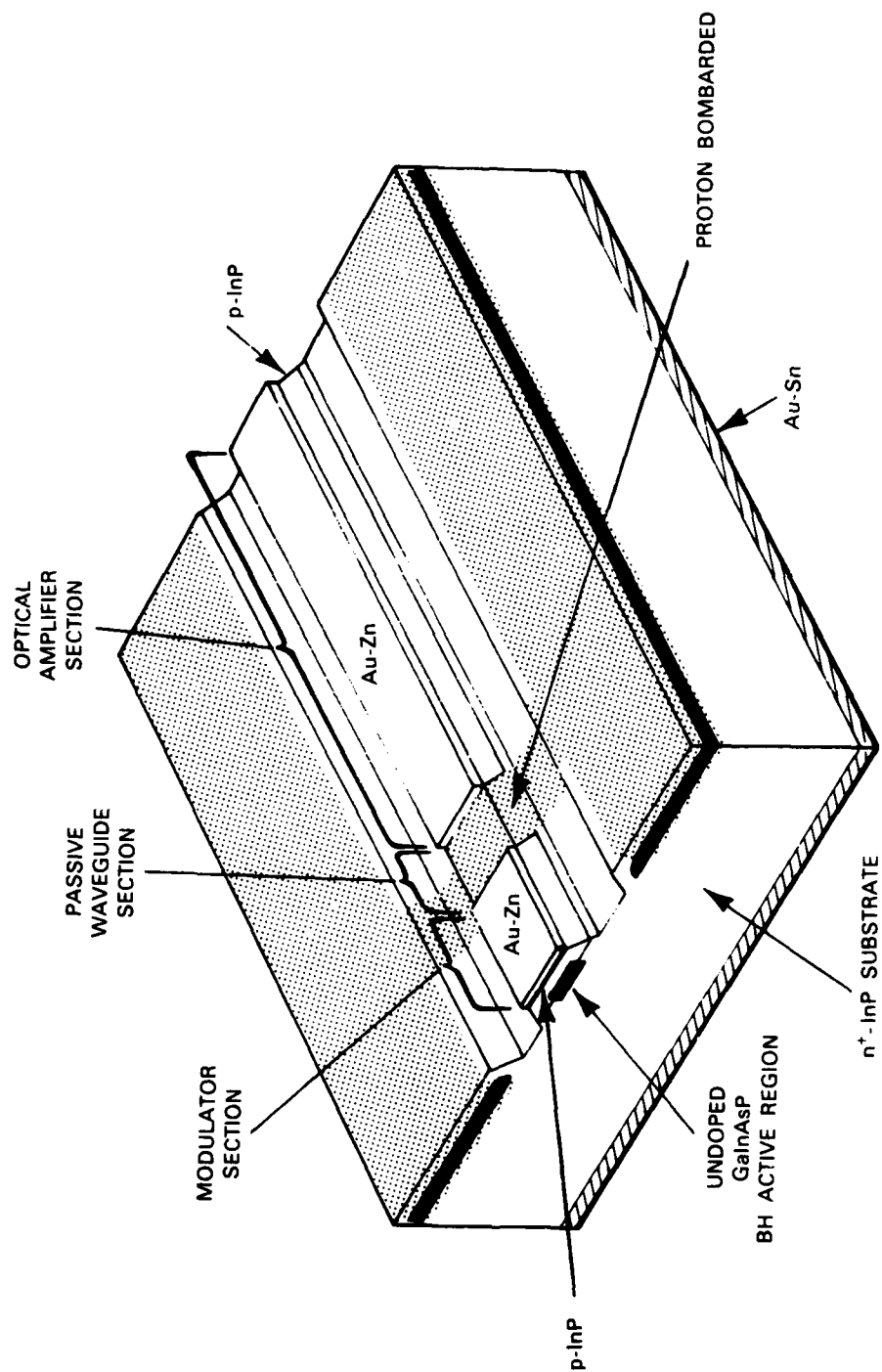


Figure 1-9. Schematic cross section of a Q-switched diode laser. The proton bombarded region extends below the active region to isolate the amplifier and the modulator.

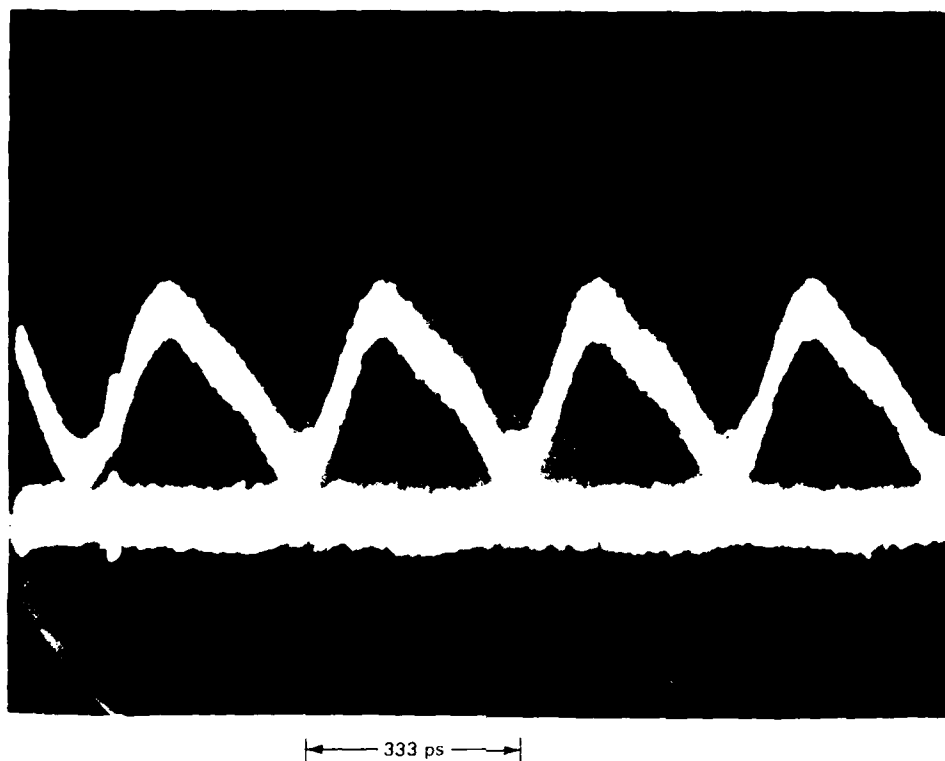


Figure 1-10. Detected output from a Q-switched diode laser with a proton-isolated modulator at 3 GHz. About 10 mW of microwave power is required for full off/on modulation.

Under modulation, significant forward current is injected into the modulator section to switch the modulator loss rapidly into gain. A Q-switched pulse can then rapidly build and dump the electron population in both sections. Since the turn-on time of the modulator is limited only by its capacitance and the drive current, while the turn-off time is dependent on the stimulated lifetime, operation well above a gigahertz is possible, depending on how hard the sections are driven. These low-threshold lasers are capable of producing short pulses at high rates with low microwave power requirements.

D.Z. Tsang
J.N. Walpole
Z.L. Liao

1.4 SEMI-INSULATING InGaAs OPTOELECTRONIC SWITCHES

Semi-insulating (SI) InP:Fe has proved to be useful for the fabrication of high-speed optoelectronic switches.⁴ Recent work by Clawson *et al.*⁵ has shown that it is possible to dope LPE InGaAs, lattice-matched to InP, with Fe and produce SI epitaxy. Here we report on our successful effort to grow such material and to utilize it in the fabrication of the first long-wavelength ($\lambda = 1.24 \mu\text{m}$) high-speed optoelectronic switches.

Epitaxial growth procedures involving extended growth solution baking, which normally produce material with net donor concentrations of $2 \times 10^{15} \text{ cm}^{-3}$ or less, were followed with the exception of the addition of $8 - 10 \times 10^{-4}$ atomic fraction of Fe (wire or powder of 5 - 9's purity) to the growth solution. Hall measurements at room temperature, carried out on the epitaxial InGaAs:Fe, yielded $\rho \approx 1260 \Omega\text{-cm}$ and net effective carrier concentration of $\approx 5.2 \times 10^{11} \text{ cm}^{-3}$. These correspond to a room-temperature mobility of $\approx 9600 \text{ cm}^2 \text{ V}^{-1}\text{s}^{-1}$, which is more than double that of bulk InP:Fe. These electrical characteristics make this material attractive for discrete as well as integrated photoconductive devices.

The discrete devices we have investigated consist of either single-gap ($\approx 10 \mu\text{m}$ wide) or interdigitated Au or Au-alloy electrodes (2-, 4-, and 6- μm finger width and spacing)⁴ e-beam evaporated directly onto the ternary epilayer. By using a He-Ne laser ($\lambda = 0.6328 \mu\text{m}$, $P \approx 2 \text{ mW}$), on-state resistances as low as 300Ω were measured on the 2- μm devices. The off-state resistance was $5 \times 10^4 \Omega$, as expected, several orders of magnitude lower than that obtained in InP. This difference is due to the lower InGaAs resistivity and implies that

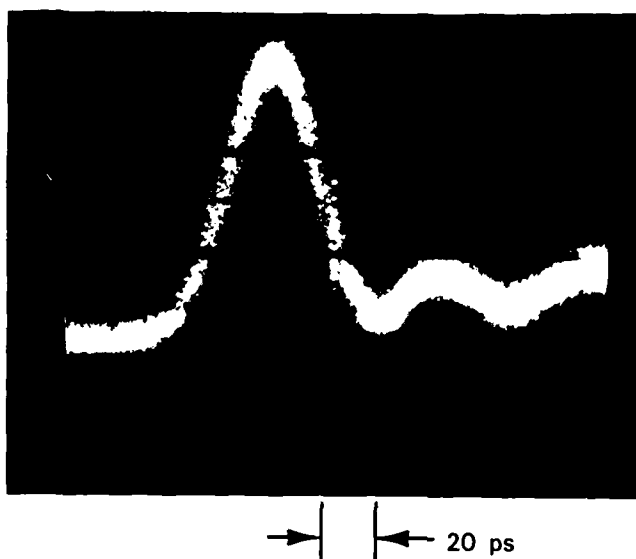


Figure 1-11. Pulse response of InGaAs:Fe optoelectronic switch to AlGaAs laser ($\lambda = 0.86 \mu\text{m}$) driven by a 100-MHz comb generator. Horizontal scale is 20 ps/div.

130271 R 01

these devices would not be suitable for the very high impedance applications, e.g., sample-and-hold circuits. On the other hand, InGaAs offers the advantages of higher mobility and sensitivity at long wavelengths. Furthermore, since the thickness of the epilayer can be chosen to be of the order of an absorption length, it is possible to make devices in which the entire depth of the device contains photogenerated carriers, leading to more uniform field distributions.

In order to measure the response time, the devices were mounted in microstrip packages and illuminated by 100-MHz comb-generator-driven AlGaAs and InGaAsP diode lasers. Figure 1-11 shows the pulse response obtained from a Au electrode, 10- μm single-gap device with $\lambda = 0.86\text{-}\mu\text{m}$ light incident upon it. This pulse shape exhibits a fast (FWHM ≈ 40 ps) component, but also a slow 90- to 10-percent fall time of ≈ 300 ps. Preliminary measurements indicate that the origin of this tail might be related to contact metallization and alloying; similar results were obtained at $\lambda = 1.23\text{ }\mu\text{m}$. To reduce the slow component and to optimize the device, an investigation of contact composition and alloying parameters is under way.

V. Diadiuk
S.H. Groves

M.C. Plonko
R.J. Bailey

1.5 BROADLY TUNABLE MODE-LOCKED HgCdTe LASERS

Tunable CW mode-locked laser action at $\lambda = 1.2$ and $\lambda = 1.73$ to $2.0\text{ }\mu\text{m}$ has been obtained from 4- to 8- μm -thick HgCdTe layers pumped longitudinally by a Nd:YAG laser. Peak output powers of 50 W, using a chopped-beam, and a CW mode-locked average output power of 5.6 mW have been achieved at a wavelength of $1.2\text{ }\mu\text{m}$. Near-bandwidth-limited pulses of 6-ps duration have also been obtained. Tuning from $\lambda = 1.82$ to $2.0\text{ }\mu\text{m}$ via the Burstein-Moss shift has been accomplished on a single epilayer by varying the loss in the external cavity.⁶

R.S. Putnam*
M.M. Salour*
T.C. Harman

*Department of Electrical Engineering and Computer Science and Research Laboratory of Electronics, Massachusetts Institute of Technology.

REFERENCES

1. Z.L. Liao and J.N. Walpole, Appl. Phys. Lett. **40**, 568 (1982), DTIC AD-A121779.
2. D.Z. Tsang, J.N. Walpole, S.H. Groves, J.J. Hsieh, and J.P. Donnelly, Appl. Phys. Lett. **38**, 120 (1981), DTIC AD-A103344/8.
3. Solid State Research Report, Lincoln Laboratory, M.I.T. (1981:2), pp. 1-3, DTIC AD-A110947/9.
4. A.G. Foyt, F.J. Leonberger, and R.C. Williamson, Appl. Phys. Lett. **40**, 447 (1982), DTIC AD-A121766.
5. A.R. Clawson, D.I. Elder, and H.H. Wieder, 2nd NATO Workshop on "Materials Aspects of InP," Lancaster, England, March 1983.
6. R.S. Putnam, M.M. Salour, and T.C. Harman, Appl. Phys. Lett. **43** (September 1983).

2. QUANTUM ELECTRONICS

2.1 Ti:Al₂O₃ LASER: RECENT ADVANCES

The Ti³⁺:Al₂O₃ laser described previously¹ has been operated with high laser quantum efficiency and has been tuned over a considerable fraction of the potential tuning range. In addition, quasi-CW operation has been attained at room temperature, with true CW operation observed from a cryogenically cooled crystal.

Figure 2-1 shows the output- vs absorbed-input-energy curves for a room-temperature Ti:Al₂O₃ laser, pumped longitudinally by ~300-ns-wide pulses from a flashlamp-pumped dye laser operating at 587 nm with rhodamine 6G dye. The Ti:Al₂O₃ laser output was at 750 nm in a nearly diffraction-limited beam; the laser cavity consisted of a concave 25-cm-radius highly reflecting mirror and a flat partially transmitting output mirror, spaced 15 cm apart. The laser crystal was 2 cm in length, doped with approximately 0.1% Ti³⁺, and had polished flat and parallel surfaces anti-reflection coated at 750 nm. In Figure 2-1, results are shown for two different values of output coupling. From the ratio of thresholds (1.65) between the high- and low-transmission couplers, one calculates an excess loss in the cavity of ~20 percent. If all this loss is due to scattering in the crystal, the crystal loss coefficient is 0.05 cm⁻¹. The predicted laser quantum efficiency, i.e., the ratio of output photons to absorbed pump photons for the high-transmission coupler is ~65 percent, compared to the observed 50 percent. The discrepancy may be due to suboptimal coupling between the laser and pump transverse modes, the latter of which had more intensity in the periphery of the beam than in the center.

In other experiments, a Ti:Al₂O₃ laser cavity with two intracavity, Brewster-angle prisms was constructed to determine the Ti:Al₂O₃ laser tuning range. The cavity geometry was confocal with a 25-cm mirror spacing and a 6-percent transmission output coupler. The tuning range observed was from 687 to 821 nm, limited to some extent by the finite bandwidth of the mirrors. Additional experiments are in progress to extend the operating range farther with alternate cavity optics. The current range extends to approximately the half-power points of the fluorescence spectrum.¹

Some preliminary work was done on CW pumping of a Ti:Al₂O₃ laser. The pump in this case was an argon-ion laser operating on all lines in the blue-green wavelength region. The 3.2-cm-long crystal used in this case was doped with ~0.02% Ti³⁺ and conduction-cooled on a copper heatsink, which could in turn be cooled by liquid nitrogen. The laser cavity was of confocal geometry with a 25-cm spacing and had ~1 percent output coupling. True CW operation was observed with liquid-nitrogen cooling, used primarily to enhance the thermal conductivity of the Al₂O₃ host crystal; 70 mW of power at 750 nm was generated for 10 W of incident power. Quasi-CW operation with a threshold peak power of 9.8 W was observed with the crystal at room temperature by chopping the pump beam at a 16-percent duty cycle; a peak output power of 44 mW was obtained at 12.5 W of pump power. Calculations show that CW operation from the Ti:Al₂O₃ laser should be possible at room temperature with less than 1 W of pump power from an argon-ion laser by improving the crystal heat-sinking and use of an optical cavity with a smaller mode size.

P.F. Moulton

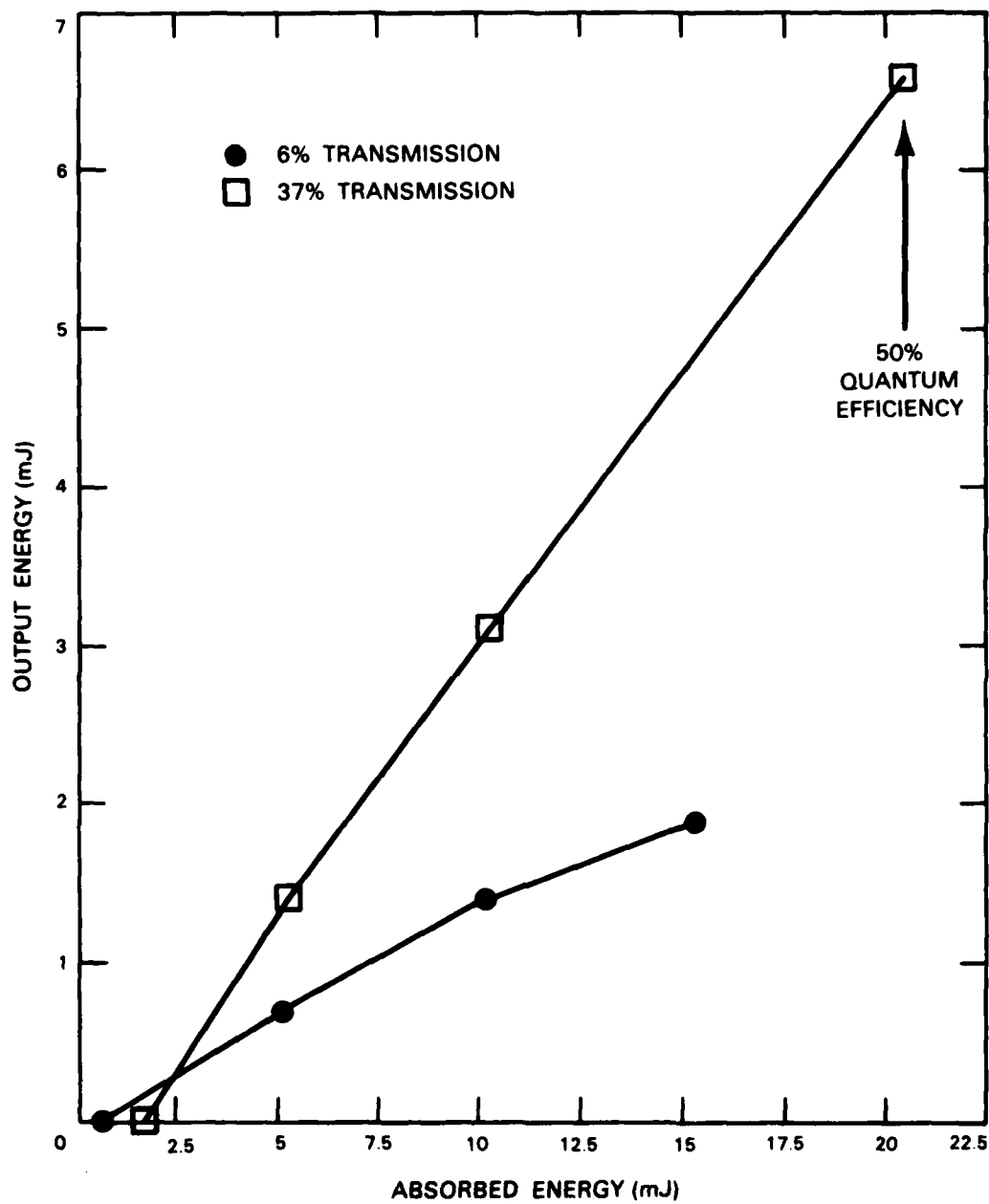


Figure 2-1. Output energy vs absorbed input energy for pulsed Ti:Al₂O₃ laser, for two different output-mirror transmissions. The pump and laser wavelengths were 587 and 750 nm, respectively.

131062 N

2.2 GAIN IN V:KMgF₃

The room-temperature gain of V:KMgF₃ at the standard Nd:YAG-laser wavelength, 1.0645 μm , has been measured by a pump-probe experiment. A 1.25-cm-long crystal of ~ 1 -percent-doped V:KMgF₃, conduction-cooled on a copper heatsink, was pumped optically by the focused beam of a TEM₀₀-mode, 0.5145- μm -wavelength argon-ion laser. A probe beam from a CW, TEM₀₀-mode Nd:YAG laser, aligned (using a set of apertures) to be exactly collinear with the pump beam, also passed through the crystal. The probe beam was detected by a large-area silicon photodiode to minimize any effects of beam steering or lensing caused by thermal gradients in the crystal. A variable-frequency optical chopper was used to modulate the pump beam, and the resultant signal induced in the probe beam was detected by a lock-in amplifier. Figure 2-2 shows the gain (expressed as a percentage of the probe signal) as a function of pump power incident on the crystal, for a chopper frequency of 55 Hz. The probe beam power was approximately 100 mW. The gain reduction at high powers may be related to heating effects. Observation of the phase of the fluorescence signal from the crystal (detected using another silicon photodiode) compared with the phase of the gain signal showed that the gain was indeed positive. With the probe beam blocked no gain signal was detected, indicating that the fluorescence background was negligible.

To check that the measured signal was related entirely to stimulated emission and not to some other processes, the magnitude of the gain signal at constant pump power (in the linear region of Figure 2-2) was observed as a function of chopping frequency. Because of the relatively long lifetime of the 4T_2 level (~ 1 ms) the pump-induced modulation of the inversion density should diminish at higher frequencies. If the pump beam was modulated with a sine wave (instead of the actual square wave) one would expect a 3-dB rolloff in amplitude at a frequency of ~ 1000 rad/s or ~ 167 Hz. To check that the gain signal had the proper frequency response, it was compared with the response of the detected fluorescence signal to varying chopper frequency. Figure 2-3 shows the relative response of both gain and fluorescence signals; the essentially equivalent response curves indicate that the gain signal was directly related to the modulation of the upper level population.

A set of calibrated apertures was used to determine spot size of both the probe and pump beams at the crystal location. The transmission, T , of a Gaussian mode through an aperture of diameter, d , can be used to find the mode characteristic radius, w , from the following relation:

$$w = \frac{d}{2} \left[\frac{-2}{\ln(1 - T)} \right]^{1/2} \quad (2-1)$$

For the probe beam, apertures with diameters of 32, 108, and 140 μm yielded values for w of 122, 117, and 119 μm , respectively, while for the pump beam, with apertures of diameters 21, 32, and 51 μm , the w values determined were 34, 36, and 31 μm , respectively. The relatively small variation in calculated spot size for different aperture sizes indicated that measurement technique was reasonably precise.

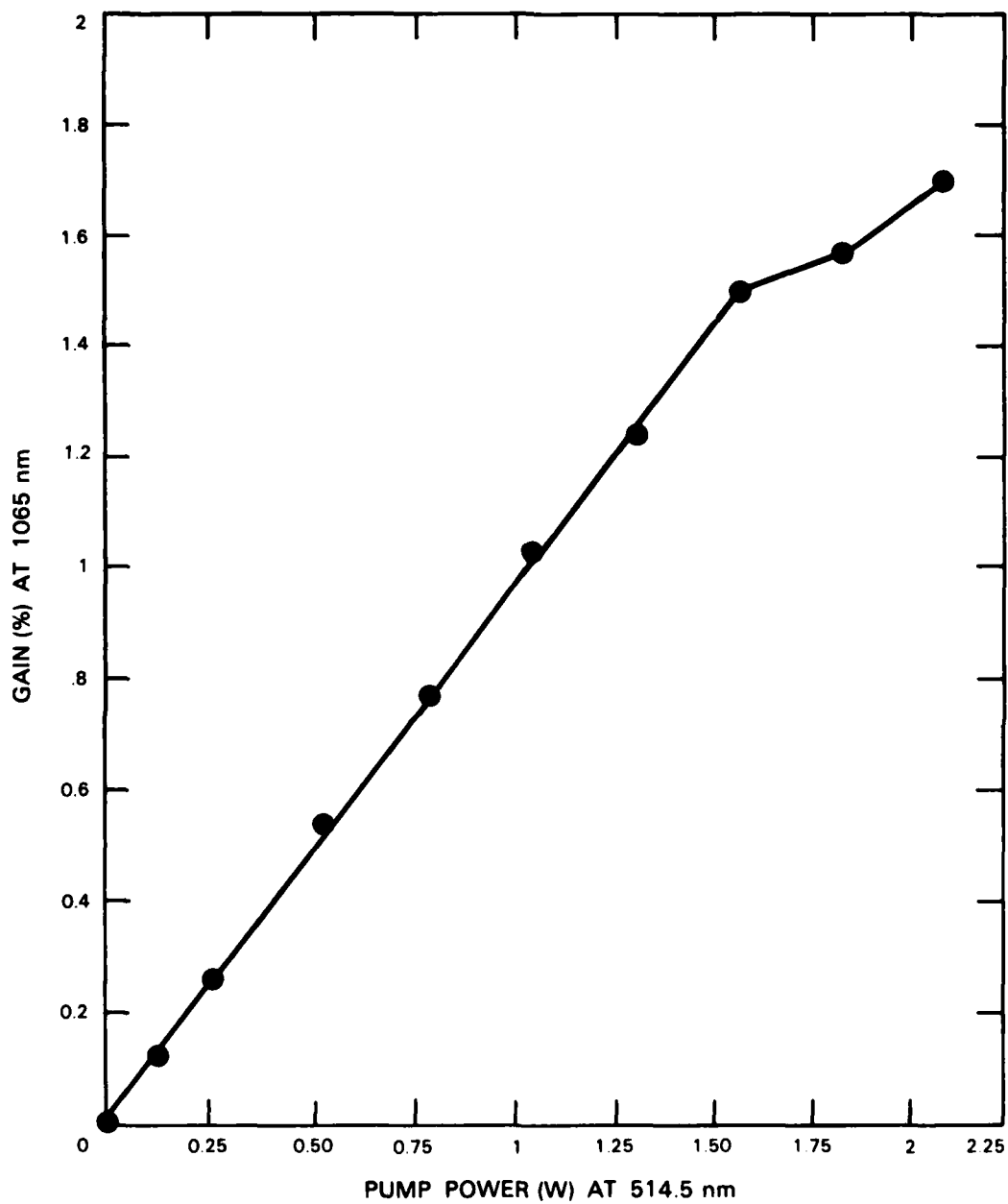


Figure 2-2. Percentage gain in V:KMgF₃ as a function of pump power for a chopper frequency of 55 Hz. The lighter section of the curve is a best-fit straight line to the points shown.

131053 N

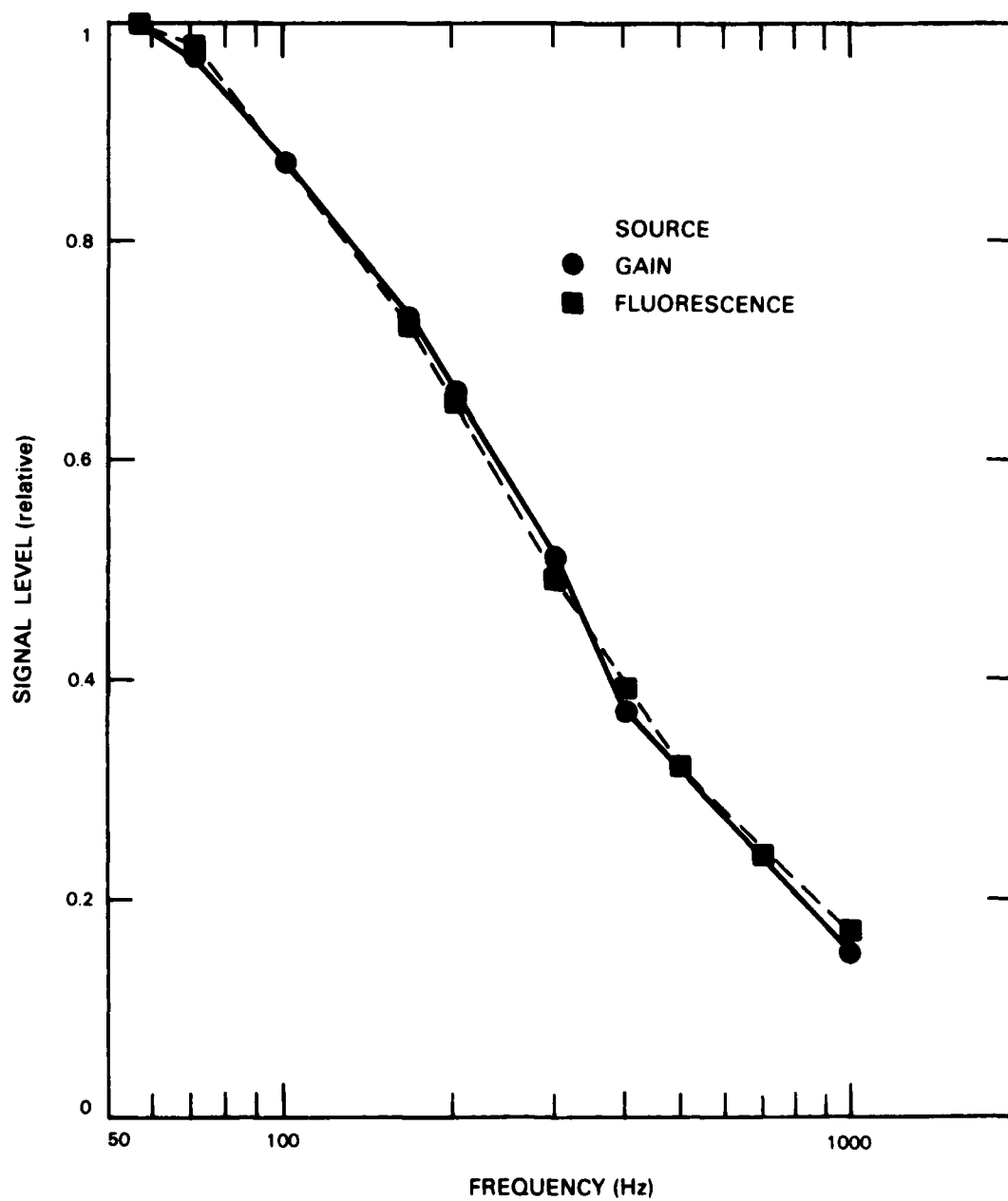


Figure 2-3. Gain and fluorescence signal levels as a function of chopper frequency, for constant pump power.

The measured pump beam transmission through the crystal was 0.46. When one accounts for Fresnel losses this implies an absorption coefficient of 0.56 cm^{-1} . The probe beam transmission was 0.85; with Fresnel losses accounted for, the loss coefficient at $1.065 \mu\text{m}$ is 0.065 cm^{-1} , due possibly to scattering in the crystal. Some of the measured loss at the pump wavelength is also likely due to scattering rather than absorption via the $^4A_2 \rightarrow ^4T_1$ transition, which increases the uncertainty in the calculations given below.

Assuming Beer's law attenuation of the pump beam and a Gaussian intensity distribution, the gain coefficient function in the crystal, $g(r,z)$, is given by

$$g(r,z) = \frac{2P\sigma\tau\alpha_p}{\pi h\nu_p w_p^2(z)} \exp [-2r^2/w_p^2(z) - \alpha_p z] \quad (2-2)$$

where P is the pump power incident on the crystal (corrected for the Fresnel loss), α is the gain cross section, τ is the upper-state lifetime, α_p is the pump absorption coefficient, ν_p is the pump frequency, r is the transverse radial coordinate, and z is the distance along the length of the crystal measured from the entrance face. The pump spot-size function, $w_p^2(z)$, is given by

$$w_p^2(z) = w_{p0}^2 \left[1 + \left(\frac{\lambda_p z}{\pi n w_{p0}^2} \right)^2 \right] \quad (2-3)$$

where n is the refractive index and it is assumed that the beam focus is at $z = 0$. Assuming that the gain is small, the fractional gain measured, G , is given by

$$G = 4 \int_0^{\ell} dz \int_0^{\infty} r dr \frac{g(r,z)}{w_s^2(z)} \exp \{-2r^2/[w_p^2(z) + w_s^2(z)]\} \quad (2-4)$$

where ℓ is the crystal length and $w_s^2(z)$ is the spot-size function for the probe beam.

An approximation to G can be easily obtained by neglecting the z -dependence of w_p and w_s and taking the limit of large w_s/w_p . Then,

$$G = \frac{2P\sigma\tau}{\pi w_s^2 h\nu_p} [1 - \exp(-\alpha_p \ell)] \quad (2-5)$$

or

$$\sigma = \frac{\pi w_s^2 h\nu_p G}{2P\tau} [1 - \exp(-\alpha_p \ell)]^{-1} \quad (2-6)$$

Using previously discussed values for the parameters above, and a value for G of 5.4×10^{-3} at a P of 0.52 W, one finds a value for σ of $1.6 \times 10^{-21} \text{ cm}^2$.

To test the validity of the approximations used for Eq.(2-6) a direct numerical calculation of Eq.(2-4) was carried out on a computer. The only approximation used was the assumption of a constant, w_s , which is valid since the confocal parameter for a 120- μm spot size in the crystal is $\sim 12 \text{ cm}$. The resultant value for σ is $1.78 \times 10^{-21} \text{ cm}^2$.

The Einstein relation can be used to relate σ at the peak of the gain curve to the fluorescence lifetime under the assumption of unity fluorescence quantum efficiency. The equation (only approximate for a system with a broad fluorescence line such as V:KMgF₃) is

$$\sigma = \frac{\lambda_m^4}{8\pi\Delta\lambda n^2 c \tau} \quad (2-7)$$

with λ_m and $\Delta\lambda$ the wavelength at the peak and full-width half-maximum of the gain spectrum, respectively, and c the speed of light. Using the available fluorescence data, one calculates $\sigma \sim 4.4 \times 10^{-21} \text{ cm}^2$.

It is perhaps premature to account for all the discrepancy between measured and predicted gain cross section by invoking excited-state absorption, given the poor quality of available crystals.² Work is continuing to improve crystal quality by removing H₂O from the initial KF charge.

P.F. Moulton

2.3 CONTINUOUS-WAVE ACTIVELY MODE-LOCKED Co:MgF₂ AND Ni:MgF₂ LASERS

Active mode-locking of continuous-wave Ni:MgF₂ and Co:MgF₂ lasers has been reported previously;^{3,4} however, the performance of these lasers was not fully examined. Here we report a more detailed study in which the tunability of these lasers has been demonstrated, and autocorrelation pulse width measurements over the tuning range have been made.

Measurements of pulse width as a function of wavelength were made for both the Co:MgF₂ and Ni:MgF₂ lasers, and the results are plotted in Figures 2-4 and -5. A sample autocorrelation trace obtained from the Co:MgF₂ laser is shown in Figure 2-6. Pulse width figures were obtained by multiplying the autocorrelation function FWHM by $2^{-1/2}$, the factor appropriate for Gaussian pulses. The cavity length was adjusted for the maximum stable second-harmonic signal in an effort to achieve the shortest pulses when these measurements were made. The autocorrelations used for the pulse width data of Figures 2-4 and -5 have the sharp tails characteristic of Gaussian pulses, and little additional structure. The autocorrelations do not exhibit a "correlation spike" characteristic of pulses with noisy substructure. The laser pulses have been observed to be either Fourier transform limited or not, depending on cavity length, but not in a systematic manner. Periodic structure in the frequency spectrum measured with a spectrometer is exhibited by the laser when emitting non-transform-limited pulses. This behavior is similar to "clustering" effects seen in mode-locked diode lasers where the effect is produced by residual reflections from AR-coated diode chips

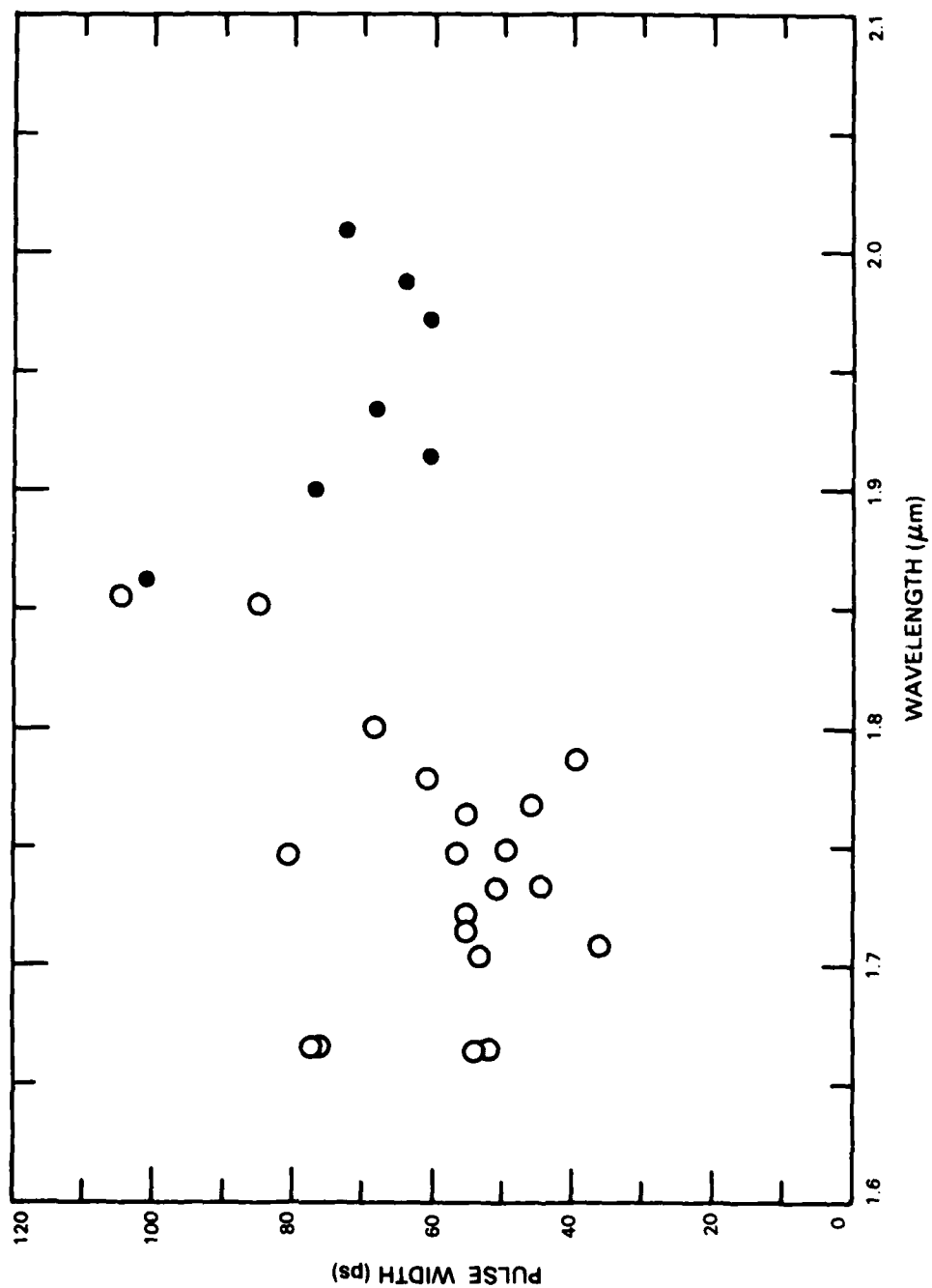


Figure 2-4. Plot of pulse width vs wavelength for Co:MgF₂ laser. The two datapoint symbols represent data with different sets of cavity mirrors.

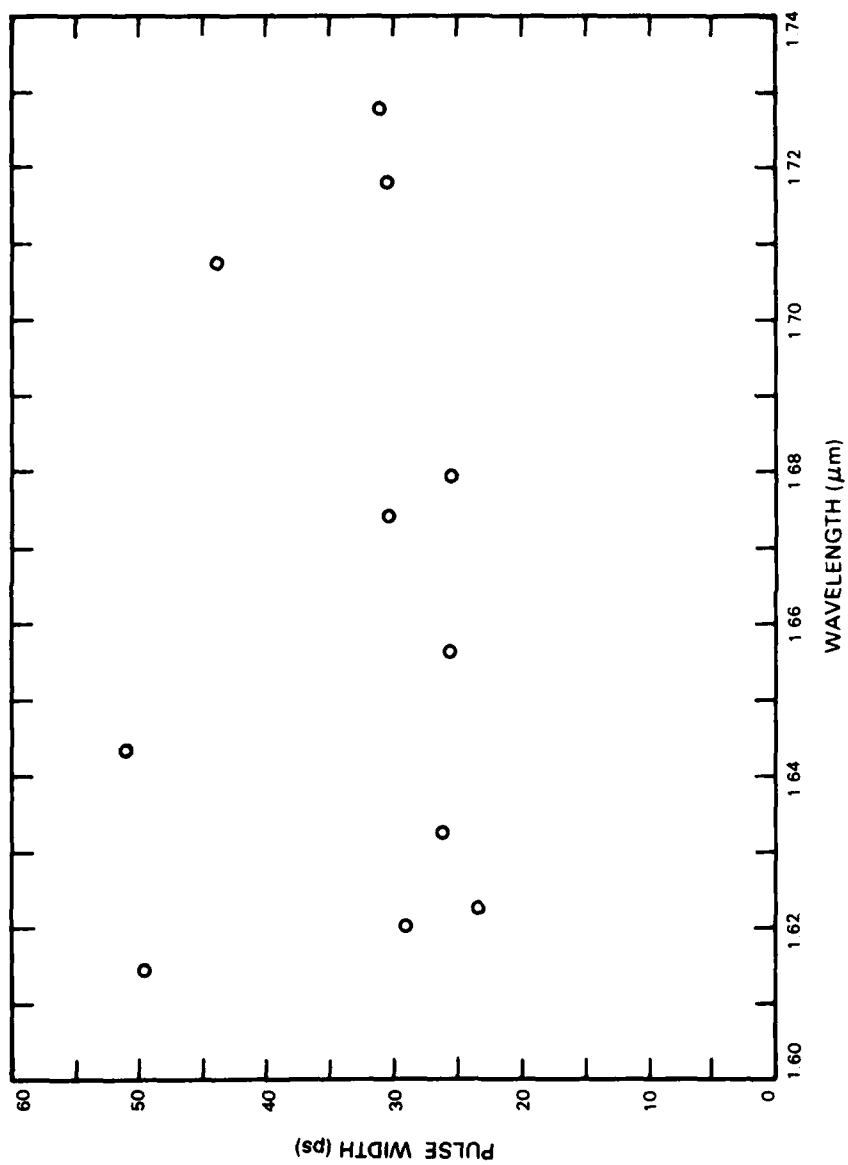


Figure 2-5. Plot of pulse width vs wavelength for Ni:MgF₂ laser.

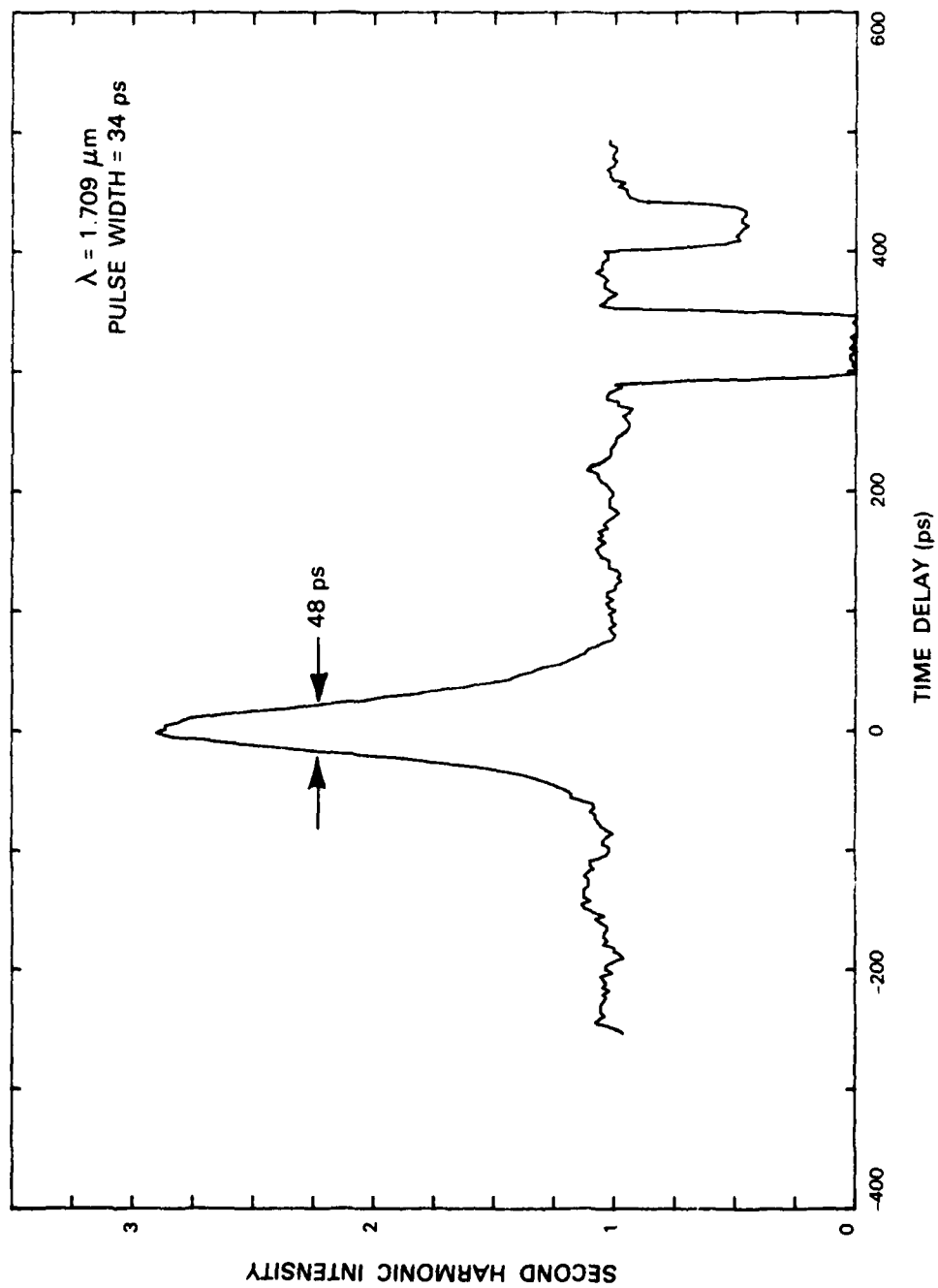


Figure 2-6. Autocorrelation trace of shortest pulse from the Co:MgF₂ laser.

128448 R-01

in the external cavity.⁵ Periodicities of ~ 0.08 and ~ 0.75 nm are commonly seen corresponding to ~ 13 and ~ 1.5 mm lengths of quartz. This means the tuning plate and one of the cavity mirrors are probable sources of small reflections. With the low gain in these systems, even extremely small reflections of this type can cause clustering; however, the problem is not a fundamental one and could be solved through more careful design of the laser. Such an improvement should result in better pulse width performance.

The variation in pulse width as a function of wavelength may reflect properties of the optics and gain medium. The large pulse widths around $1.85 \mu\text{m}$ for the Co:MgF₂ laser occur where the cavity mirror reflectivities begin to fall off. Spectral structure in the gain medium also seems to play a role. The gain spectrum at 77 K exhibits a number of peaks superimposed on a broad background. These gain peaks are associated with purely electronic transitions while the vibronic sidebands accompanying the electronic transitions provide the background. Longer than average pulses are seen at 1.667 , 1.750 , and $1.805 \mu\text{m}$ in Co:MgF₂ and at $1.703 \mu\text{m}$ in Ni:MgF₂, which correspond to gain curve local maxima. Data points clustered around these wavelengths with very different pulse lengths represent different tuning plate angles. The laser oscillation frequency pulls slightly toward large gain peaks resulting in the insensitivity of wavelength to tuning-plate angle in these regions. This pulling can be reduced with more selective tuning elements, although at the expense of broadening the pulses. Measurements of wavelength vs tuning-plate angle indicate the Ni:MgF₂ system has a slightly smoother tuning curve than Co:MgF₂; this may explain the generally shorter pulses produced by the Ni:MgF₂ laser. The theory of Kuizenga and Siegman⁶ predicts the pulse width to be

$$\Delta t = [(\sqrt{2} \ln 2)^{1/2} / \pi] (g/\delta)^{1/4} (f_m \Delta f)^{1/2}$$

where g/δ is the ratio of gain to modulation depth, f_m the modulation frequency, and Δf the effective bandwidth of gain medium and tuning element. The bandwidths for these systems are estimated to be in the 1000- to 5000-GHz range, indicating pulse widths as short as 10 ps should be possible. The theory, however, does not apply to lasers with clustering problems since it assumes a smooth Lorentzian gain curve. It is expected that a system free of residual reflection problems would produce pulses in the predicted range.

In conclusion, the performance of actively mode-locked Co:MgF₂ and Ni:MgF₂ lasers has been measured and reliable mode-locked operation from 1.65 to $2.01 \mu\text{m}$ has been demonstrated. We feel that improvements in stability of the system and more careful optical design to prevent clustering effects will result in pulses closer to the limit presented by the Kuizenga and Siegman theory. Even so, these pulses are close to the width achieved by any actively mode-locked system, and are significantly shorter than those of Nd:YAG. Scaling these lasers to higher power should allow efficient frequency doubling to provide tunable picosecond radiation over the 0.8 - to $1.1 \mu\text{m}$ spectral region in addition to the wavelength range of the fundamental radiation.

B.C. Johnson
P.F. Moulton
A. Mooradian

2.4 UV LASER PHOTOPOLYMERIZATION OF VOLATILE SURFACE-ADSORBED METHYL METHACRYLATE

In studies of laser photochemistry on surfaces, the photoreactions of surface-adsorbed molecular layers have been found to have a number of important implications. For the photodeposition of metals, in particular, it has been found that such adlayers can be used to control nucleation kinetics and thereby to achieve submicrometer spatial resolution. We recently have found a process in which the photochemistry is completely confined to such molecular adlayers. Specifically, adsorbed layers of the small organic molecule methyl methacrylate (MMA) are polymerized into localized films of poly(methyl methacrylate) (PMMA), a high-quality polymer used extensively in the definition of high-resolution thin-film and substrate patterns by etching and lift-off techniques.

The photochemical mechanism is a free-radical-catalyzed polymerization initiated by absorption of UV-laser light by the volatile molecular layers which form on surfaces exposed to an ambient MMA vapor. At the 1- to 30-Torr pressures used in the present study, rapid collisions of vapor-phase molecules with the surface continually replenish the polymerizing adsorbed MMA and permit rapid PMMA growth. Without sensitization the polymerization equilibrates with chain-degradation and radical quenching reactions at net deposition rates of ~ 40 nm/s. With sensitization increased rates of up to $1 \mu\text{m/s}$ are achieved.

In our experiments an inverted high-power microscope is used to focus the 257.2-nm output (1 to $1000 \mu\text{W}$) of a frequency-doubled Ar-ion laser through a 5-mm-path-length vapor cell to spot sizes of 0.8 to $3 \mu\text{m}$ on Si and SiO_2 substrates. Typical intensities on the substrates were 1 to 10 kW/cm^2 - insufficient to cause substrate heating exceeding several degrees Celsius. The substrates were scanned, under computer control, by precision stepping-motor-driven translation stages. The MMA, a liquid with a ~ 30 -Torr vapor pressure at room temperature was vacuum distilled prior to use to remove a hydroquinone inhibitor. Throughout the 1- to 30-Torr pressure range, the laser-beam irradiation results in well-defined local deposition of a polymer with the physical properties of moderate molecular weight PMMA. In particular, it is insoluble in many inorganic aqueous etching solutions, although easily stripped in organic solvents such as acetone.

Using this process a variety of substrate and film patterning sequences have been demonstrated. As a first step, a PMMA film with a thickness of 50 to 500 nm was grown by scanned UV-laser irradiation. The sensitized compound adsorbed layer used in this step is shown in Figure 2-7; the sensitizing layer is formed by an initial exposure of the SiO_2 substrates to $\text{Cd}(\text{CH}_3)_2$ vapor. Prior to UV irradiation the $\text{Cd}(\text{CH}_3)_2$ is carefully evacuated and MMA is introduced. From previous quartz-microbalance measurements, this is known to leave a single chemisorbed monolayer of the organometallic between the substrate and the MMA layer. Polymerization rates are greatly accelerated by a surface catalytic effect, as discussed below.

The deposited PMMA film is then used much in the manner of a negative resist, although no prior spin-on or subsequent development steps are required. To pattern Al films, the PMMA was either written directly on the metal surface, or on surfaces which

were first overcoated with a ~ 100 -nm thickness of plasma-deposited SiO_2 . With no intermediate SiO_2 layer, the metal pattern was etched without further processing in a $\text{KOH}:\text{K}_3\text{FeCN}:\text{H}_2\text{O}$ solution; minimum linewidths for $1\text{-}\mu\text{m}$ -thick sputtered Al were limited to $\sim 5\text{ }\mu\text{m}$ by slow lift-off of the polymer in this etchant. Features as small as $\sim 1\text{ }\mu\text{m}$ were produced using the intermediate SiO_2 layer. In this case the laser-written PMMA pattern was first transferred into the SiO_2 using an HF etchant, and then the SiO_2 was used to mask the Al etch. A similar sequence was used to pattern features in SiO_2 over Si substrates. The patterned SiO_2 was then used as a durable mask for subsequent processing, much as in a multilevel resist sequence. As an example, Figure 2-8 shows $0.8\text{-}\mu\text{m}$ -linewidth relief transferred into Si by reactive-ion etching. For the latter example, feature sizes are limited by the optical resolution of the laser deposition system; the edge roughness in Figure 2-8 is attributed largely to mechanical vibrations of the translation stages.

The mechanism of the polymerization has been examined in a series of separate experiments. The importance of adlayer photochemistry was studied using a quartz-crystal microbalance to measure both MMA surface coverage and polymerization rate as functions of pressure. Surface-coverage data were recorded as mass changes on a PMMA-covered surface. At 23°C , multilayer adsorption begins as the MMA pressure is increased above ~ 10 Torr, although slight warming reduces the coverage greatly. For example, the coverage at 29 Torr is reduced by a factor of ~ 3 on warming to 28°C , reflecting relatively weak, Van-der-Waals-type bonding for both the first and subsequent adsorbed monolayers. The shape of the adsorption isotherm is characteristic of adsorption on SiO_2 and Au as well as on PMMA

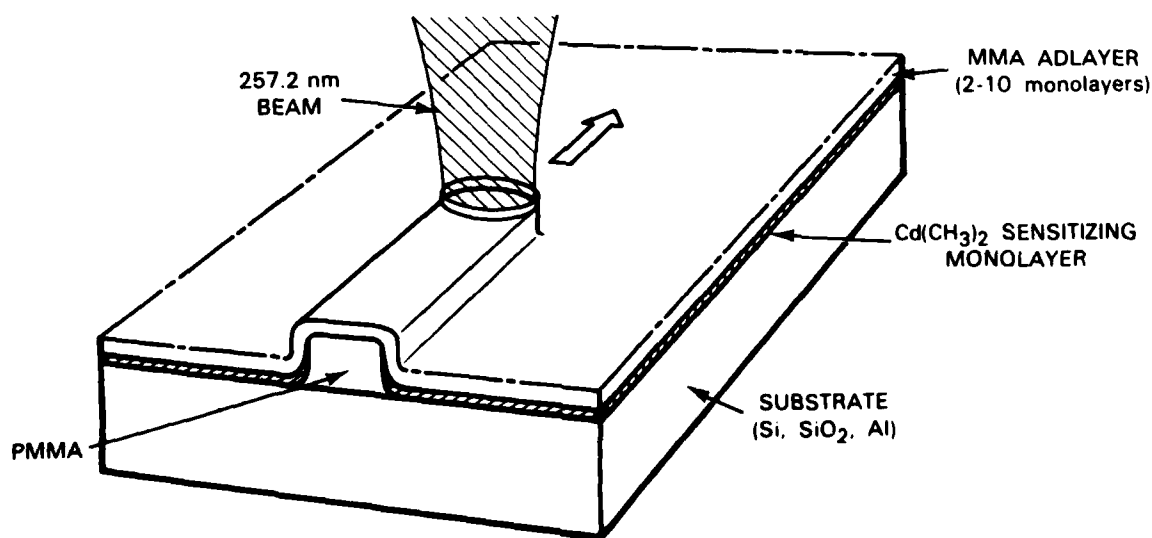


Figure 2-7. Two-component adsorbed multilayer used in laser photopolymerization. The volatile MMA layers equilibrate rapidly with the MMA-vapor ambient.

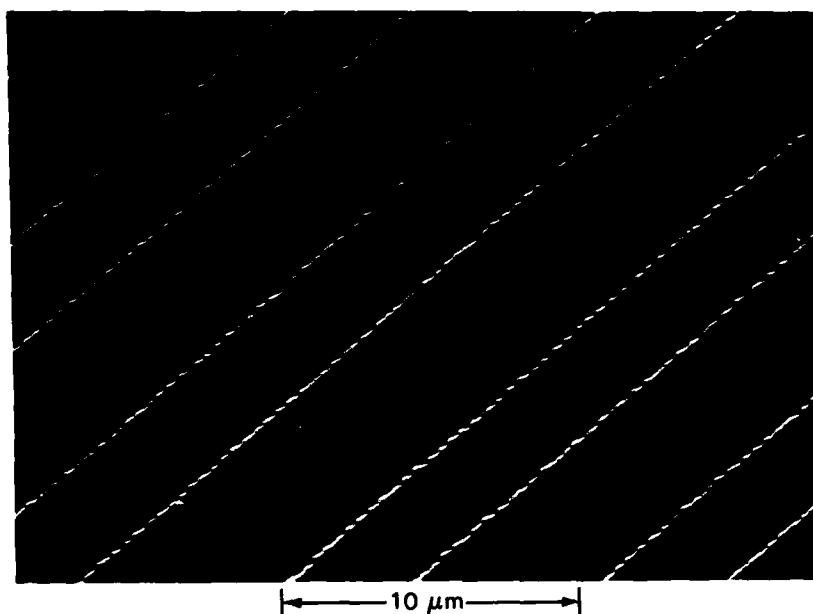


Figure 2-8. Electron micrograph of positive relief in (100) Si. Laser-deposited PMMA was used to mask a two-step wet and dry etching sequence (see text).

131055-S

surfaces. Photopolymerization-rate measurements were made by irradiating the microbalance surface through a 2-cm path length of MMA vapor with the 253.7-nm output of a low-pressure Hg lamp. The strong correlation of adlayer coverage to changes in pressure or temperature indicates that this rate is controlled by chemical kinetics in the adsorbed layer rather than in the vapor. A detailed comparison indicates slightly greater absolute reaction efficiencies in thicker adlayers.

The mechanism of confinement of the photoreaction to the adsorbed molecular layers is apparently particular to the present process. Similar, dominantly surface photochemistry observed for laser photodeposition of metals has been ascribed partially to pronounced spectral shifts in light absorption by surface-adsorbed molecules. To test for this the UV spectrum of liquid MMA was measured, under the assumption that the liquid-phase and weakly bound-adlayer molecular environments are nearly equivalent. A 257.2-nm absorption cross section of $1.8 \times 10^{-19} \text{ cm}^2$, almost identical to that of vapor-phase MMA ($1.7 \times 10^{-19} \text{ cm}^2$), was found. We conclude that the polymerization is favored by some more complex surface-catalytic process, such as multimolecular collisions in the condensed adlayer phase.

In summary, the polymerization process described here is the first clear example of a photochemical laserreaction which occurs selectively in a volatile adlayer. The new negative resist technique has applications as a mask-free fabrication process, and as a procedure for local modification and fault-correction on electronic devices with submicrometer resolution, without the introduction of secondary lithography-related defects. For example, the process has recently been applied to custom metallization of Si metal-oxide-semiconductor field-effect transistors.

J.Y. Tsao
D.J. Ehrlich

2.5 SELF-DEVELOPING UV PHOTORESIST USING EXCIMER LASER EXPOSURE

We recently have reported that nitrocellulose can function as a self-developing resist sensitive to both low-energy ion beams and to 193-nm UV excimer laser radiation; however, the results of the laser experiments were only summarized briefly.⁷ Used as a UV resist material, nitrocellulose has higher contrast than most conventional photoresists, exhibits submicrometer resolution, and has properties compatible with many semiconductor processing operations. A resolution of at least 0.3 μm , substantially higher than previously reported,⁸ has been demonstrated. The self-developing property of the resist results from the fact that it can be decomposed into volatile products by sufficiently intense UV irradiation; similar excimer laser ablation of relatively thick polymer films has been reported by others.⁸

Nitrocellulose films having thicknesses ranging from 0.5 to 3 μm were prepared by spinning a solution of nitrocellulose in amyl acetate onto silicon wafers. The etch rate was determined by measuring the depth of the spot made using a weakly focused ArF excimer laser beam.

The etch rate measurements showed a threshold value for development of approximately 20 mJ/cm². Because there is a threshold, the resist does not obey reciprocity and the contrast is variable. In fact, contrasts in excess of 7 may be obtained under appropriate operating conditions; most conventional photoresists show contrasts of 1 to 3 using lamp exposure. The etch rate increases with fluence, reaching a maximum of $\sim 2 \mu\text{m}\cdot\text{cm}^2/\text{J}$ at 50 mJ/cm².

Figure 2-9 (top) shows a grating pattern in nitrocellulose produced using ArF laser radiation and a 3.8- μm -period grating mask contacted to the substrate; the pattern in Figure 2-9 (bottom) was produced by placing the mask about 40 μm from the substrate. The pattern in Figure 2-9 (bottom) is due to a diffraction phenomenon, called spatial period division,⁹ and serves to illustrate that the resolution of the resist is $\sim 0.3 \mu\text{m}$.

Difficulty can be encountered with contact mask lithography due to the volatile products which form during exposure, causing the mask and the substrate to separate. In order to examine the resolution limits of the resist further, we utilized the diffraction from the edge of a cleaved, 100- μm -thick, Si wafer contacted to a 0.6- μm -thick nitrocellulose film on a Si substrate. Figure 2-10 shows an optical micrograph of the resulting pattern. The grating lines extend to the resolution limit of the microscope. Scanning electron microscope studies of this pattern show incompletely developed line pairs spaced as close as 0.25 μm apart. This spacing is approximately ten times closer than previously reported for an optical

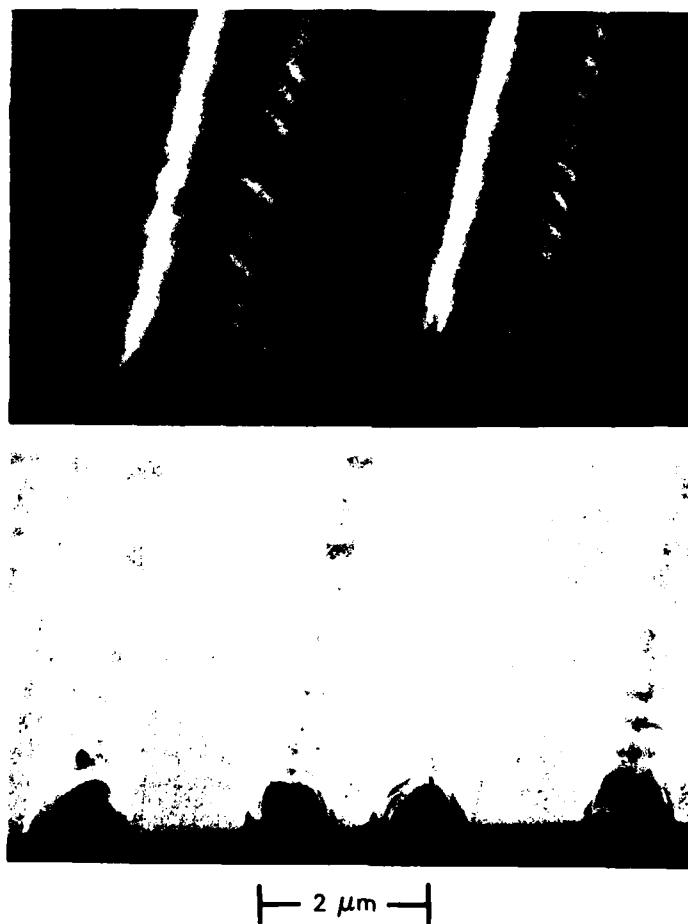


Figure 2-9. (Top) optical micrograph of a grating pattern in nitrocellulose obtained using 193-nm ArF laser radiation and a 3.8- μm -period chrome-on-quartz mask contacted to the Si substrate. (Bottom) grating pattern obtained when the mask is spaced away from the substrate in order to obtain spatial period division effects.

127743 R

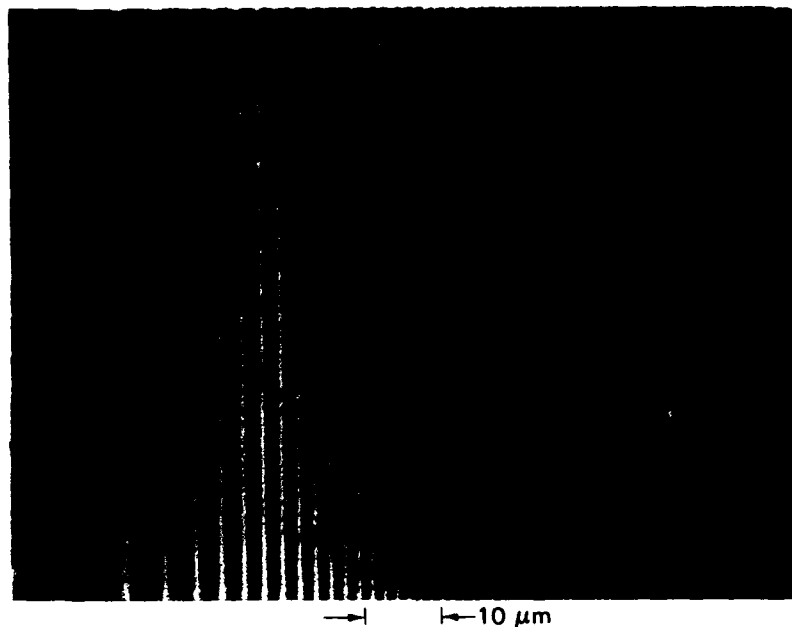


Figure 2-10. Optical micrograph of a grating pattern in nitrocellulose produced by diffraction from the edge of a 100- μ m-thick Si wafer contacted to the substrate.

self-developing resist.⁸ The micrograph also serves to illustrate the high contrast of the resist, since the intensity pattern of diffraction from an edge consists of a relatively weak modulation about an average light intensity rather than the 100-percent modulation that is obtained using a mask pattern. The calculated intensity variation at the edge of the pattern is less than 1 percent of the average intensity.

The stability of nitrocellulose in a number of typical semiconductor processing operations has been described previously.⁷ It is possible to add dopants or additives to alter the processing behavior of nitrocellulose. For example, the addition of 10 wt% ferrocene to the nitrocellulose results in a factor of 4 reduction in the etch rate under typical conditions for reactive-ion etching of SiO_2 (25 Torr CHF_3 at 45 sccm), while leaving the sensitivity to optical radiation unchanged. By contrast, the sensitivity to ion beam exposure was reduced by a factor of 20 by the doping, indicating a difference between the development mechanisms for optical and ion exposure.

T.F. Deutsch
M.W. Geis

REFERENCES

1. Solid State Research Report, Lincoln Laboratory, M.I.T. (1982:3), pp. 15-21, DTIC AD-A124305/4.
2. *Ibid.* (1983:1), pp. 21-23, DTIC AD-A128894.
3. *Ibid.* (1980:3), pp. 11-13, DTIC AD-A094075.
4. *Ibid.* (1982:4), pp. 19-20, DTIC AD-A128982.
5. H.A. Haus, J. Appl. Phys. **51**, 4042 (1980).
6. D.J. Kuizenga and A.E. Siegman, IEEE J. Quantum Electron. **QE-6**, 691 (1970).
7. M.W. Geis, J.N. Randall, T.F. Deutsch, P.D. DeGraff, K.E. Krohn, and L.A. Stern, Appl. Phys. Lett. **43**, 74 (1983).
8. R. Srinivasan and V. Mayne-Banton, Appl. Phys. Lett. **41**, 576 (1982).
9. D.C. Flanders, A.M. Hawryluk, and H.I. Smith, J. Vac. Soc. Technol. **16**, 1949 (1979), DTIC AD-A090071/2.

3. MATERIALS RESEARCH

3.1 ZONE-MELTING RECRYSTALLIZATION OF Si FILMS ON SiO₂-COATED Si SUBSTRATES

In previous reports¹ we have described the preparation of silicon-on-insulator (SOI) films by using graphite strip heaters for zone-melting recrystallization of poly-Si deposited on SiO₂-coated Si substrates. The yield and performance of test devices and circuits fabricated in the recrystallized films are promising.² Work on the zone-melting recrystallization technique has been motivated by the potential of thin-film devices for achieving higher packing density, speed, and radiation resistance than bulk devices, and also by the potential of SOI structures for accomplishing three-dimensional integration of electronic circuits. In this report we describe progress in further development of this technique. Wafer flatness has been improved to a level approaching that required for VLSI applications. The relationships between the density of surface protrusions, the spacing between subgrain boundaries and the temperature gradient at the liquid-solid growth interface have been determined, and the effect of various processing parameters on this gradient has been investigated.

Stringent flatness requirements are imposed by the characteristics of the photolithographic process used in VLSI fabrication. The flatness is measured with a high-angle-of-incidence laser interferometer, which yields an interference pattern that provides a topographic map of the sample surface. The pattern shown in Figure 3-1 was obtained for a typical unrecrystallized 2-in.-dia. SOI wafer placed on a vacuum chuck. The overall warp, peak to valley, is less than 4 μm , a value comparable to that for a bulk Si wafer after device processing. To maintain this degree of flatness for recrystallized samples, well-controlled heating rates and temperature profiles are necessary.

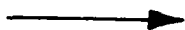


WARP < 4 μm
2 μm /FRINGE

Figure 3-1. Interference pattern showing the flatness of an SOI sample before zone-melting recrystallization.



AS RECRYSTALLIZED
WARP $\sim 28 \mu\text{m}$



BACK SIDE LAPPED
 $< 8 \mu\text{m}$



AFTER ONE HOUR
ANNEAL AT 1000°C
 $< 6 \mu\text{m}$



AFTER AN ADDITIONAL
ONE HOUR ANNEAL AT 1100°C
 $< 6 \mu\text{m}$

SENSITIVITY $2 \mu\text{m}/\text{FRINGE}$

128126-N-01

Figure 3-2. Interference patterns showing the flatness of an SOI sample: (a) as recrystallized; (b) back-side lapped; (c) and (d) after high-temperature anneals.

Uniform thermal contact between the sample and fixed lower heater and a constant separation between the sample and moving upper heater are essential for recrystallization to be accomplished over the entire surface of 2- and 3-in.-dia. samples. Because Si has a lower emissivity than graphite, a radial temperature gradient will result if an SOI sample is placed on an otherwise uniformly heated lower heater. However, it is possible to compensate for this effect, for example, by making a circular depression in the surface of the lower heater in order to reduce the resistive heating directly beneath the sample.

Figure 3-2 shows interference patterns obtained for a recently recrystallized 2-in.-dia. SOI sample that was placed on a vacuum chuck for measurement. The pattern at the upper left shows that the as-recrystallized sample was relatively flat over a large portion of the surface, but had a high point not far from the center. Such high points, which are characteristic of as-recrystallized samples, result from imperfections that protrude from the back side of the wafers and prevent them from conforming to the flat surface of the vacuum chuck. These imperfections can be removed by lapping the back side of the sample. By using this procedure the measured overall warp of the sample was dramatically reduced to less than $8\text{ }\mu\text{m}$, as shown by the interference pattern at the upper right. To simulate the effects of high-temperature device processing, the sample was then annealed for one hour at 1000°C and for another hour at 1100°C . As shown by the two lower patterns, the overall warp was actually decreased to less than $6\text{ }\mu\text{m}$. Similar results have been obtained for 3-in.-dia. wafers, with total warp reduced to less than $8\text{ }\mu\text{m}$. This flatness approaches the level required for VLSI applications.

The recrystallized Si films contain subgrain boundaries (sub-boundaries) and generally exhibit surface protrusions as well. Protrusions are believed to result from the volume expansion occurring during the solidification of liquid Si pools that remain after the liquid-solid interface has passed. Auger profiling studies have shown that the elemental composition of the protrusions is the same as that of the surrounding Si film. The protrusions generally lie along sub-boundaries, suggesting a correlation between the two types of imperfections. By evaluating a large number of SOI samples, we have established a direct relation between protrusion density and sub-boundary spacing. This relationship is illustrated by Figure 3-3, which shows optical micrographs of two recrystallized SOI samples that were Secco etched to delineate the defects. The sample on the right, which has the wider sub-boundary spacing, has many protrusions; the sample on the left, with more closely spaced sub-boundaries, has very few. Figure 3-4, in which the sub-boundary spacing is plotted vs protrusion density, shows a roughly linear relationship between the two quantities.

The model developed earlier to explain sub-boundary formation predicts that a sharper temperature gradient normal to the liquid-solid growth interface will lead to a decrease in sub-boundary spacing.³ Earlier experimental results are consistent with this model, since finer sub-boundary spacing was achieved by reducing the scan speed or the thickness of the Si films, two changes that are expected to increase the interface temperature gradient. With a sharper temperature gradient, the liquid-solid interface becomes more stable and hence less susceptible to small thermal fluctuations that would give rise to protrusions. Since the protrusion density should therefore decrease as the thermal gradient becomes sharper, this density would also be expected to decrease monotonically as the sub-boundary spacing decreases.

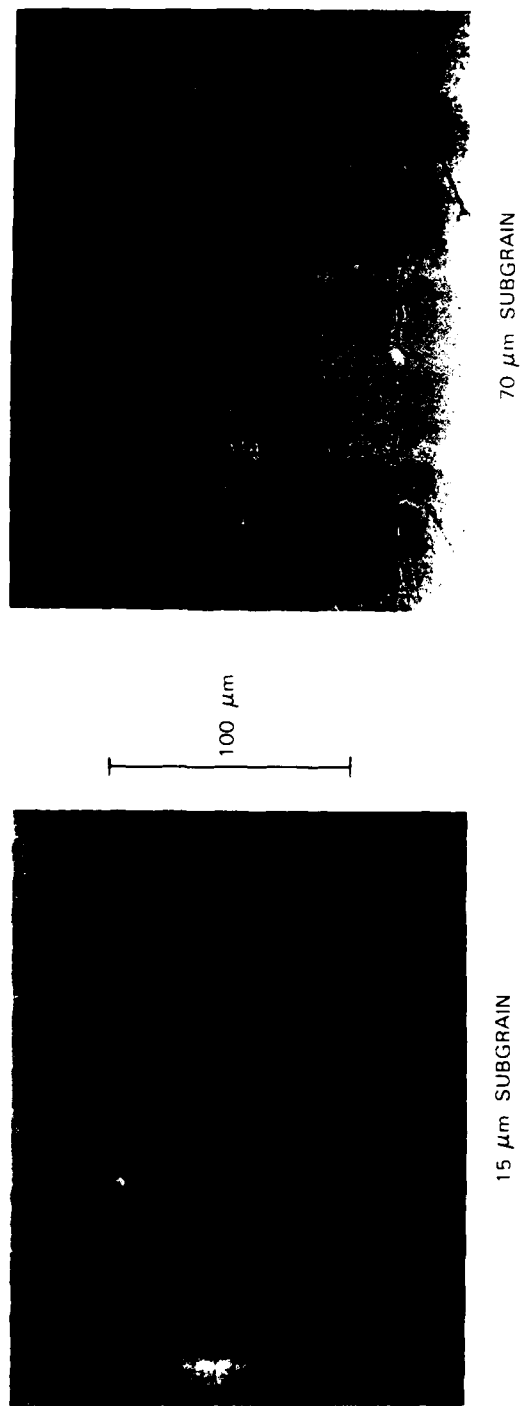


Figure 3-3. Photomicrographs of recrystallized Si films illustrating the correlation between protrusion density and sub-boundary spacing.

128124 N 02

128962 N-01

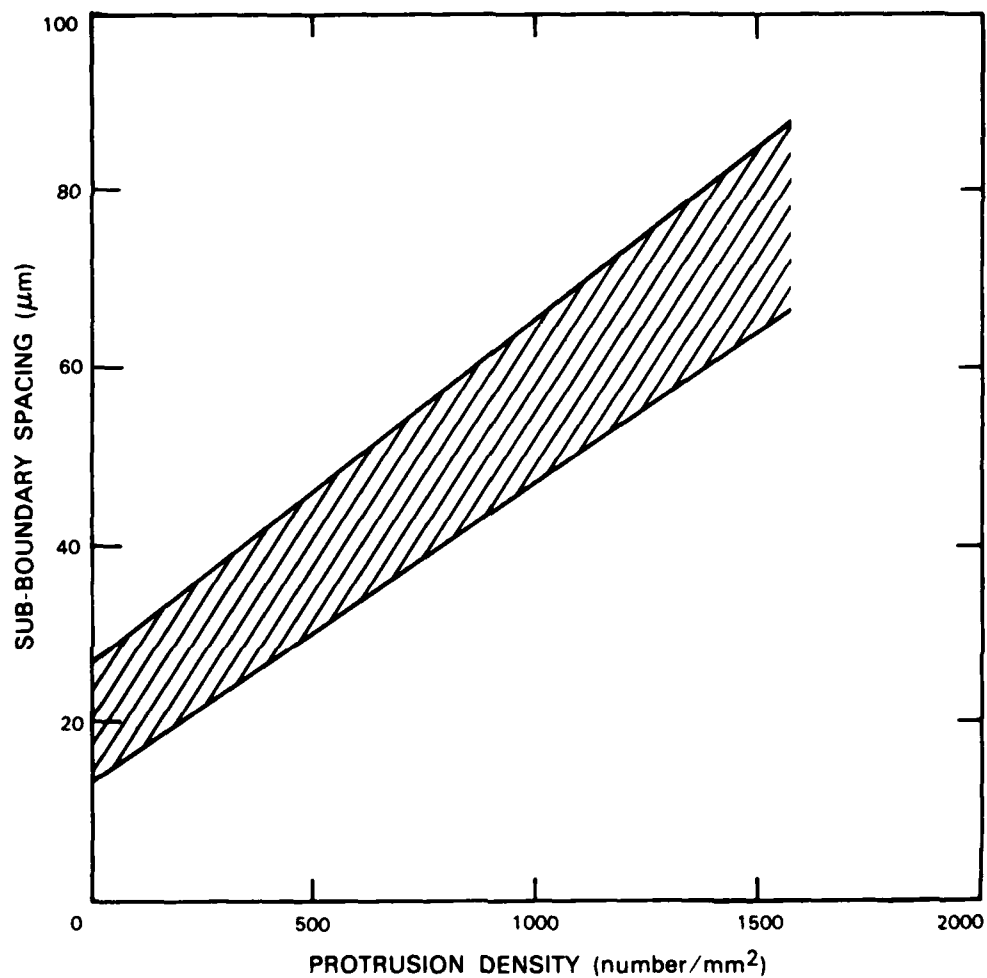


Figure 3-4. Plot of sub-boundary spacing vs protrusion density. Data points for 85 percent of the samples examined fall in the shaded region.

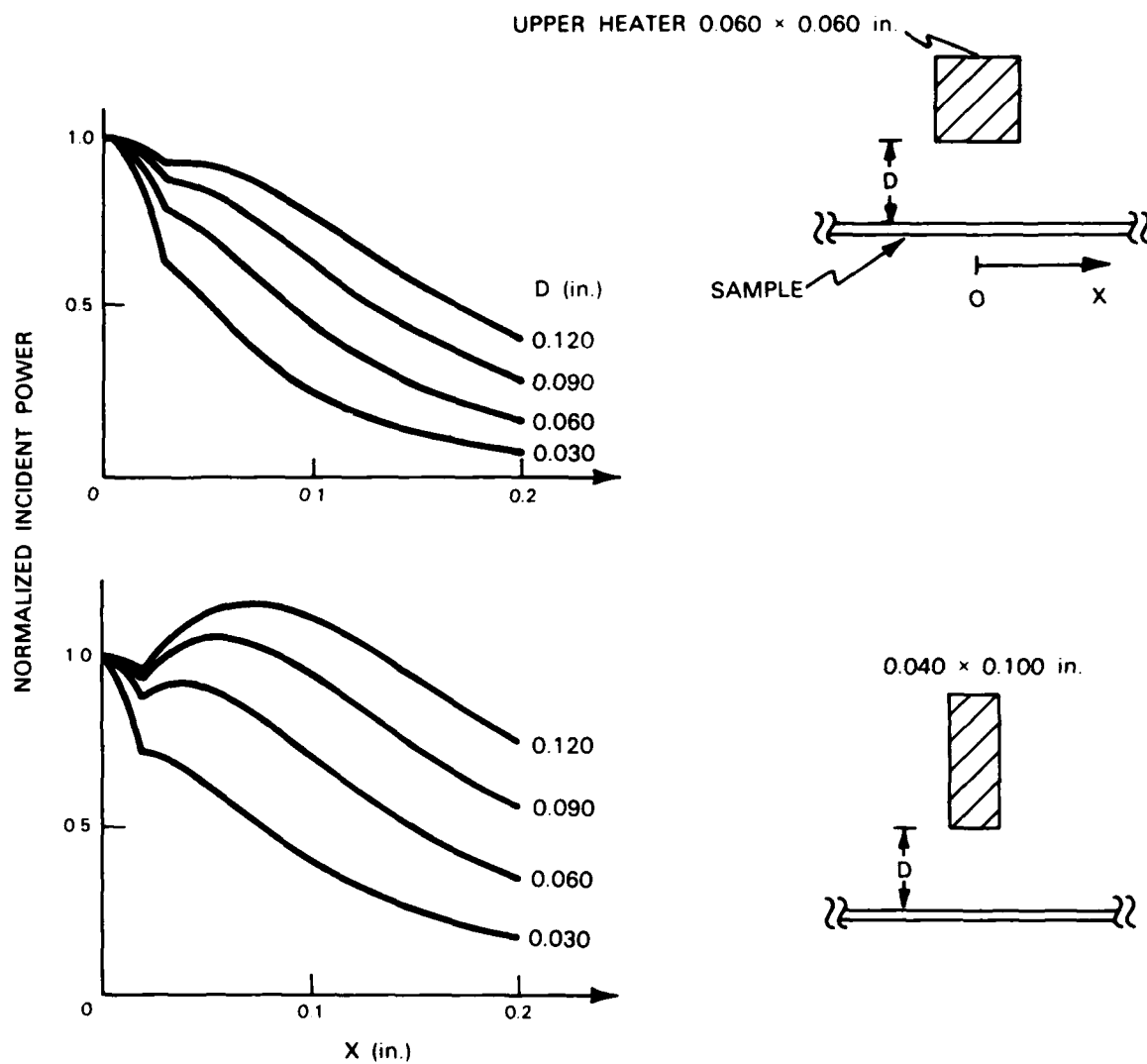


Figure 3-5. Power incident on a sample from the upper strip heater as a function of position X along the sample surface. D is the heater-sample separation.

128122-N-01

We have performed additional experiments confirming the predicted dependence of sub-boundary spacing and protrusion density on the temperature gradient. Several samples that differed in the thickness of the SiO_2 layers below the Si films were recrystallized. Samples with thinner oxide layers, which allow more rapid removal of energy from the molten zone to the substrate and hence should yield sharper temperature gradients, had finer sub-boundary spacing and a lower protrusion density.

The temperature gradient is also affected by the shape of the upper strip heater and the separation between this heater and the sample. We have carried out calculations to investigate the effect of these parameters on the geometrical distribution of the power from the upper heater that is incident on the sample. Figure 3-5 shows curves of power vs distance on the sample surface calculated for two different heater shapes. The power has been normalized at the position $x = 0$, directly beneath the heater. The calculations take into account the angle subtended by the heater at the sample as well as the angle at which the radiant energy is incident on the sample surface. The curves show that the incident power profiles (and thus the temperature gradients) become sharper with decreasing heater-sample separation. Consistent with this result, lower protrusion densities have been observed for reduced separations. The curves also show that much sharper incident power profiles are obtained by reducing the vertical dimension of the heater. For smaller heater-sample separations, this height dependence can be minimized by adjusting the power in order to limit the molten zone to a region directly beneath the upper heater.

C.K. Chen
M.W. Geis
B-Y. Tsaur

R.L. Chapman
J.C.C. Fan

3.2 Pd_2Si /POLY-Si CONTACTS FOR Si DEVICES

Stable, low-resistance ohmic contacts to shallow p-n junctions are an important requirement for small-dimension Si transistors. Although Al is the material predominantly used for wire-bond contacts to these devices, direct Al contacts to shallow junctions are thermally and electrically unstable. Metal silicides are more reliable than Al, but direct silicide contacts to such junctions can jeopardize junction integrity unless the consumption of Si during silicide formation is carefully controlled. In advanced bipolar devices, poly-Si is usually employed for making direct contact to the emitter and base in order to achieve the self-aligned structure and improve device performance.⁴ However, Al/poly-Si contacts would be unsatisfactory, since MOS device studies have shown that such contacts suffer instabilities due to Si precipitation and enhanced electromigration.⁵

We are investigating an alternative metallization scheme that incorporates a metal silicide layer between the Al and poly-Si. As an initial step we have studied the structural and electrical properties of Pd_2Si /poly-Si contacts. We have chosen Pd_2Si , rather than a refractory metal silicide, because the reaction forming this compound from Pd and Si occurs at relatively low temperatures and is not very sensitive to interface contamination. An additional advantage is that dopant atoms in the Si are usually snowplowed in front of the Pd_2Si /Si interface during this reaction,⁶ producing a dopant redistribution that can help preserve

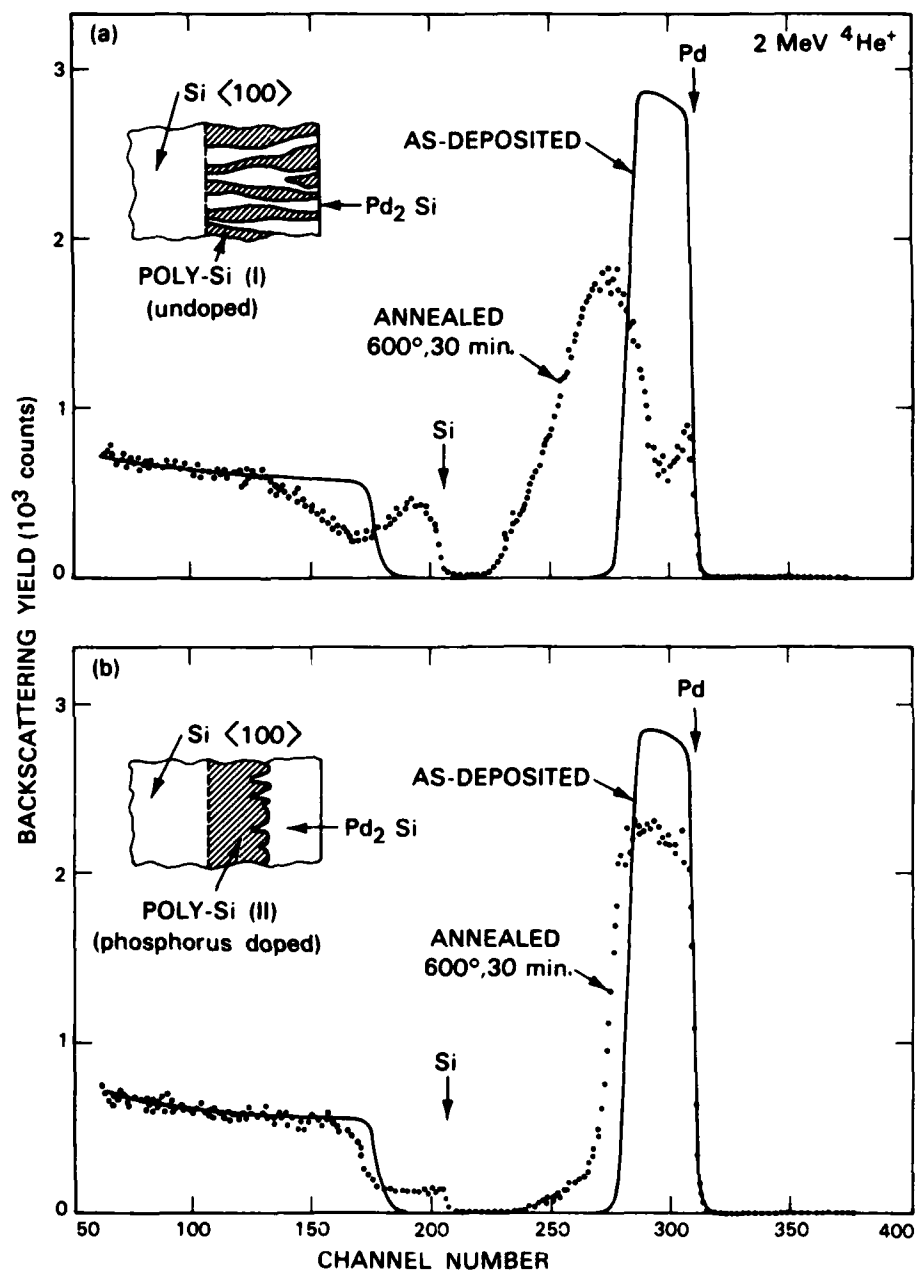


Figure 3-6. RBS spectra showing intermixing of Pd_2Si with (a) undoped poly-Si film and (b) P-doped poly-Si film.

131059 S

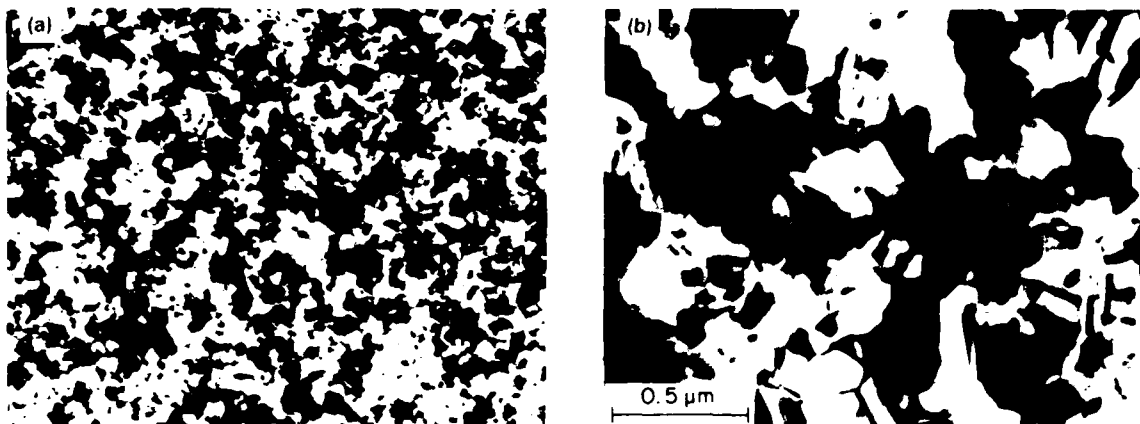


Figure 3-7. TEM micrographs for (a) undoped poly-Si film and (b) doped poly-Si film.

131060 S

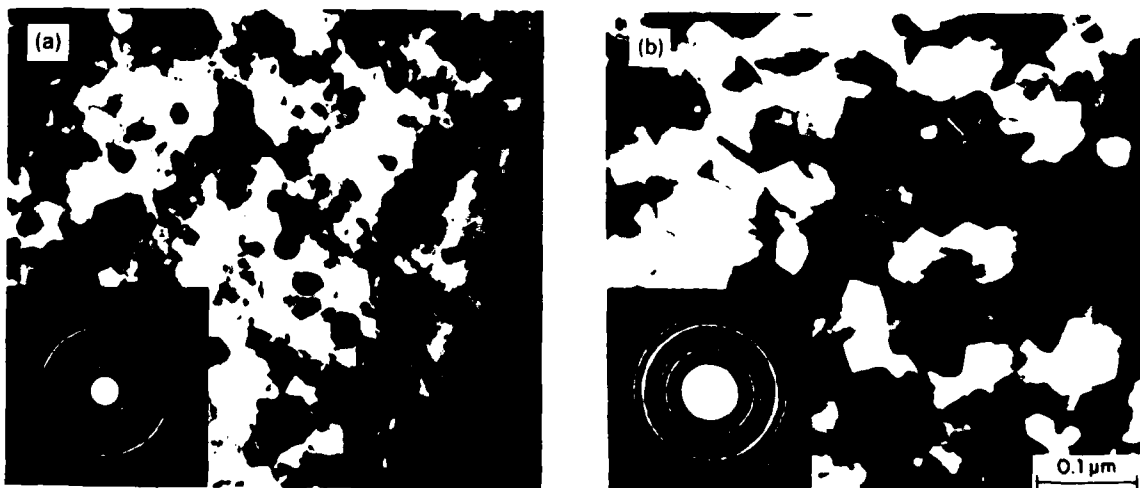


Figure 3-8. TEM micrographs for Pd_2Si formed on (a) undoped poly-Si film and (b) doped poly-Si film.

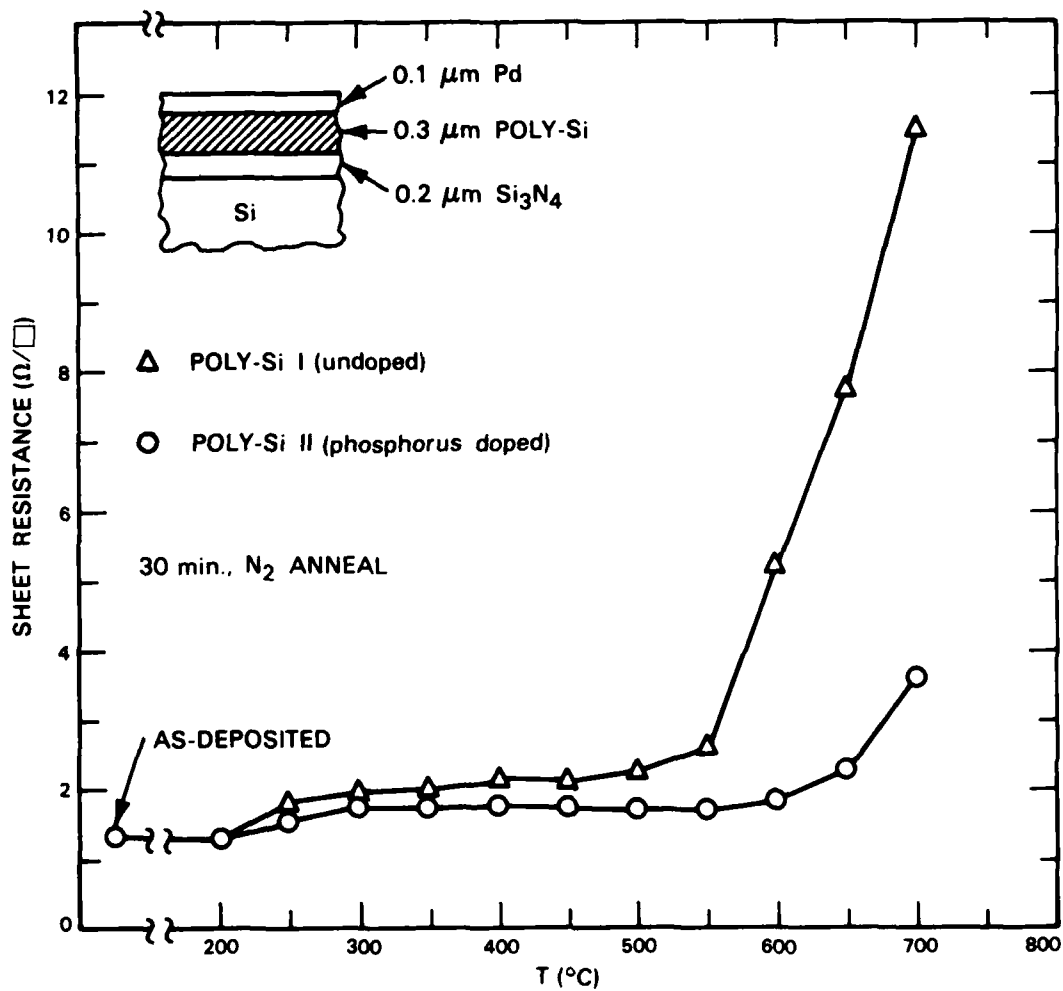


Figure 3-9. Sheet resistance of Pd_2Si /poly-Si layers as a function of annealing temperature.

131081 S

junction integrity and lower contact resistance.⁷ However, Pd₂Si and Al react at relatively low temperatures,⁸ necessitating a diffusion barrier layer between them. We have obtained preliminary results suggesting that W might be a satisfactory barrier material.

Films of Pd 0.1 μm thick were deposited by e-beam evaporation on LPCVD poly-Si films 0.3 μm thick formed on single-crystal Si substrates that were either bare or coated with SiO₂ or Si₃N₄. The poly-Si films were either undoped or doped with P by diffusion at 900° to 1000°C. In a few samples, contact-resistance patterns and junction diodes were prepared for electrical characterization. Thermal treatments at 50°C intervals from 200° to 700°C were performed in flowing N₂ ambient for 30 min. at each temperature.

Rutherford backscattering (RBS) measurements show that Pd₂Si was formed at 250° to 300°C. For the undoped poly-Si films, intermixing with Pd₂Si to produce a two-phase region was first detected after annealing at 550°C; very strong intermixing was observed after annealing at 600°C, with RBS signals due to Pd extending to the depth of the initial poly-Si/substrate interface, as shown in Figure 3-6(a). For doped poly-Si films, on the other hand, intermixing with Pd₂Si was not detected after annealing at 550°C and was still quite limited after annealing at 600°C, as shown by Figure 3-6(b). Transmission electron microscopy (TEM) shows that the grain size is much smaller for the undoped poly-Si films and the Pd₂Si formed on them [Figures 3-7(a) and 3-8(a)] than for the doped poly-Si films and the Pd₂Si formed on them [Figures 3-7(b) and 3-8(b)]. Since intermixing presumably takes place by grain-boundary diffusion, this difference in grain size accounts for the greater stability of the doped poly-Si films. The intermixed poly-Si and Pd₂Si grains have columnar structure.

Figure 3-9 shows the sheet resistance as a function of annealing temperature for Pd/poly-Si samples deposited on Si₃N₄-coated Si substrates. Formation of Pd₂Si at 250° to 300°C results in a small increase in resistance compared to Pd. The data for this temperature range yield a resistivity of $\sim 25 \mu\Omega\text{-cm}$ for Pd₂Si on doped poly-Si; the resistivity is somewhat higher for Pd₂Si formed on undoped poly-Si, probably because of the smaller grain size. The thermal stability is much better for the samples with doped poly-Si than for those with undoped poly-Si, consistent with the smaller degree of Pd₂Si/poly-Si intermixing for the former. The contact resistance between Pd₂Si and doped poly-Si has been determined by transmission line measurements. For films doped to $\sim 2 \times 10^{20} \text{ cm}^{-3}$, for annealing temperatures of 300° to 550°C, the contact resistance is nearly constant at $\sim 5 \times 10^{-7} \Omega \text{ cm}^2$.

Diodes with Pd₂Si/poly-Si or Al/poly-Si contacts to shallow n⁺/p junctions, as shown schematically in Figure 3-10, were fabricated on p-Si substrates. The junctions were formed by P diffusion through the poly-Si film into the substrate. The measured junction depth was $\sim 0.2 \mu\text{m}$. The diode leakage current was measured at a reverse voltage of 10 V. Before annealing, the leakage current density was $\sim 10^{-7} \text{ A/cm}^2$ (see Figure 3-10). The diodes with Al/poly-Si contacts showed a significant increase in leakage current after being annealed at 400°C, while those with Pd₂Si/poly-Si contacts showed no change even after being annealed at 450°C.

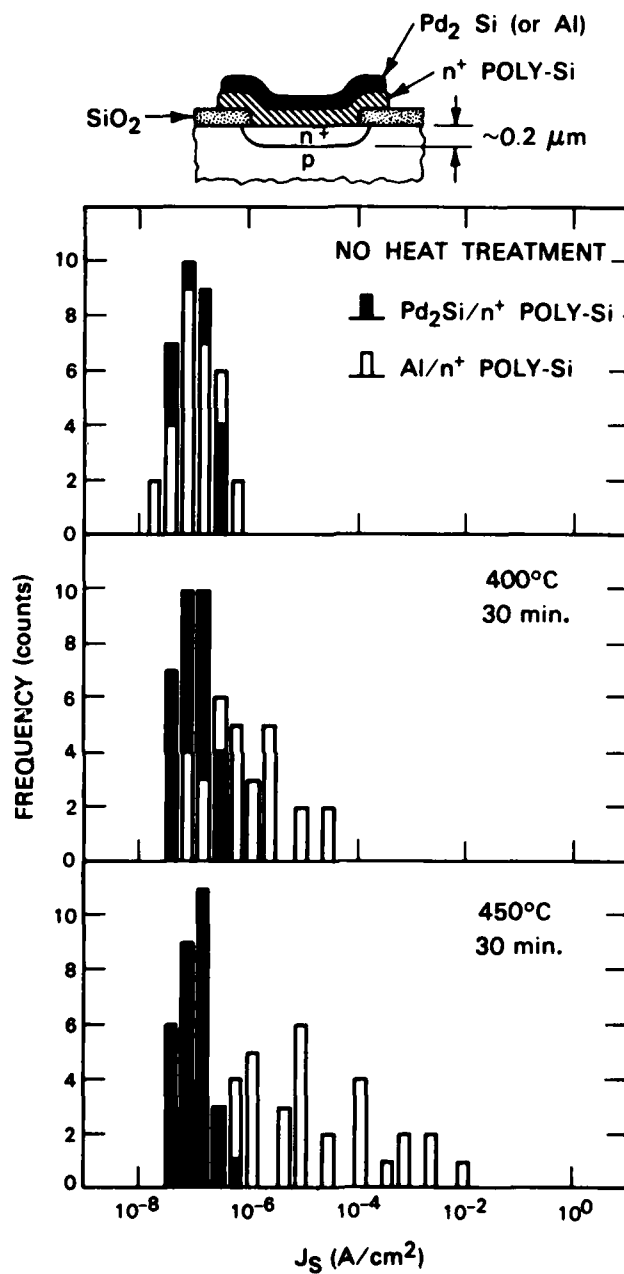


Figure 3-10. Histogram of leakage current density for shallow-junction diodes with $\text{Pd}_2\text{Si}/\text{poly-Si}$ or $\text{Al}/\text{poly-Si}$ contacts.

131064 S

Results suggesting that W may form a satisfactory diffusion barrier between Pd₂Si and Al were obtained in initial annealing experiments on samples prepared by successive deposition of poly-Si, Pd, W (300 Å thick), and Al on SiO₂-coated Si substrates. RBS measurements gave no evidence of reaction after annealing at 400°C for 30 min. and showed only limited reaction between Al and W after annealing at 450°C for the same time.

To further study the effectiveness of W as a diffusion barrier, Schottky diodes with Pd/W/Al metallization were prepared on 1 Ω-cm n-type Si<100> substrates. The diode characteristics of these devices were measured after annealing at 50°C intervals from 300° to 700°C for 30 min. at each temperature. After 300°C annealing the devices exhibited a barrier height of ~0.78 V and an ideality factor of ~1.03, indicating good Schottky characteristics. These characteristics remained nearly unchanged for annealing up to 450°C, but annealing at 500°C caused changes in the barrier height and degradation of the ideality factor. These results indicate that W is an effective diffusion barrier between Pd and Al for 30-min. annealing up to 450°C.

B-Y. Tsaur
C.H. Anderson, Jr.
P.M. Nitishin

3.3 PLASMA-DEPOSITED Si₃N₄ AS AN OXIDATION MASK IN THE FABRICATION OF GaAs SOLAR CELLS

The optimum junction depth in shallow-homojunction n⁺/p/p⁺ GaAs solar cells is approximately 500 Å (Ref. 9). In the fabrication of these cells the technique of anodic oxidation and stripping is utilized for thinning the n⁺ layer from its as-grown thickness, which is generally 1000 to 1500 Å, and the final oxidation step is employed to form an antireflection (AR) coating. High-efficiency cells have been fabricated with either a tin front contact grid applied before anodic oxidation⁹ or a gold front contact grid applied after the final oxidation.¹⁰ However, neither metallization scheme is ideal. In this report we describe a new fabrication technique that employs a plasma-deposited Si₃N₄ mask to permit application of a gold grid before anodic oxidation.

Since a passivating oxide layer is formed on Sn during anodic oxidation, Sn contacts can be electroplated on the n⁺ GaAs surface prior to the oxidation process. This procedure permits the solar cell current and voltage to be monitored after successive oxidation steps, making it convenient to optimize the thickness of the n⁺ layer. However, the bulk electrical conductivity of Sn is only about one-fifth that of Au. Therefore, to obtain comparable series resistance requires the use of thicker Sn layers, which can lead to additional shadowing losses because of the expansion of the contact grid linewidth during electroplating. In addition, there is evidence from scanning electron microscopy that an interfacial oxide layer can be formed between the Sn and GaAs during anodic oxidation. Such a layer can increase the contact resistance and therefore decrease the cell fill factor and conversion efficiency.

Unlike Sn, Au does not become passivated during anodic oxidation. Previously, therefore, it has been necessary to deposit Au contact grids after the completion of the thinning process, making it impossible to monitor the cell characteristics after successive oxidations.

Furthermore, the reduction in the thickness of the n^+ layer separating the contacts from the junction increases the risk that extended high-temperature operation will lead to junction degradation due to the diffusion of Au into the GaAs.

Plasma-deposited Si_3N_4 has been used in MOS technology as a final passivation layer,¹¹ since it provides an inert barrier to Na and H_2O contamination and can be deposited at relatively low temperature. We have found that Au contacts can be protected from dissolution during anodic oxidation by coating them with a film of plasma-deposited Si_3N_4 . The use of this technique makes it possible to take advantage of the higher conductivity of Au while retaining the ability to monitor cell performance after the successive oxidation steps. Plasma-deposited Si_3N_4 has not been used previously in the fabrication of GaAs solar cells.

The basic solar cell structure was prepared by using vapor-phase epitaxy to grow successive p^+ , p , and n^+ GaAs layers on p^+ GaAs substrates, as described previously.¹⁰ The Au contacts were formed by either electroplating or evaporation of Au layers 0.3 to 1.0 μm thick. The protective Si_3N_4 films were deposited at rates of $\sim 160 \text{ \AA}/\text{min}$. in a Plasma-Therm PK1250 multiversion system. The substrate temperatures were in the range of 100° to 200°C . The relative flow rates of N_2 , SiH_4 , and NH_3 were about 30:1.6:1, and the deposition pressure was 0.55 Torr. The RF power density was $0.07 \text{ W}/\text{cm}^2$ at 13.56 MHz.

The Si_3N_4 films were characterized by several techniques. Index of refraction and thickness measurements were made at a number of points on each film with an automatic ellipsometer. The index of refraction was generally found to be 2.00 ± 0.04 , and the thickness uniformity was approximately 5 percent over 2-in.-dia. test wafers. The reproducibility of the films was confirmed by wet etch tests in a solution of 20:1 $\text{H}_2\text{O}:\text{HF}$, which consistently gave etch rates of 1000 to 2000 $\text{\AA}/\text{min}$.

Because the n^+ layer is so thin in shallow-homojunction GaAs solar cells, the quality of the n^+/p junction is very sensitive to damage to the GaAs surface. Any such damage caused by the plasma deposition process or by stress incorporated in the Si_3N_4 film could increase the leakage current significantly, thus degrading the open-circuit voltage and fill factor of the cells. To test the effect of the deposition process, we etched off the anodic oxide layer from a high-efficiency solar cell that had been fabricated by our conventional technique¹⁰ and measured the cell I-V characteristics. A film of Si_3N_4 about 2000 \AA thick was deposited on the n^+ GaAs surface and then removed, after which the I-V characteristics were remeasured. The open-circuit voltage and fill factor of the cell were found to be unchanged. In contrast, deposition and removal of pyrolytic SiO_2 and PSG generally resulted in degradation of these parameters.

We have demonstrated the low intrinsic stress of the plasma-deposited Si_3N_4 films by using an interferometer to examine GaAs and Si wafers before and after deposition of films about 2000 \AA thick. There was no detectable change in the free-standing radius of curvature of the wafers. To evaluate the intrinsic tensile stress, a membrane deflection technique was used for measurements on films deposited on several Si wafers. The average stress was $9 \times 10^8 \text{ dynes}/\text{cm}^2$, well below the values of $\sim 4 \times 10^9 \text{ dynes}/\text{cm}^2$ that were measured by the same technique for Si_3N_4 films deposited by low-pressure chemical vapor deposition.

The optimum thickness of Si_3N_4 to be used for protection masks was determined by experiments on shallow-homojunction solar cells fabricated by the procedure shown in Figure 3-11. An $n^+/p/p^+$ structure was grown by vapor-phase epitaxy, a 3000-Å Au layer was deposited by evaporation on the as-grown GaAs surface and patterned to form a front contact grid, and the entire surface was covered with a layer of Si_3N_4 . Next a photoresist etch mask with sufficient overlap for sidewall coverage was defined over the contact fingers, and the Si_3N_4 between the fingers was removed with a dilute HF etch. The remaining photoresist was removed, an electrical contact was made to the back of the sample, the sample was mounted face up on a glass slide with a low-melting-point wax, and anodic oxidation was performed in the manner described previously.¹⁰ Measurements on solar cells fabricated by this procedure showed that a layer of Si_3N_4 2000 to 3000 Å thick is sufficient to protect the Au fingers during anodic oxidation without producing any detectable degradation in the cell parameters.

The Si_3N_4 masking process was then used in fabricating a number of shallow-homojunction solar cells with anodic oxide AR coatings. The I-V characteristic of the best 0.51-cm² cell is shown in Figure 3-12. The open-circuit voltage is 0.97 V, the short-circuit current is 24.7 mA/cm², and the fill factor is 0.84, giving an AM1 conversion efficiency of 20.1 percent. For a 0.0925-cm², 20-percent AM1 cell fabricated on the same wafer the diode factor is 1.1 and the dark current is 1×10^{-17} A/cm², as determined from the data for short-circuit current density vs open-circuit voltage shown in Figure 3-13, indicating that no junction damage was caused by the plasma-deposition process.

G.W. Turner
M.K. Connors

3.4 DEPTH PROFILE OF TRAPS INTRODUCED BY DRY ETCHING OF GaAs

A number of dry etching techniques have been developed to produce anisotropic etch profiles in GaAs. An important consideration for device and circuit fabrication is whether a sample suffers radiation damage by exposure to ions, electrons, or ultraviolet light during etching. Contamination originating from polymer formation or from materials sputtered from the etching chamber can also influence device performance. In an earlier study,¹² the effects of dry etching on the electrical properties of GaAs were investigated by evaluating the characteristics of Schottky diodes fabricated on the etched surfaces and by using deep-level transient spectroscopy (DLTS) to characterize trapping centers. Etching was found to change the barrier heights and breakdown voltages of the Schottky diodes and to increase the density of electron traps. The DLTS study has now been extended in order to determine the depth profile of the electron traps after dry etching. In addition, the hole traps present in an etched sample have been investigated by means of optical DLTS (ODLTS).

An n-type GaAs sample doped to about 5×10^{16} cm⁻³ was etched to a depth of 300 Å by reactive-ion etching (RIE) in CF_4 at 250 V followed by Ar ion beam etching at 500 V. If a Schottky diode is fabricated directly on the etched surface, the region just below this surface will be shielded from DLTS probing by the intrinsic depletion region

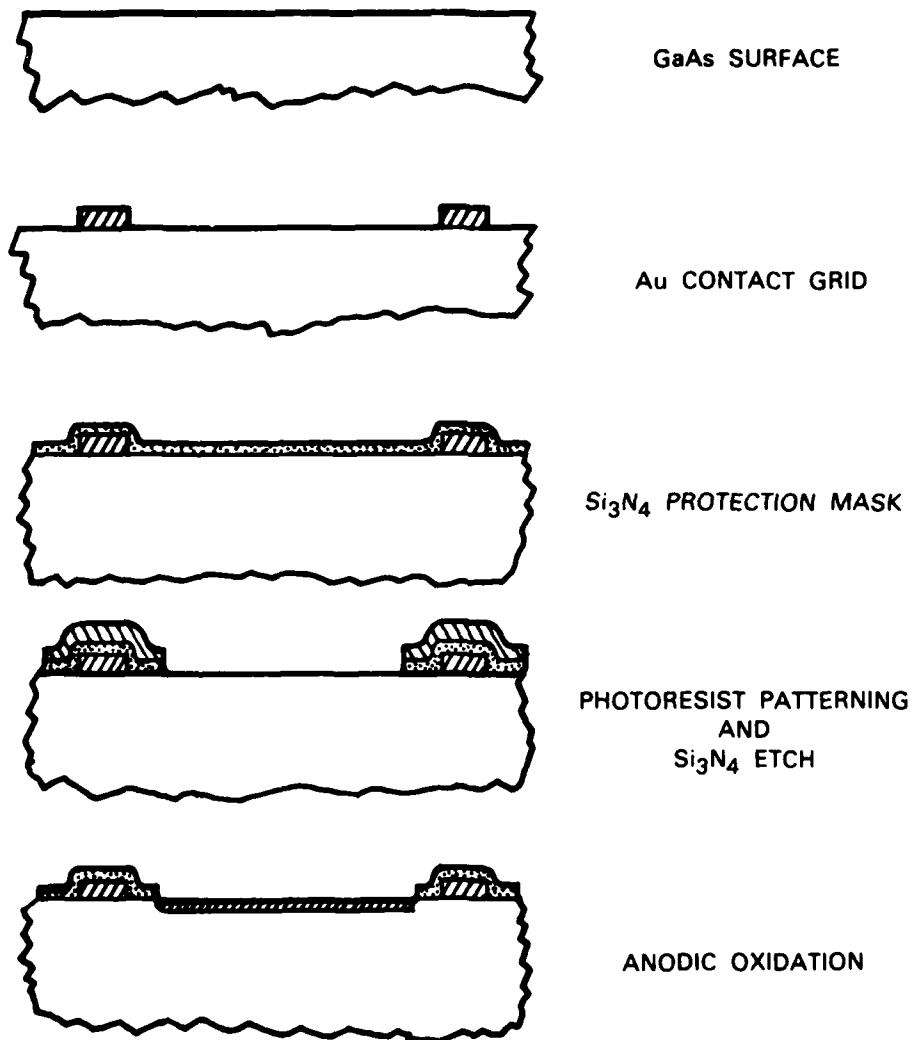


Figure 3-11. Solar cell fabrication procedure using Si_3N_4 protection mask.

128191 N 01

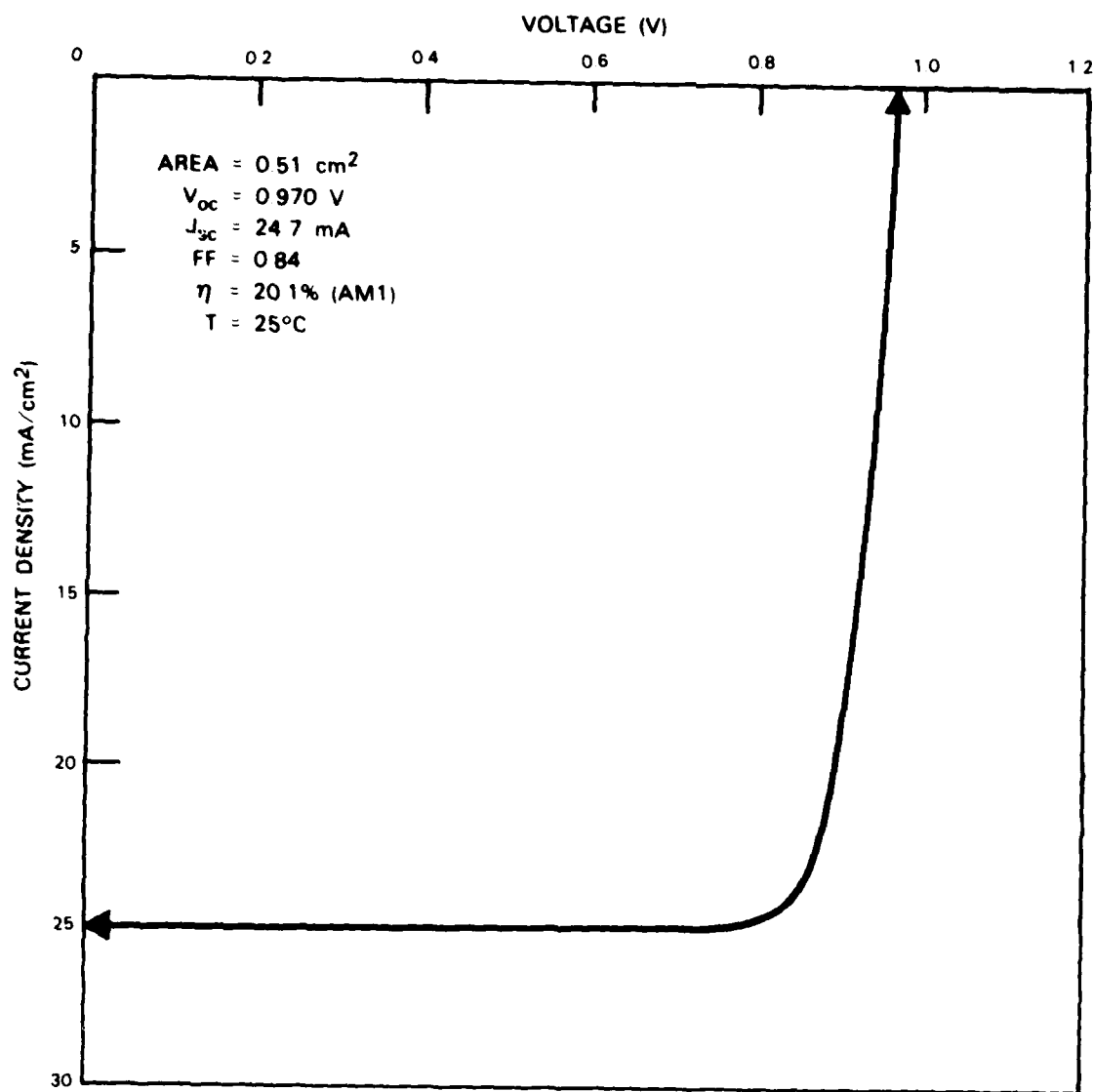


Figure 3-12. Photocurrent density as a function of voltage for GaAs cell with 20-percent conversion efficiency at AM1.

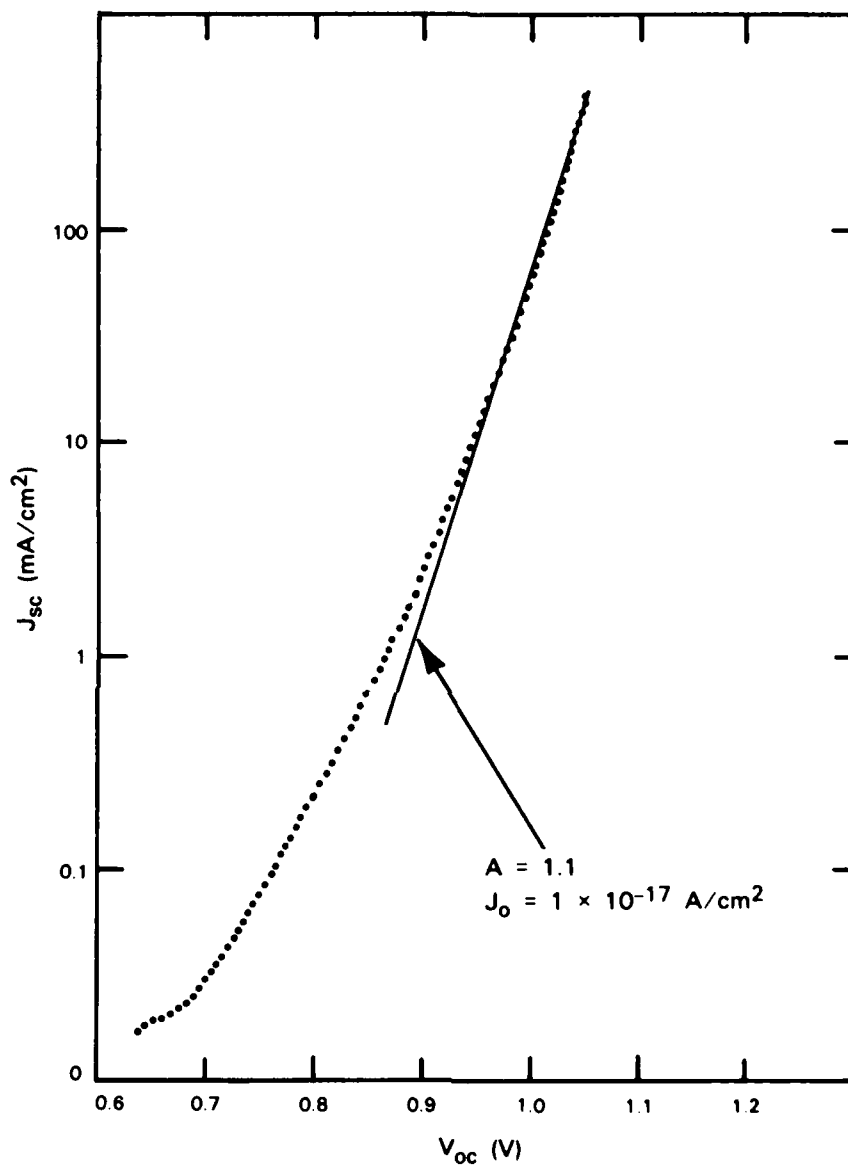


Figure 3-13. Short-circuit current density J_{sc} as a function of open-circuit voltage V_{oc} for a 0.0925-cm^2 cell fabricated on the same wafer as the cell of Figure 3-12.

128190 N 01

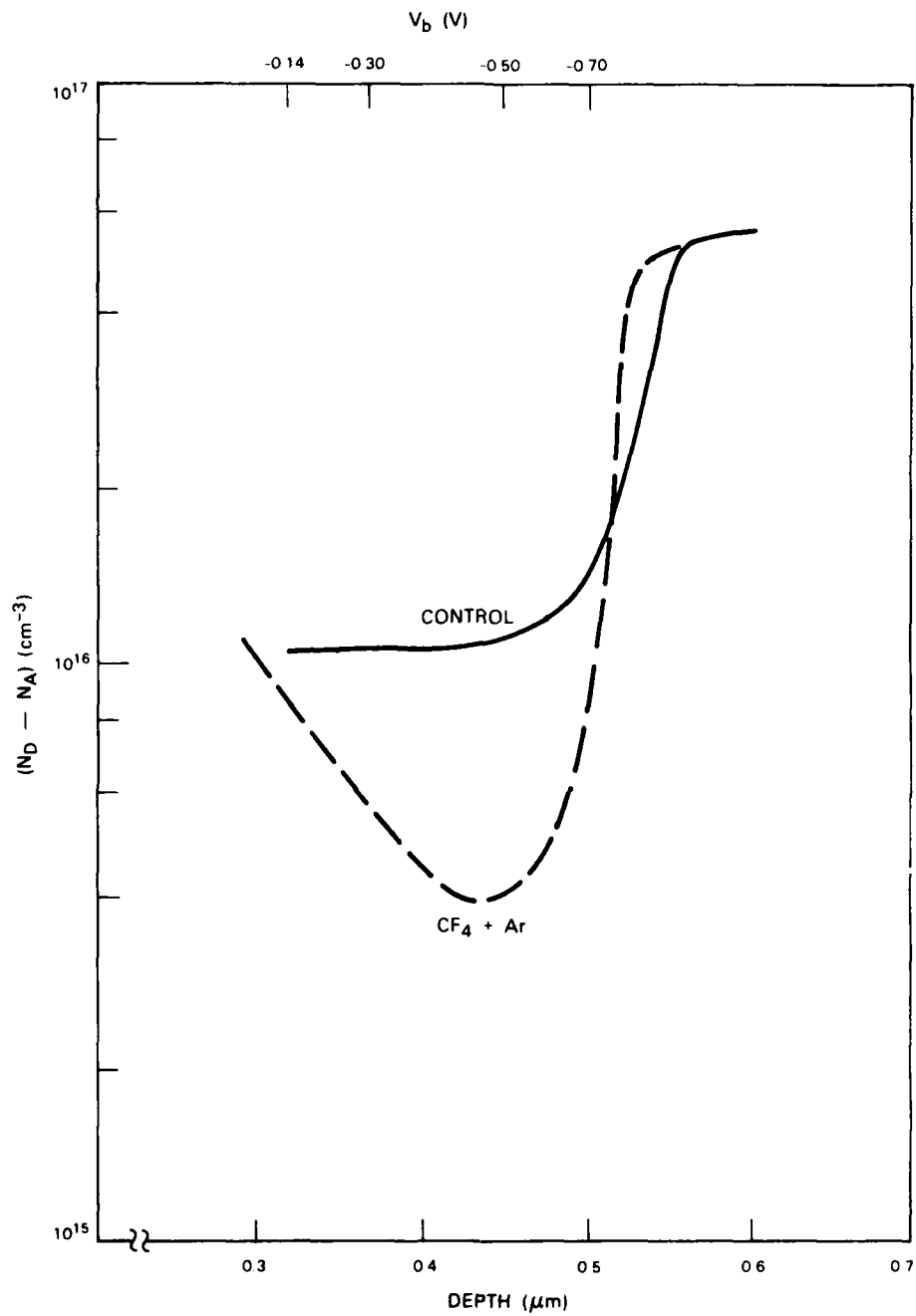
under the metal contact. Therefore, in order to examine the effect of etching, a 0.6- μm -thick n-type GaAs layer doped to about $1 \times 10^{16} \text{ cm}^{-3}$ was grown by vapor phase epitaxy on the etched surface before making the metal contact. Prior to epitaxial growth the surface was cleaned with H_2SO_4 solution, which removed a layer of GaAs about 200 Å thick; during growth the sample was subjected to annealing at the growth temperature of 700°C. The same procedure of H_2SO_4 cleaning, epitaxial growth, and contact metallization was used for a control sample that had not been dry etched.

Figure 3-14 shows the depth profiles of net donor concentration, $N_D - N_A$, obtained by capacitance-voltage measurements on the dry-etched sample and the control sample.¹² At depths from about 0.3 to 0.5 μm below the metal contact, this concentration is significantly lower in the epilayer grown on the dry-etched substrate than in the layer grown on the control substrate. The reduction in concentration, which peaks at a depth of about 0.44 μm , becomes insignificant when the depth reaches 0.6 μm , the location of the epilayer-substrate interface. This behavior indicates that the epitaxial growth process was significantly affected by damage to the substrate surface resulting from dry etching, even though this damage had no appreciable effect on the net donor concentration of the substrate as measured after growth was complete. The mechanism of the effect on the epilayer has not been established. Possibilities include the propagation of lattice damage from the damaged surface into the growing layer and the incorporation of compensating contaminants present on the damaged surface prior to growth.

Earlier DLTS measurements¹² showed the control sample to contain one major electron trap with an energy, E_a , of $\sim 0.89 \text{ eV}$ and a density, N_t , of $\sim 1.3 \times 10^{13} \text{ cm}^{-3}$. Dry etching was found to increase the density of this trap and also to introduce several other electron traps. In the present study, in order to examine the depth distribution of the traps in the dry-etched sample, DLTS measurements were carried out at four different values of DC bias V_b , in each case with a small trap-filling pulse, V_p . Each measurement thus sampled the interval between the depths corresponding to V_b and $(V_b + V_p)$, respectively. The four values of V_b are shown along the upper abscissa of Figure 3-14; the corresponding depths are given by the depth scale of the lower abscissa.

In DLTS measurements N_t is given by $(\Delta C / C) (N_D - N_A)$, where ΔC is the change in capacitance immediately after the filling pulse is removed and C is the static capacitance. It is generally assumed that C is independent of temperature and accordingly that $N_t(T) \sim \Delta C(T)$. In the present case, however, C can vary significantly with temperature, as shown in Figure 3-15. To take account of this variation, the DLTS apparatus was modified by the addition of an analog divider, which yields plots of $\Delta C / C$ vs T .

Figure 3-16 shows the plots of $\Delta C / C$ vs T obtained for the dry-etched sample with the four values of V_b and with $V_p = 0.14 \text{ V}$, which corresponds to a depth interval of 0.05 μm or less. The largest overall trap densities are found for V_b values of 0.30 and -0.50 V, corresponding to the region where the reduction in $(N_D - N_A)$ is greatest, as shown in Figure 3-14. The plots in Figure 3-16 for these V_b values show that the traps associated with the dry-etching process have an almost continuous distribution of energies. For $V_b = -0.70 \text{ V}$ (corresponding to a depth of about 0.5 μm), the trap densities are much smaller, consistent with the results in Figure 3-14.



128137-N-02

Figure 3-14. Depth profiles of net donor concentration deduced from C-V measurements on a control sample (solid line) and a sample etched by reactive-ion etching in CF_4 at 250 V followed by Ar ion beam etching at 500 V (dashed line).

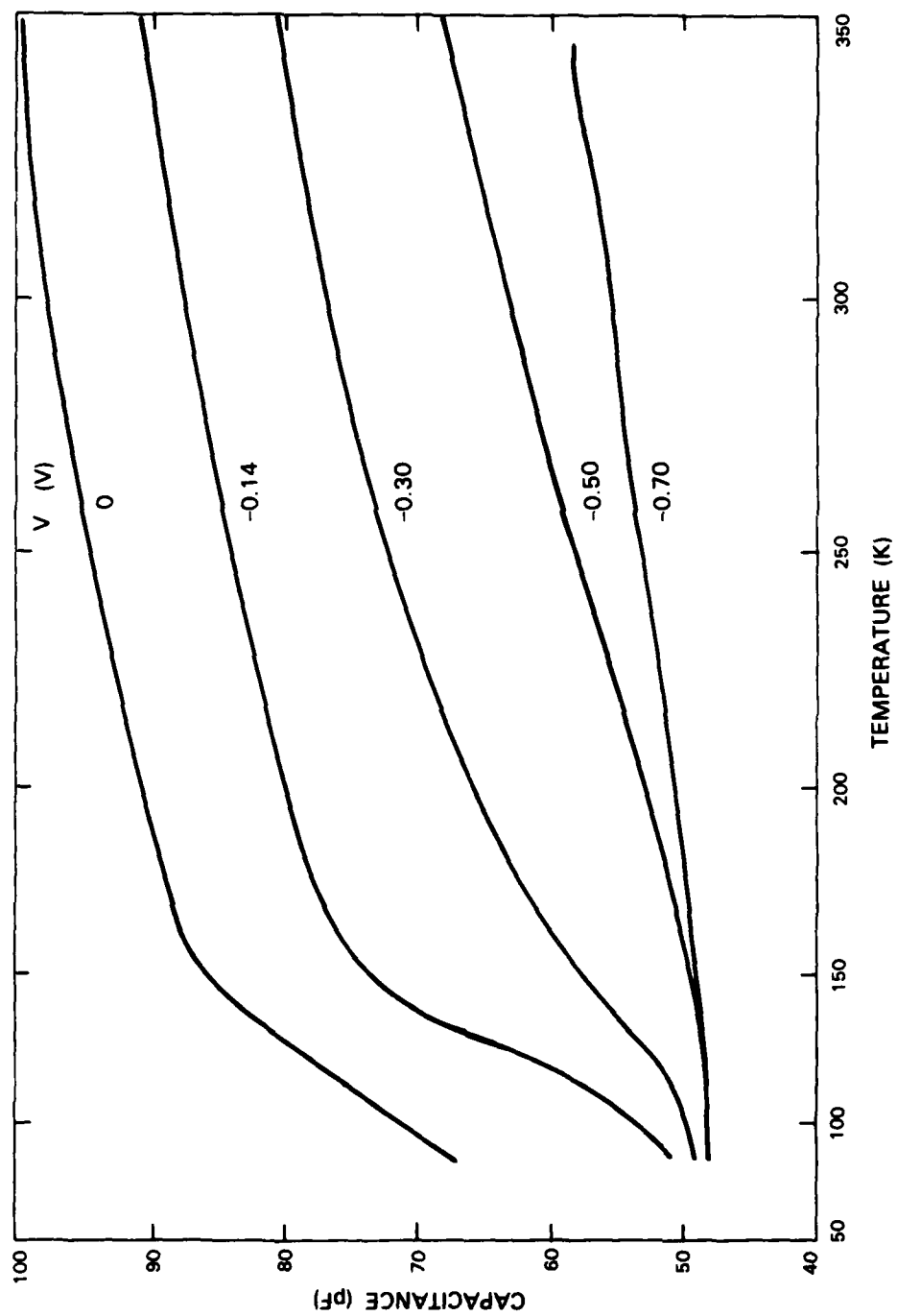


Figure 3-15. Capacitance vs temperature for a back-biased Schottky diode for various values of bias V_b .

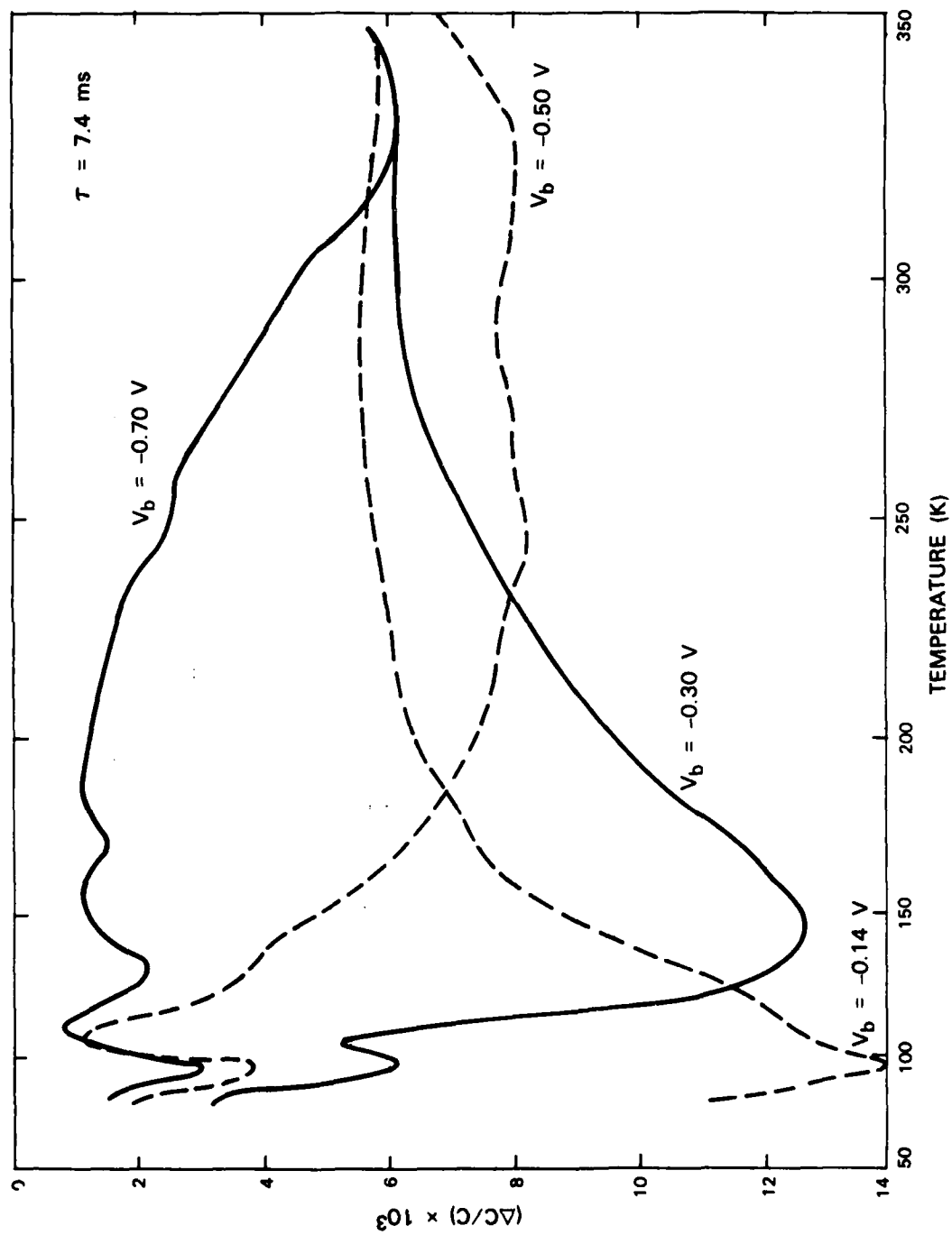


Figure 3-16. DLTS signals $\Delta C/C$ for a 1-ms-wide filling pulse, $V_p = 0.14$ V, and various values of back bias. Emission $\tau = 7.4$ ms.

131083-N

In Figure 3-17 the $\Delta C/C$ vs T plot for $V_b = -0.70$ V and $V_p = 0.14$ V is compared with the plot for $V_b = -0.70$ V and $V_p = 0.70$ V, which measures the total density of electron traps from the surface to about $0.5 \mu\text{m}$. From the latter plot (note that the $\Delta C/C$ values have been multiplied by $1/5$) the total trap density is in the $5 \times 10^{13} \text{ cm}^{-2}$ range, and the traps have a continuous distribution of energies from 0.15 to 0.90 eV.

Since minority carrier traps cannot be observed by DLTS, the hole traps in the dry-etched sample have been investigated by ODLTS. Figure 3-18 shows the $\Delta C/C$ vs T plots obtained for the same values of V_b as those used for the DLTS measurements, together with a plot for $V_b = 0$. These plots indicate that there is a higher concentration of hole traps for V_b values of -0.14 to -0.50 V than for V_b of either 0 or 0.70 V. Thus the excess hole traps are present in the same region of the epilayer that contains additional electron traps resulting from dry etching.

J.G. Mavroides	D.F. Kolesar
S.W. Pang	G.A. Lincoln

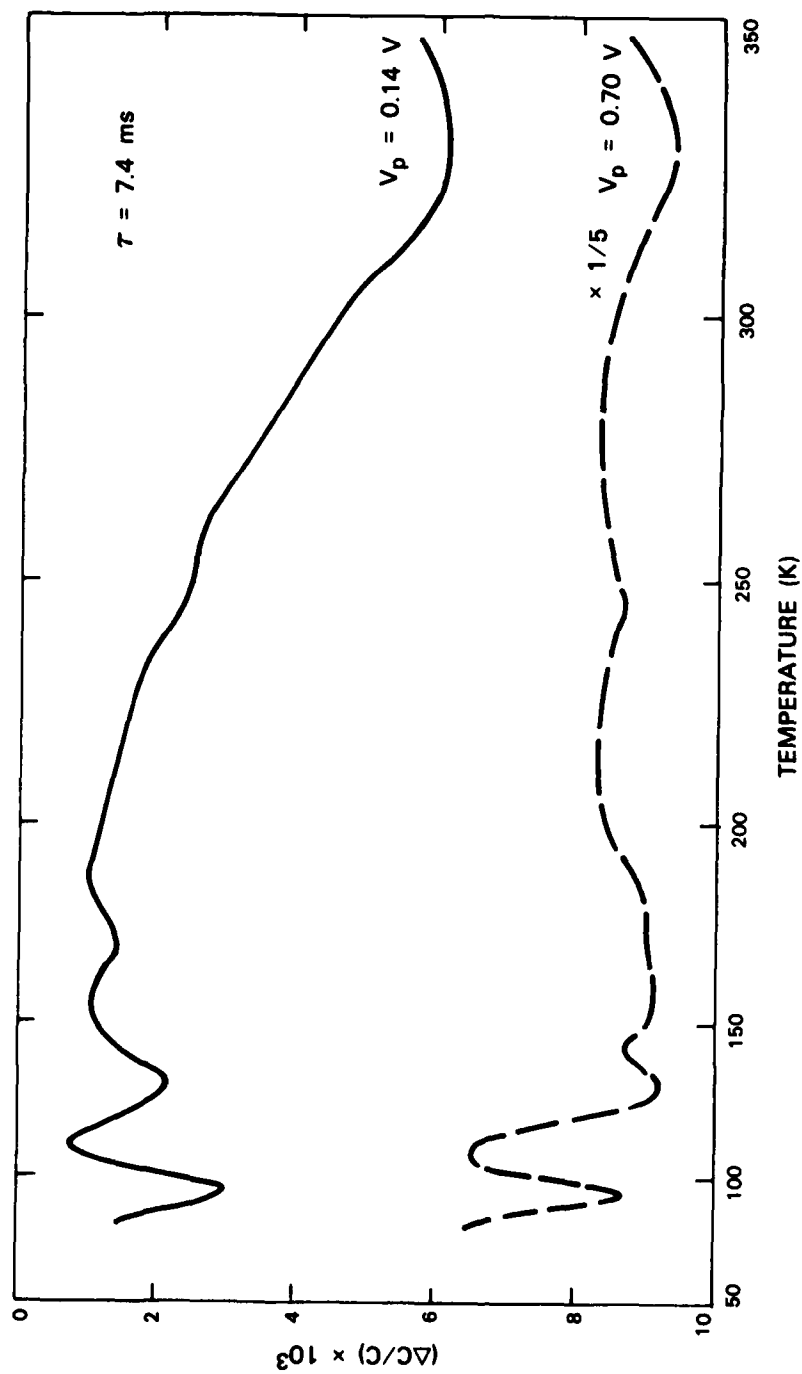


Figure 3-17. DLTS signals $\Delta C/C$ for back bias $V_b = 0.70$ V and 1-ms-wide V_p filling pulses of 0.14 V (solid line) and 0.70 V (dashed line). Emission $\tau = 7.4$ ms.

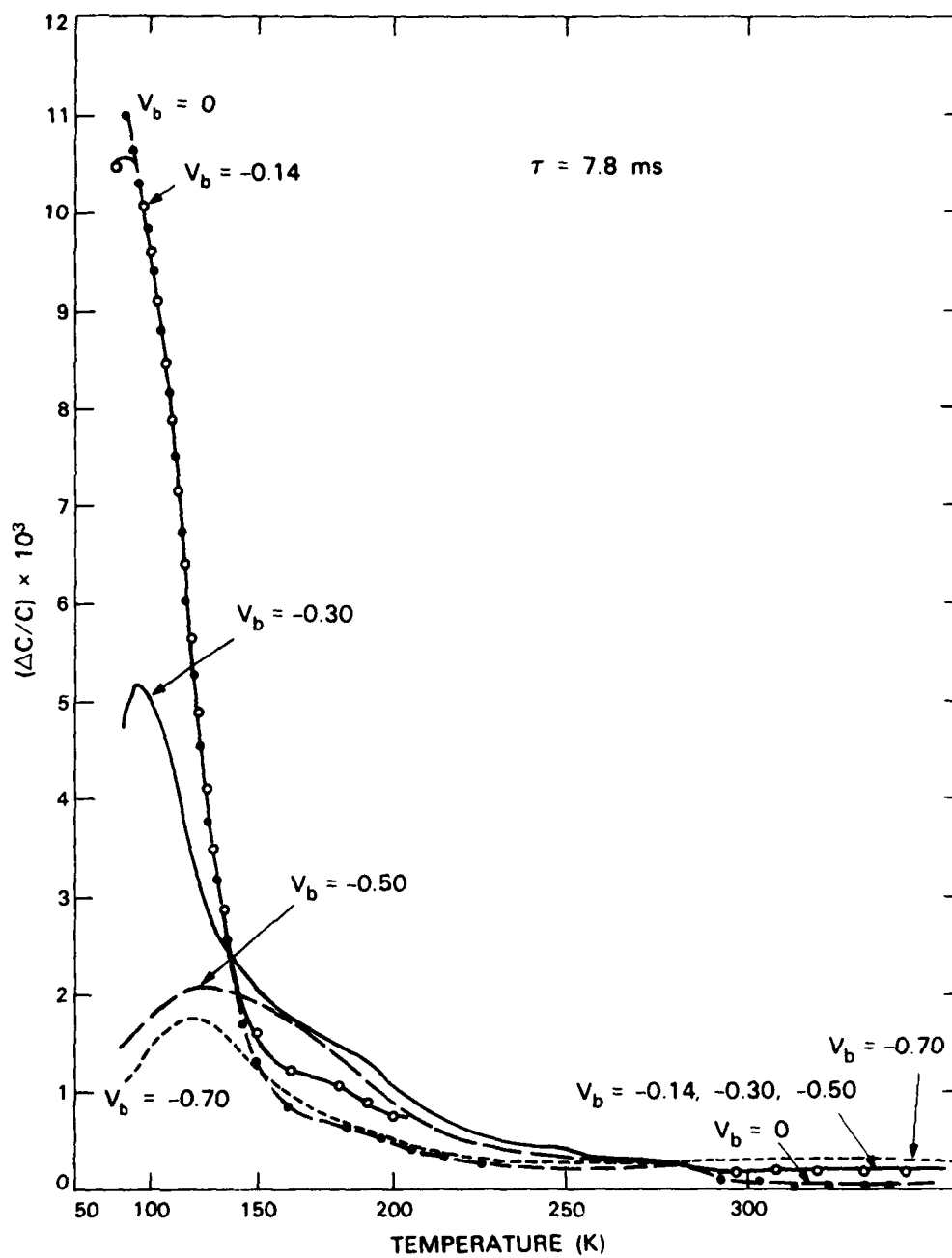


Figure 3-18. ODLTS signals $\Delta C/C$ for $h\nu = 0.95 \mu\text{m}$ and various values of back bias V_b . Emission $\tau = 7.8 \text{ ms}$.

REFERENCES

1. See, for example, Solid State Research Report, Lincoln Laboratory, M.I.T. (1983:2), p. xx; also M.W. Geis, H.I. Smith, B-Y. Tsaur, J.C.C. Fan, D.J. Silversmith, and R.W. Mountain, *J. Electrochem. Soc.* **129**, 2813 (1982).
2. *Ibid.* (1982:2), p. 50, DTIC AD-A122252; also B-Y. Tsaur, J.C.C. Fan, R.L. Chapman, M.W. Geis, D.J. Silversmith, and R.W. Mountain, *IEEE Electron Dev. Lett.* **EDL-3**, 398 (1982).
3. M.W. Geis, H.I. Smith, D.J. Silversmith, and R.W. Mountain, *J. Electrochem. Soc.* **130**, 1178 (1983).
4. See, for example, T.H. Ning, R.D. Isaac, P.M. Solomon, D.D. Tang, H.N. Yu, G.C. Feth, and S.K. Wiedmann, *IEEE Trans. Electron Dev.* **ED-28**, 1010 (1981).
5. S. Vaidya, *Appl. Phys. Lett.* **39**, 900 (1981).
6. M. Wittmer and T.E. Seidel, *J. Appl. Phys.* **49**, 5827 (1978).
7. C.Y. Ting, M. Wittmer, and K.N. Tu, in *VLSI Science and Technology/1982*, C.J. Dell'Oca and W.M. Bullis, Eds. (Electrochemical Society, Pennington, New Jersey, 1982), p. 242.
8. P.S. Ho, J.E. Lewis, and U. Koster, *ibid.*, p. 250.
9. C.O. Bozler, J.C.C. Fan, and R.W. McLelland, in *Proceedings of the 7th International Symposium on GaAs and Related Compounds, St. Louis, 1978* (The Institute of Physics and Physical Society, London, 1979), p. 429.
10. J.C.C. Fan, C.O. Bozler, and R.L. Chapman, *Appl. Phys. Lett.* **32**, 390 (1978), DTIC AD-A058281/7.
11. A.K. Sinha, H.J. Levinstein, T.E. Smith, G. Quintana, and S.E. Haszko, *J. Electrochem. Soc.* **125**, 601 (1978).
12. S.K. Pang, G.A. Lincoln, R.W. McClelland, P.D. DeGraff, M.W. Geis, and W.J. Piacentini, "Effects of Dry Etching on GaAs," submitted to *J. Vac. Sci. Technol.*

4. MICROELECTRONICS

4.1 A TECHNIQUE FOR THE DETERMINATION OF STRESS IN THIN FILMS

Intrinsic stress, elastic bulk modulus, and yield strength of thin films have been determined by measuring the deformation vs pressure of circular membranes of the materials. Experimental data for low-pressure chemical vapor deposited (LPCVD) silicon-rich silicon nitride (SiN_x) is given. It is shown that the stress measurement technique can be extended to accurately measure the intrinsic stress of thin films deposited onto SiN_x membranes.

By using a technique similar to that suggested by Beams,¹ stress measurements are carried out by applying a known pressure differential between the front and back of a circular membrane, as illustrated in Figure 4-1. The differential pressure p , as a function of membrane deflection, is found to be

$$p = \frac{4t\sigma_0}{r^2} h + \frac{8t}{3r^4} \frac{E}{1-\nu} h^3 \quad (4-1)$$

for a membrane with radius r , bulge height h , film thickness t , intrinsic stress σ_0 , and bulk modulus $E/(1-\nu)$ (References 1 and 2). By interferometrically measuring the bulge height vs pressure, fitting the data to a polynomial with first- and third-order terms and using the known membrane thickness and radius, σ_0 and $E/(1-\nu)$ can be determined easily.

A method similar to that of Sekimoto *et al.*³ is used for fabrication of a free-standing membrane. A silicon wafer is coated with 1- μm , silicon-rich, silicon nitride (SiN_x) prepared by reaction of SiH_2Cl_2 and NH_3 (5:1 by volume) at 850°C by LPCVD. A circular window pattern is opened in the SiN_x on the wafer back side by conventional photolithography and CF_4/O_2 plasma etching. The silicon is then etched away using a KOH anisotropic etchant.

Figure 4-2 shows the center deflection vs pressure data for a 1- μm -thick SiN_x circular membrane of 1.05 cm diameter. LPCVD material fabricated in this manner is well suited as free-standing mask material since it is optically transparent, has a thermal expansion coefficient well matched with that of the original Si support material, and has a resulting membrane stress sufficient to assure minimal distortion due to heating during X-ray or ion-beam exposure.^{4,5} A yield pressure of 470 Torr was found for 1-cm-dia., 1- μm -thick material. The high yield pressure indicates that this material can be used as an X-ray-transparent vacuum window in an exposure apparatus in which there is a pressure differential between the X-ray source and the substrate exposure chambers.

By using LPCVD SiN_x membranes, extension of the bulge-measurement technique can be made to thin films of other materials. Stress determination using this technique is possible for deposited thin films in compressive stress as long as the total stress in the composite membrane is tensile. First the intrinsic stress of the SiN_x membrane is determined. Then another thin film is deposited onto the membrane, and the properties of the thin film composite are measured. Experimental data for several thin films in tensile stress deposited onto SiN_x membranes are listed in Table 4-1. Agreement is good between measurements made using bulged membranes and those made using the bending of wafers. Both membrane bulge

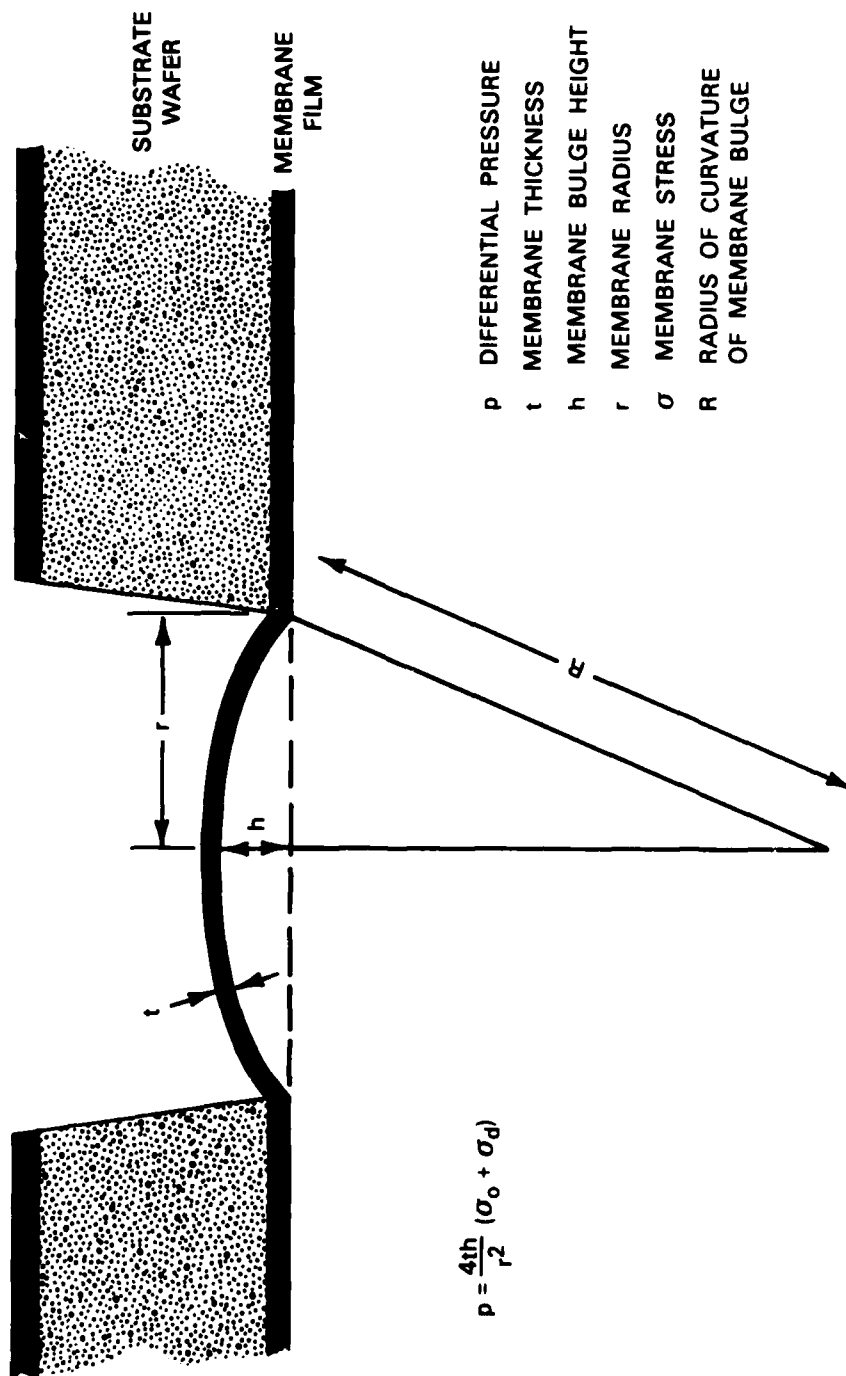


Figure 4-1. Diagram of the deflection of a free-standing membrane used for stress calculation.

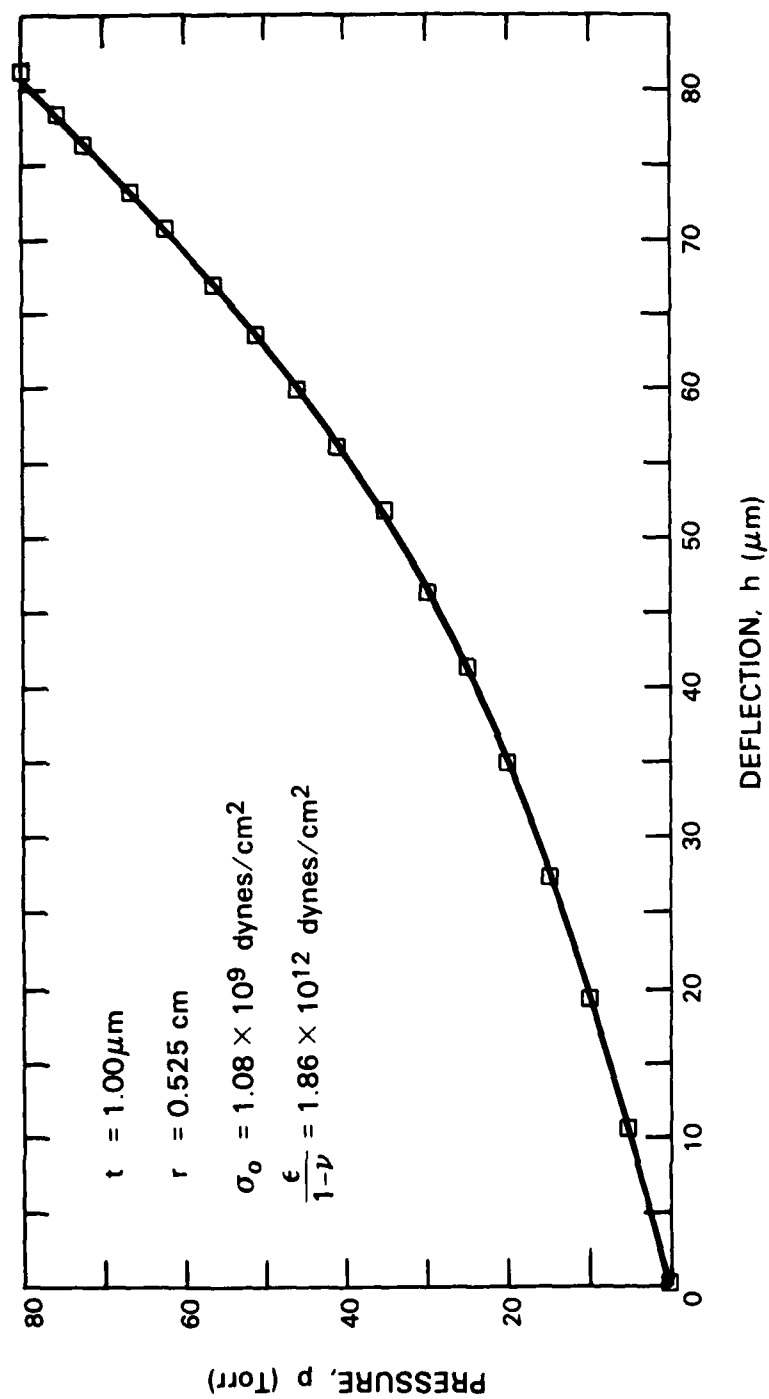


Figure 4-2. Bulge test data and fit for LPCVD SiN_x deposited at 850°C with a gas volume ratio of 5:1 ($\text{SiH}_2\text{Cl}_2:\text{NH}_3$).

and wafer bending techniques have a stress measurement accuracy of ~ 1 percent. However, the bulge technique can be used to measure stresses $< 1 \times 10^2$ dynes/cm², which is five orders of magnitude lower than is possible with the bending technique.

E.I. Bromley D.C. Flanders
J.N. Randall R.W. Mountain

TABLE 4-1 EXPERIMENTAL DATA FOR SEVERAL THIN FILMS DEPOSITED ONTO SiN _x MEMBRANES		
Thin Film Material	t (Å)	σ_0 (dynes/cm ²)
Sputtered W	400	8.8×10^{10}
Evaporated Al	370	6.8×10^{10}
Evaporated Ni	740	2.8×10^{10}
Evaporated Cr	615	1.4×10^{10}
Evaporated Mo	1000	4.3×10^9
Evaporated Au	480	2.3×10^9

4.2 CHARGE-COUPLED DEVICES: TIME-INTEGRATING CORRELATOR

In previous reports⁶⁻⁸ we have described the design and some initial test results for a new binary-analog time-integrating correlator which uses a pipe-organ CCD structure. This device is intended for use in spread-spectrum receivers, and in particular with the 10.23-Mb/s P-code of the Global Positioning System (GPS). In this report we describe the charge integrator and a technique for managing the buildup of integrated charge. We also describe test results which demonstrate device operation at a 20-MHz clock rate (as required for the GPS application) and removal of the fixed pattern noise previously noted⁸ with a simple post-processing technique.

One limitation on the integration time or processing gain of this correlator is the large buildup of integrated charge. Long integration times are desirable but can require an unrealistically large portion of the chip area for the integrating capacitor and output register. An analysis has shown that for the input signal-to-noise ratios which are typical of spread-spectrum applications, the integrated charge consists of a relatively small signal charge riding

on a DC background. One way to deal with this large DC background charge is to skim off only the signal-bearing portion of the charge into the output register and discard the background charge. The charge handling requirements of the output register (and therefore its area) are then reduced by the ratio of the skimmed to total integrated charge.

An integrator circuit which employs a charge skimming feature is described in Figure 4-3. Charge from the high-speed delay lines passes through the reference multiplier gates (labeled V_R , V_R) and is collected by an FET whose gate is labeled INTEGRATE. During most of the integration period this gate is high and the charge is collected on the drain [Figure 4-3(b)]. At the end of the integration period this gate is driven low, and the top portion of the charge is skimmed off over a skim gate into a temporary holding well [Figure 4-3(c)]. This skimmed charge, containing the signal, is then delivered to the output register. Meanwhile the DC background charge is drained off through a reset transistor before the next integration period. Because of spatial variations in threshold voltage between the skim and reset gates, we expect variations in skimmed charge and therefore spatial pattern noise due to this circuit. However, experimental results show that the pattern noise introduced by skimming is much less than that arising from the CCD input stages.

The performance of the integrator and skimming circuits and of the device as a whole has been demonstrated previously at a 5-MHz clock rate.⁸ The clock drivers used in those tests were commercial TTL-MOS translators which were not capable of driving the large (500-pF) capacitance of the pipe-organ gates at clock frequencies above 5 MHz. However, we have recently built a clock driver which is capable of driving the correlator at a 20-MHz clock frequency. In Figure 4-4 we show an example of device performance at 20 MHz using a 511-bit m-sequence at 20 Mb/s as the input signal (upper trace) and the same sequence delayed by 16 bits as the reference. The integration period is 511 clock periods or 25.6 μ s, and the output data rate (lower trace) is 1.4 MHz. The existence of both positive and negative correlation peaks is due to the fact that the reference sequence was modulated by +1 and -1 during alternate integration periods. In this test the skimming gate was adjusted to allow the top 10 percent of the integrated charge to be skimmed off.

The ideal correlation function for this sequence has flat sidelobes, and the nonuniform sidelobes seen in Figure 4-4 are an artifact of the device and due primarily to variations in the charge generated among the CCD input stages. This pattern noise is stationary and independent of both signal and reference, and therefore can be removed by post-processing. A simple and highly effective method of removing pattern noise has been demonstrated with a SAW/CCD time-integrating correlator⁹ and is illustrated in Figure 4-5. The local reference is modulated by a +1, -1, +1, ... sequence during each integration period causing the correlation peak to change sign without affecting the pattern noise, as was demonstrated in Figure 4-4. We remove this modulation by multiplying the CCD output by the same ± 1 sequence, and then sum two (or any even number) of data sets. This demodulation restores the correlation peaks to their correct polarity, but the pattern noise reverses sign and is canceled when the data frames are summed.

The noise cancellation scheme of Figure 4-5 is demonstrated in Figure 4-6. The input signal is a 1023-bit m-sequence at 20 Mb/s, and the CCD output after two successive integration periods (each 512 clock periods) is shown in the upper trace. This signal was then

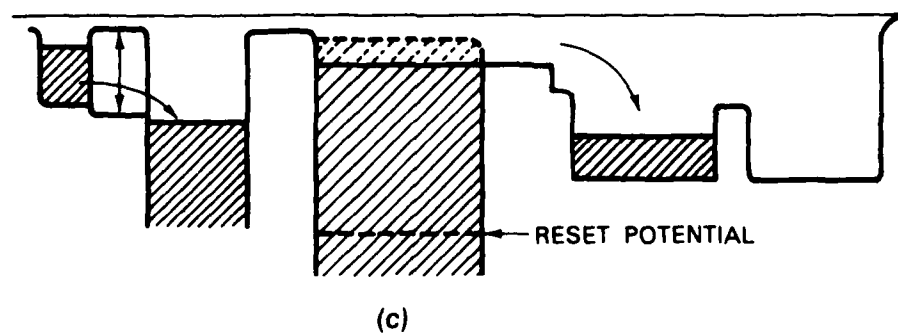
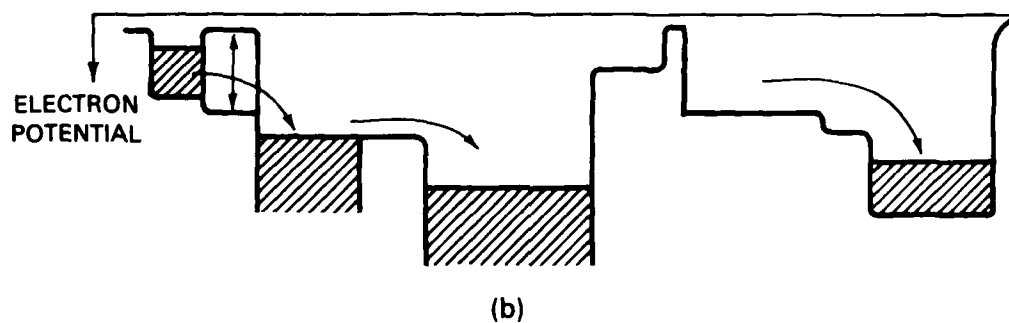
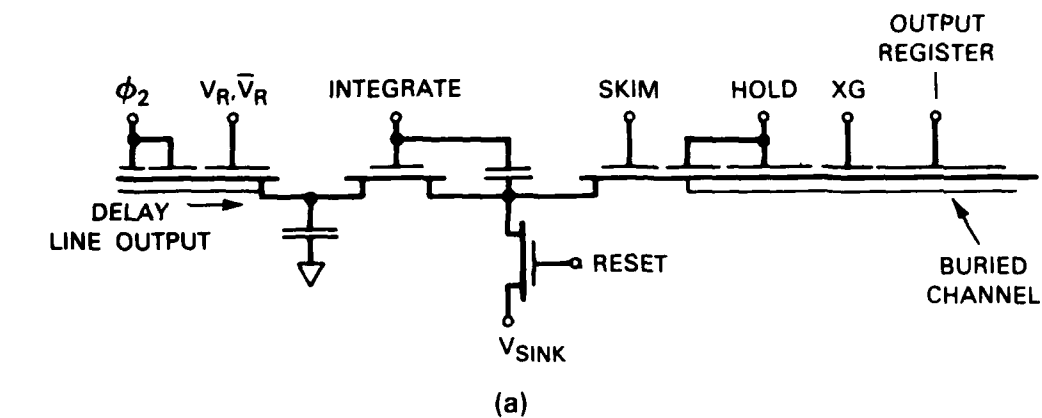


Figure 4-3. (a) Diagram of the integrator and skimming circuits, (b) potential diagram when integrator gate is high and holding gate is low, and (c) when integrator gate is low, holding gate is high, and charge skimming occurs.

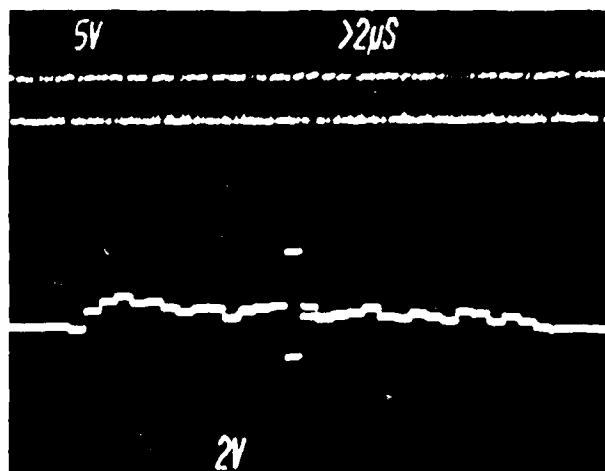


Figure 4-4. Example of correlator performance at a 20-MHz clock rate. Upper trace is a 511-bit m-sequence at 20 Mb/s and the lower trace is the CCD output at 1.4 MHz after integrating for 511 clock periods (25.6 μ s).

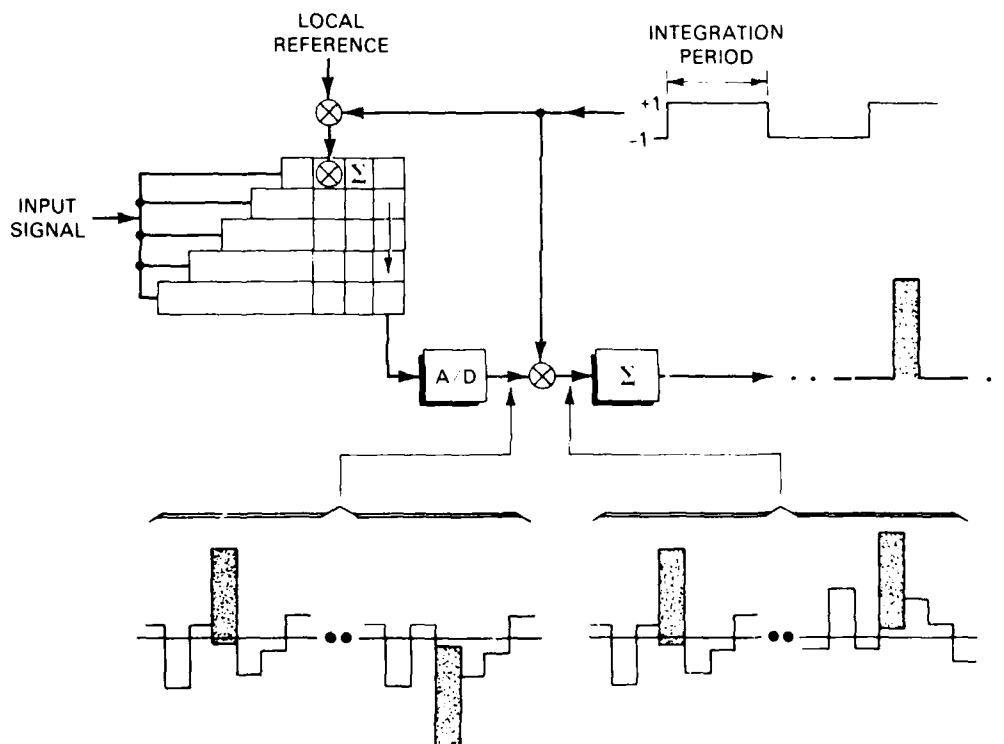
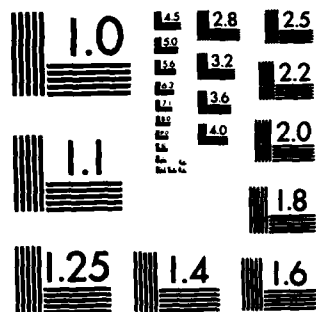


Figure 4-5. Illustration of a method of removing pattern noise arising from offsets

SOLID STATE RESEARCH(U) MASSACHUSETTS INST OF TECH
LEXINGTON LINCOLN LAB A L MCWHORTER 15 AUG 83 1983:3
ESD-TR-83-051 F19628-80-C-0002

F/G 20/12 NL

END
DATE
FILMED
5 84
DTIC



MICROCOPY RESOLUTION TEST CHART
NATIONAL BUREAU OF STANDARDS-1963-A

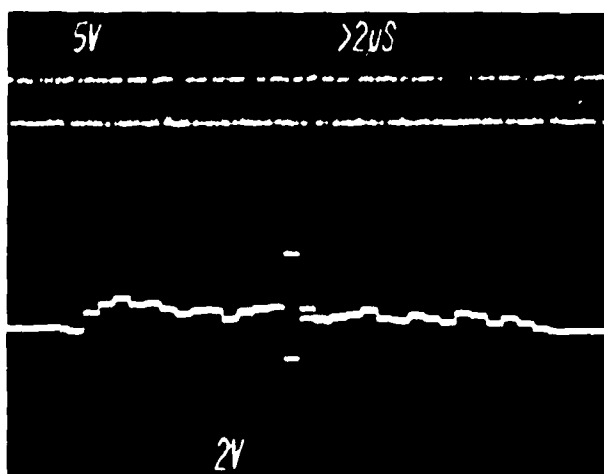


Figure 4-4. Example of correlator performance at a 20-MHz clock rate. Upper trace is a 511-bit m-sequence at 20 Mb/s and the lower trace is the CCD output at 1.4 MHz after integrating for 511 clock periods (25.6 μ s).

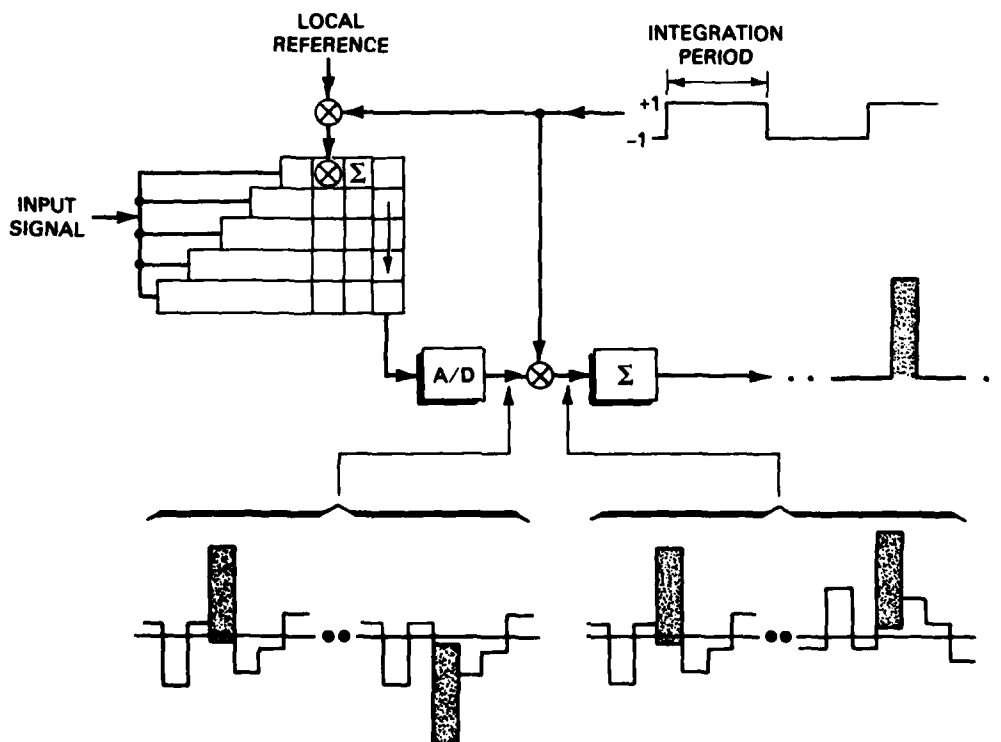


Figure 4-5. Illustration of a method of removing pattern noise arising from offsets.

digitized to 8 bits, and the two 32-sample segments of the upper trace were subtracted. The result was fed to a D/A converter and displayed as the lower trace. The correlation function can be seen to have the ideal shape, free of extraneous offsets.

B.E. Burke
D.L. Smythe
W.H. McGonagle



Figure 4-6. Experimental demonstration of pattern noise removal technique of Figure 4-5. Upper trace is CCD output of two successive integration periods. Lower trace is the result of subtracting the second half of the upper trace from the first half.

4.3 SUBMILLIMETER-WAVE MIXERS FOR SPACE APPLICATIONS

Many potential applications exist in remote sensing,¹⁰ atmospheric chemistry,¹¹ and astronomy¹² for aircraft or space-borne receivers at near-millimeter and submillimeter wavelengths. Although planar structures are the mixer configuration of choice for these severe environments because of their mechanical and electrical ruggedness, for the ultimate in receiver sensitivity one must at present rely on whisker-contacted diodes. Since the whisker point is generally held in place only by spring action and the spring force is limited so as not to damage the underlying Schottky diode, this arrangement is often fragile mechanically. The most successful near-millimeter-mixer structure to date is the corner reflector,¹³ shown in Figure 4-7, in which the whisker contacting the active device is typically 4 to 15 wavelengths long. Since the whisker serves as part of the antenna, it cannot be bent to some optimally stable shape (as has been done for encapsulated diodes for space use¹⁴) because the antenna pattern would be distorted.

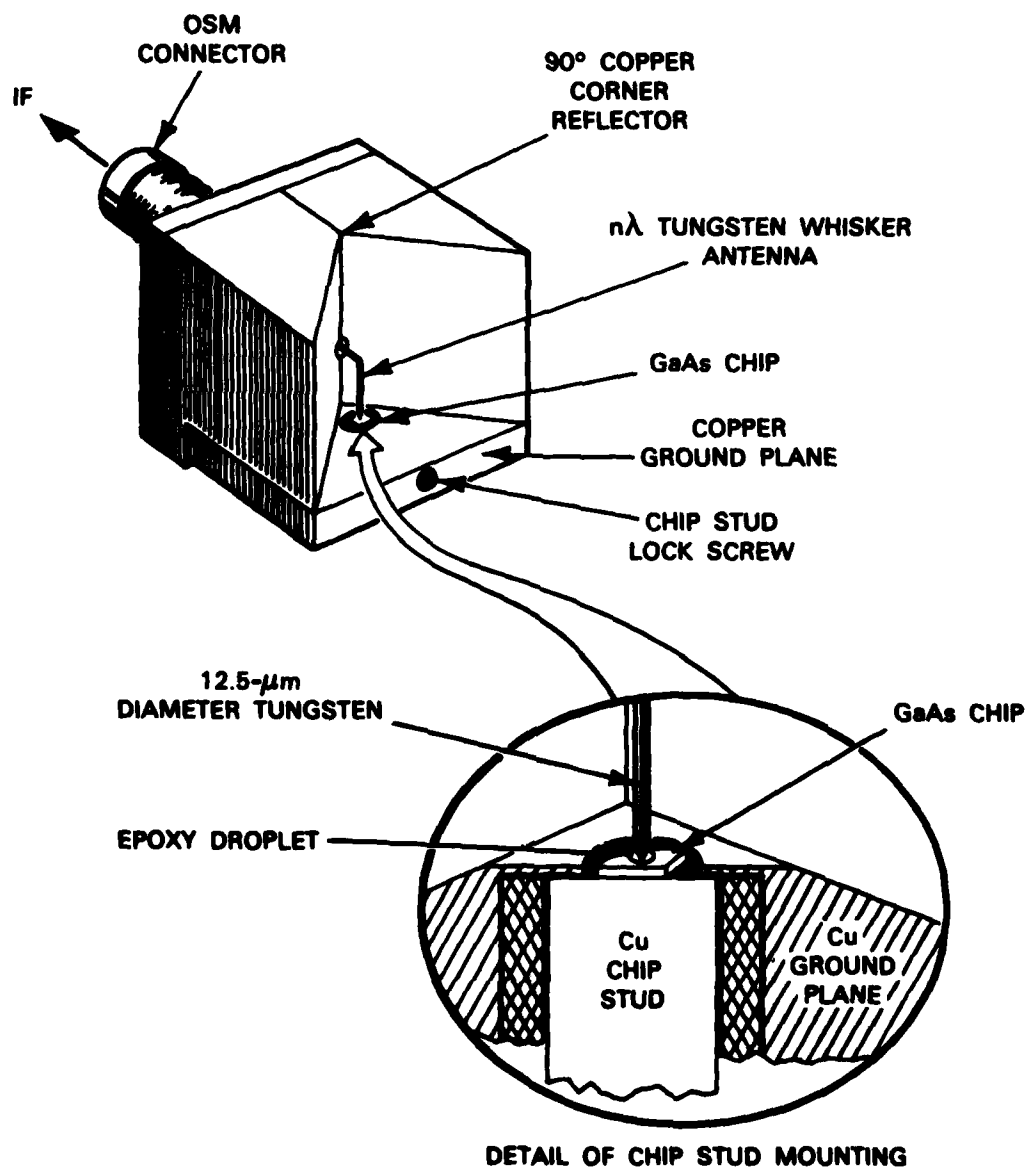


Figure 4-7. Corner reflector mixer showing location of nanoliter epoxy droplet bonding whisker antenna to GaAs chip.

We have developed a simple technique for ruggedizing the bond of the corner-cube whisker contact which does not affect mixer performance, at least up to 2.5 THz. The technique is based on a method worked out by Kerr¹⁵ for waveguide-mounted diodes at 115 GHz. A small drop (volume approximately 10 nl) of silica-loaded epoxy is placed on the whisker-chip interface after the device has been contacted. After a curing time of approximately 36 hours, the contact is firmly bonded. Mixer sensitivity does not change measurably due to this ruggedizing process.

Epoxy Technology* type H74 epoxy was obtained unfilled, and then filled just before using with an equal quantity by weight of Neosil-A powdered silica,[†] according to Reference 15. The 10 nl droplet was picked up and deposited using an applicator made of two tungsten wires with a 0.002-in. gap between them. The droplet was moved to the whisker and lowered until it contacted the chip. Typically the droplet covered about half of a 0.010-in.-square chip. Curing requires 24 hours at room temperature followed by 12 hours at 130°C. These and other details of this procedure are available in Reference 15. The labor involved in these steps is only a small fraction of the total mixer construction time.

One ruggedized device has been tested mechanically as well as electrically. The mechanical tests were vibration qualifications for a current satellite launch. They consisted of an rms load of 20.8 G with a spectrum which is flat between 100 and 1000 Hz and falls off at 6 dB/octave outside that spectral region. A nonruggedized corner reflector was tested simultaneously. Both devices survived to 14.8 G_{rms} , but the nonruggedized one failed at the full test rating of 20.8 G_{rms} in two of the three axes tested. The failure mode, as judged by monitoring the I-V curve, appeared to be hopping of the whisker on the chip surface. The ruggedized mixer passed the highest load tests in all three axes.

The electrical performance tests were made before and after the mixer was ruggedized. Voltage responsivity was measured at a wavelength of 432 μm to be 40 V/W and at 119 μm to be 6 V/W, and the receiver noise temperature was measured at 432 μm to be 12,000 K DSB. Within the 10- to 20-percent uncertainty in the measurements, no change in sensitivity could be found after the mixer was ruggedized. This result is somewhat surprising since the higher dielectric constant ($\epsilon_r \approx 4$) of the loaded epoxy should increase the whisker-to-chip fringing capacitance. However, perhaps this is compensated by the slightly inductive whisker.

One may expect these ruggedized devices to be stable to electrical overload due to the increased heat capacity of the loaded epoxy droplet, although we have not yet tested this. Devices which do fail electrically can be recontacted by removing the epoxy with epoxy stripper.

*Epoxy Technology, Inc., 14 Fortune Drive, P.O. Box 567, Billerica, MA 01821.

†Tammsco, Inc., 10 N. Front Avenue, Tamms, IL 62988.

In conclusion, we have demonstrated a procedure which brings space applications of sensitive near-millimeter receivers closer to reality. Although schemes of greater elegance could be envisioned, the method reported here is simple and achieves the desired results with little or no sacrifice in mixer sensitivity. The physically harsh environment in an aircraft or during space launch should no longer be a deterrent to the several near-millimeter wavelength applications.

T.C.L.G. Sollner
J.A. Taylor

4.4 CHARGE-COUPLED DEVICES: MATRIX-MATRIX PRODUCT DEVICE

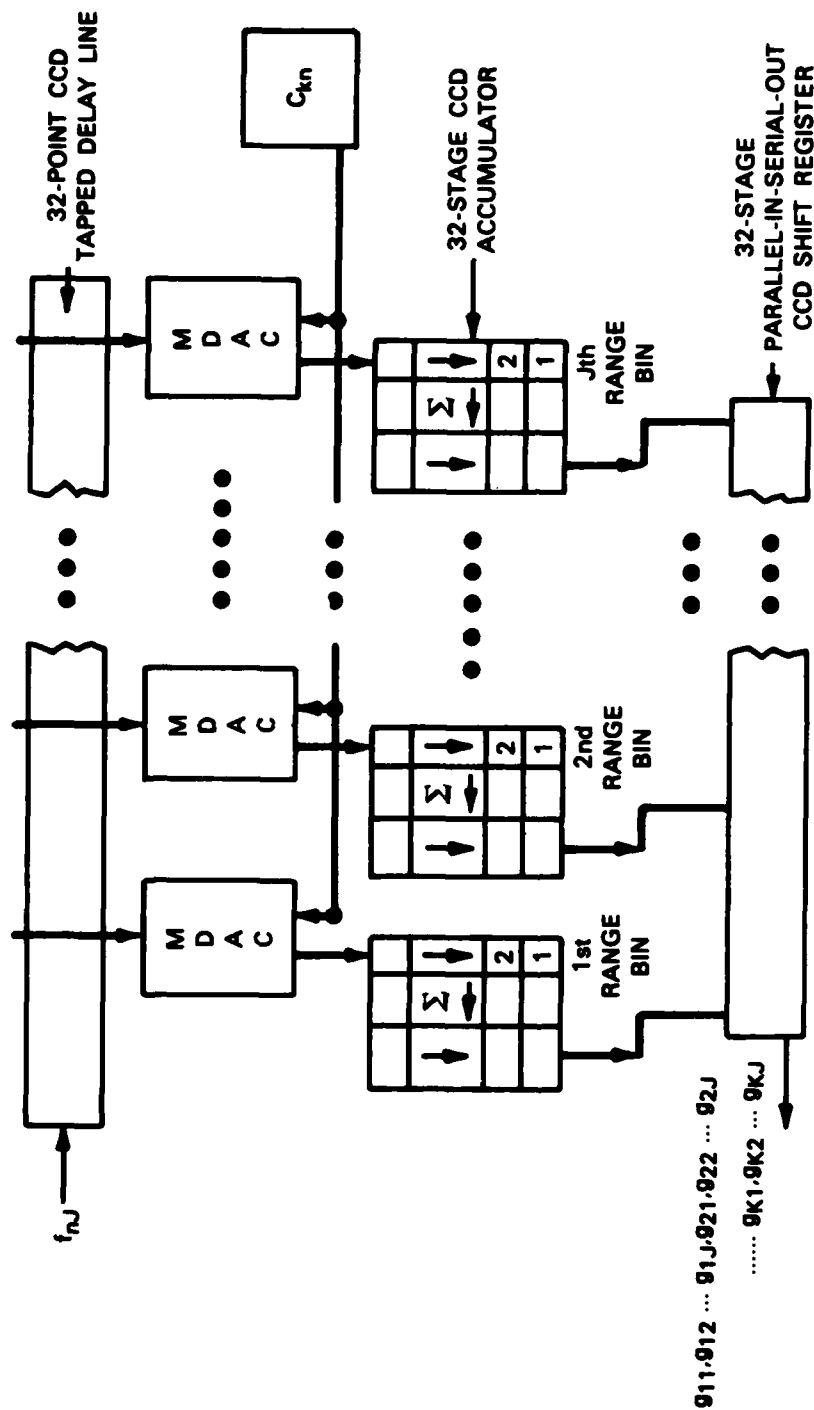
A single-chip CCD matrix-matrix product (MMP) device¹⁶ has been fabricated and evaluation begun. The chip can be used as a pulsed radar signal processor for 32 range bins, each with 32 Doppler resolution cells. A schematic of the MMP chip is shown in Figure 4-8. The device is capable of computing the function

$$g_{kj} = \sum_{n=0}^{31} c_{kn} f_{nj} \quad 0 \leq j \leq 31, 0 \leq k \leq 31$$

where f_{nj} are sampled analog data and c_{kn} are 8-bit digital words represented in 2's complement notation.

The chip includes a 32-stage CCD tapped delay line, 32 vector-matrix product (VMP) computing elements, 8 pairs of TTL-to-MOS buffer and inverting buffer, and a parallel-in serial-out (PISO) CCD output shift register. The tapped delay line shifts and holds analog sampled data. At each stage of delay the sample data are coupled to a corresponding VMP processor, and all the samples in the delay line are processed in parallel. A VMP computing element, which can be used as a single-range-bin Doppler processor, consists of an 8-bit, charge-domain, multiplying D/A converter (MDAC)¹⁷ and a 32-stage accumulating memory with separate input and output shift registers. Each pair of buffer and inverting buffer takes one bit of a TTL-level digital input word and generates an MOS-level bit word and the complement bit word which are the required digital input format to a CCD MDAC. The PISO CCD is used to reformat the output data stream. The sequential output data from each VMP device corresponds to a column vector of the G matrix. Since all the VMPs share common clocks, the column vectors of the G matrix are clocked out in parallel from the VMPs. These outputs can be read out of the chip directly or can be loaded in parallel into the CCD PISO device. In the latter case a serial output data stream with the elements of the G matrix can be read out sequentially row-by-row.

A photomicrograph of the chip is shown in Figure 4-9. The chip size is 8.4×8.4 mm. The device is a two-phase, buried-channel CCD with an implanted barrier and uses a double-polysilicon, double-metal process. For layout convenience two CCD floating-gate delay lines, tapped at even and odd stages, respectively, are used so the chip can be designed in a folded structure. The even-number range bin processor is located at the top of the device and the odd-number processor at the bottom.



$$9_{kj} = \sum_{n=1}^N f_{nj} w_{kn} \text{ FOR } 1 \leq N \leq 32, 1 \leq J \leq 32$$

Figure 4-8. Schematic of a general-purpose MMP device.

131100 S

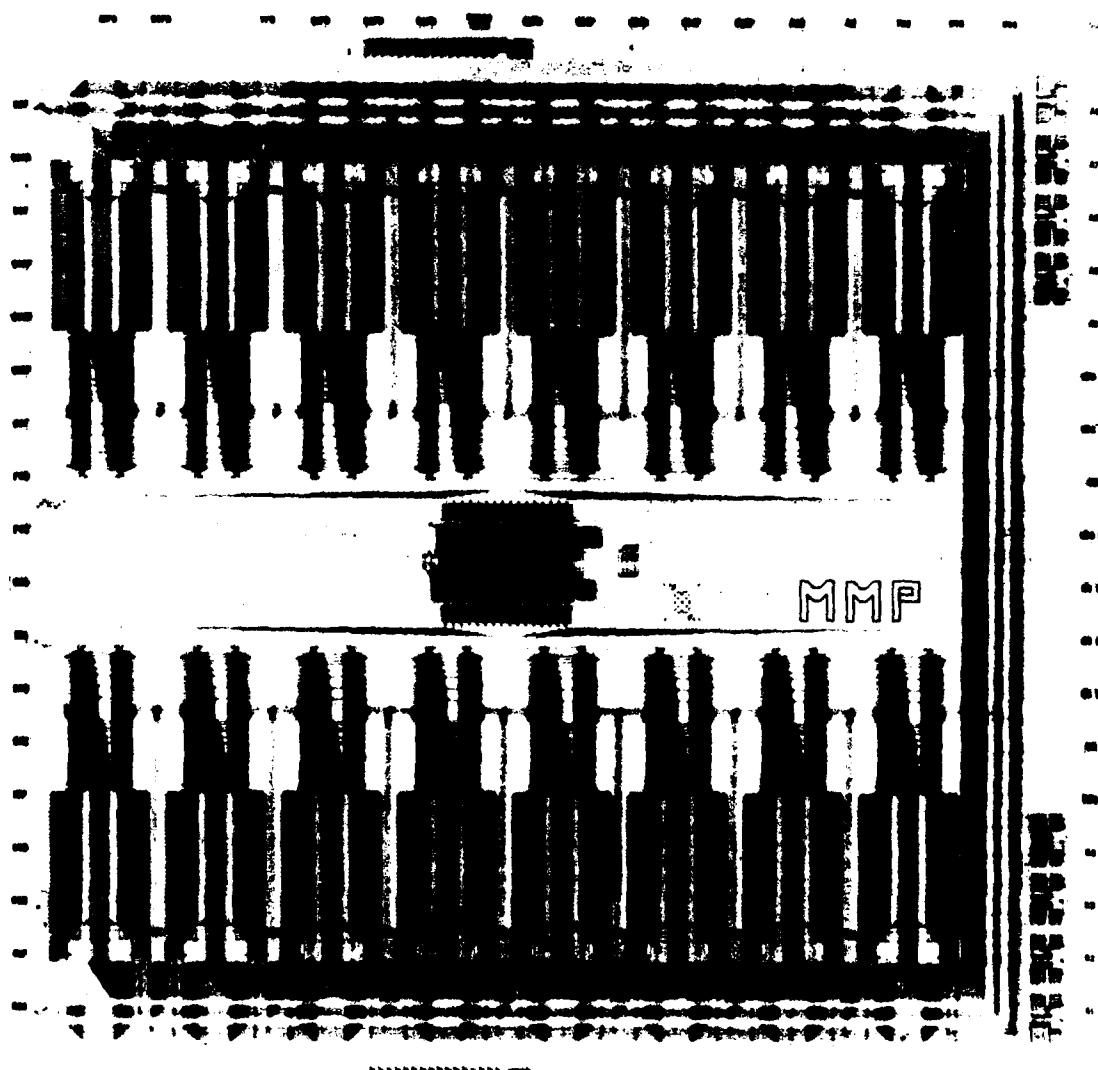
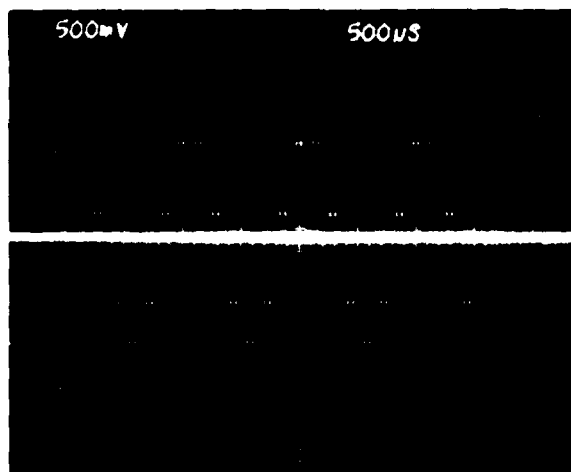
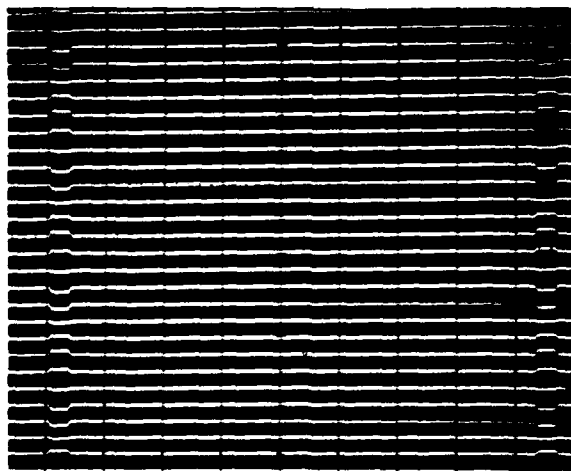


Figure 4-9. Photomicrograph of a CCD MMP device.



131101 S

Figure 4-10. Simulated serial radar video which consists of 28 returns, each to be sampled into 32 range-cell resolution. The waveform can be represented as $f_{nj} = -\cos(8\pi n/28)$ for $j = 4, j = 28$, and $0 \leq n \leq 27$; $f_{nj} = 0$ otherwise.



131102 S

Figure 4-11. The same video as in Figure 4-10 displayed in two-dimensional format, with the horizontal axis corresponding to range bins and the vertical axis to PRIs.

The device has been used to demonstrate Doppler processing in a simulated pulsed radar system. A simulated radar video is shown in Figure 4-10. The serial radar video consists of 28 returns, each to be sampled into 32 range-cell resolution. The pulse repetition interval (PRI) is 144 μ s. For illustrative purposes moving targets are placed in range bins 4 and 28. The input waveform is a 28 by 32 matrix and can be expressed as

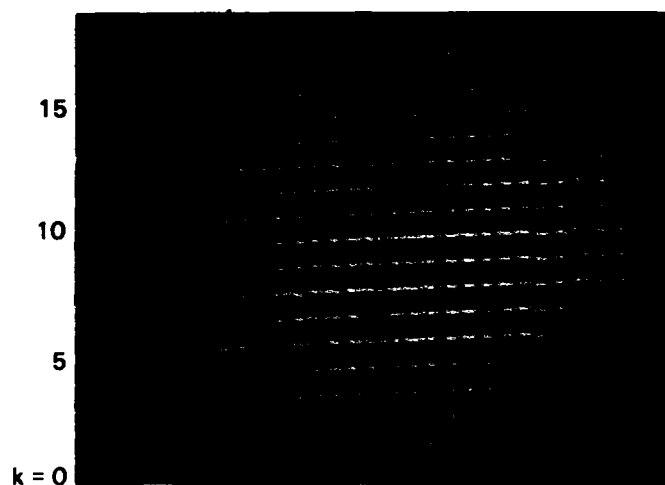
$$\begin{aligned} f_{nj} &= -\cos(8\pi n/28) && \text{for } j = 4 \text{ and } j = 28, 0 \leq n \leq 27 \\ f_{nj} &= 0 && \text{otherwise.} \end{aligned}$$

If the serial radar video is displayed in a two-dimensional format (i.e., the horizontal axis corresponds to range cells and the vertical axis to PRIs, as shown in Figure 4-11), the moving targets in the above-mentioned range bins are clearly indicated.

When the simulated radar video shown in Figure 4-10 is applied to the CCD MMP chip, the CCD tapped delay line takes 32 samples and then processes them in parallel during each PRI. For this demonstration the experiment was performed at wafer level at a CCD sampling rate of 500 kHz. After 28 pulse returns the device performs 28-point, real discrete Fourier transforms on each of the 32 range-bin samples, and the results are stored in the 32 VMPs. It should be noted that we have used a real, symmetric input waveform, with the result that a pure discrete cosine transform yields the desired spectral information.

At this point in the processing, the spectral information of all the range bins for a given Doppler cell can be parallel loaded into the CCD PISO and read out sequentially. Since the output from the CCD PISO is a serial data stream, it also can be displayed in a two-dimensional format. If the horizontal display axis is chosen to represent the range cells and the vertical axis the Doppler cells, the output from the device is of the form shown in Figure 4-12, clearly demonstrating that there are two moving targets in range cells 4 and 28 with a Doppler shift of $k = 4$. The false targets shown in the output of the device are the result of fixed-pattern noise caused by fabrication problems. Another run of MMP wafers is being processed, and improved device performance is expected.

A.M. Chiang



131103-S

Figure 4-12. Discrete cosine transform of the input waveform shown in Figure 4-10, computed by the MMP device. Serial output data stream from the device is displayed in two-dimensional format (i.e., the horizontal axis corresponds to range bin resolution and the vertical axis to Doppler resolution).

REFERENCES

1. J.W. Beams, in *Structure and Properties of Thin Films*, C.A. Neugebauer, J.B. Newkirk, and D.A. Vermilyea, Eds. (Wiley and Sons, New York, 1959), pp. 183-192.
2. R.J. Jaccodine and W.A. Schlegel, *J. Appl. Phys.* **37**, 2429 (1966).
3. M. Sekimoto, H. Yoshihara, and T. Ohkubo, *J. Vac. Sci. Technol.* **21**, 1017 (1982).
4. J.N. Randall, D.C. Flanders, N.P. Economou, J.P. Donnelly, and E.I. Bromley, *Appl. Phys. Lett.* **42**, 457 (1983).
5. A.K. Sinha, H.J. Levinstein, and T.E. Smith, *J. Appl. Phys.* **49**, 2428 (1978).
6. Solid State Research Report, Lincoln Laboratory, M.I.T. (1981:3), pp. 45-49, DTIC AD-A112696/0.
7. *Ibid.* (1982:2), pp. 59-63, DTIC AD-A122252.
8. *Ibid.* (1982:3), pp. 55-58, DTIC AD-A124305/4.

9. D.L. Smythe and R.W. Ralston, "An Improved SAW Time-Integrating Correlator with CCD Readout," in *1980 Ultrasonics Symposium Proceedings* (IEEE, New York, 1980), pp. 14-17, DTIC AD-A102977/6.
10. M.M. Litvak, J.A. Weiss, and G.F. Dionne, *Intl. J. Infrared and Millimeter Waves* 1, 561 (1980), DTIC AD-A101149/3.
11. J.L. Bufton, private communication; and J.W. Waters and S.C. Wofsy, *Final Report of the NASA Committee on High Resolution Passive Microwave Satellite Systems*, D.H. Staelin, Chairman, Chapter 7 (1978).
12. D. Buhl, "Sub-Millimeter Wave Astronomy Research and Technology," to be published.
13. H.R. Fetterman, P.E. Tannenwald, B.J. Clifton, C.D. Parker, W.D. Fitzgerald, and N.R. Erickson, *Appl. Phys. Lett.* 33, 151 (1978).
14. F.J. Solman, C.D. Berglund, R.W. Chick, and B.J. Clifton, *J. Spacecraft and Rockets* 16, 181 (1977).
15. A.R. Kerr, R.J. Mattauch, J.A. Grange, and K. Schrubba, "A Microwave Diode Package for Millimeter and Submillimeter Wavelength Detectors," Internal Report, NASA Institute for Space Studies, New York, NY 10025.
16. A.M. Chiang, "A New CCD Parallel Processing Architecture," in *CMU Conference on VLSI Systems and Computations*, H.T. Kung, B. Sproull, and G. Steele, Eds. (Computer Science Press, Rockville, Maryland, 1981), pp. 408-418.
17. A.M. Chiang and B.E. Burke, "A High-Speed Digitally Programmable CCD Transversal Filter," 1980 GOMAC Digest of Papers, pp. 182-183.

5. ANALOG DEVICE TECHNOLOGY

5.1 SUPERCONDUCTIVE RING MIXERS

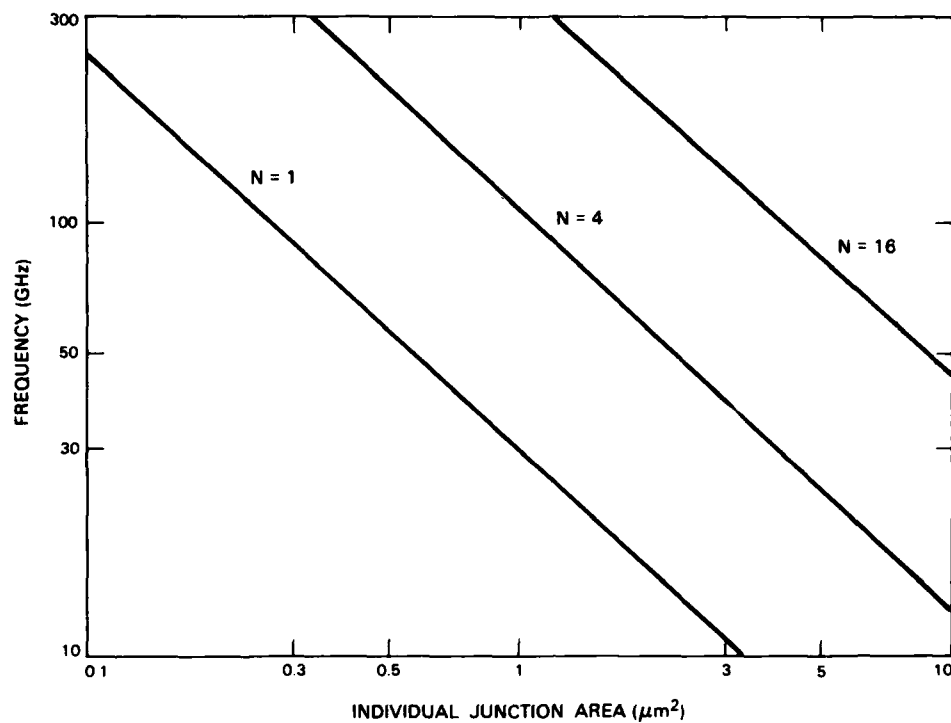
Superconductive tunnel junctions provide the essential nonlinear mixing interaction in programmable wideband analog superconductive signal-processing devices.¹ Single junction configurations have been employed in a preliminary convolver² and as high-frequency mixers.³ Superconductive mixers characteristically suffer from very low saturation levels. The saturation is observed as a smoothing of the tunneling nonlinearity and occurs for potentials across the junction of more than about 1 mV. The preliminary convolver had limited dynamic range because of this junction saturation. By connecting a number N of junctions in series, one can increase the saturation power P_s by N^2 . The mixer configuration used is actually a ring with a series array of four junctions in each of the four sections of the ring. The properties of these superconductive mixers result in improved multipliers for signal-processing devices.

Consider the cutoff frequency of the mixer. The superconductive tunnel junction can be modeled as a nonlinear tunneling resistance R_n in parallel with a parasitic junction capacitance C_j . In high-frequency mixer applications without inductive tuning, as in structures like the convolver, the time constant $R_n C_j$ is the limiting factor in the frequency response. Capacitance values of $13.4 \mu\text{F}/\text{cm}^2$ have been measured for tunnel junctions⁴ with niobium-oxide barriers having current densities J_n of about $10^3 \text{ A}/\text{cm}^2$. Because the capacitance is a slower function of the barrier thickness t than is J_n (and resistance), this time constant can be reduced by decreasing t . Thin barriers (J_n of up to $10^5 \text{ A}/\text{cm}^2$) have been achieved at Lincoln Laboratory⁵ and elsewhere. However, high current densities can only be obtained in devices with low resistance-area products. To provide adequate impedances for many RF applications, junction dimensions must be shrunk to submicrometer dimensions. Stacking N junctions in series is an alternative method of increasing the RF impedance. This is portrayed in Figure 5-1, where the time-constant-limited response of niobium-based junction arrays is plotted as a function of individual junction area. Array impedance was held at a convenient 50Ω .

To increase the available output power, maintain impedance, and to provide partial suppression of undesired spurious products in the programmable analog signal-processing devices, the ring-mixer structure shown in Figure 5-2 has been developed. The ring mixer has two RF input ports, a single output port, and a DC bias port. Each of its legs has several superconductive tunnel junctions in series.

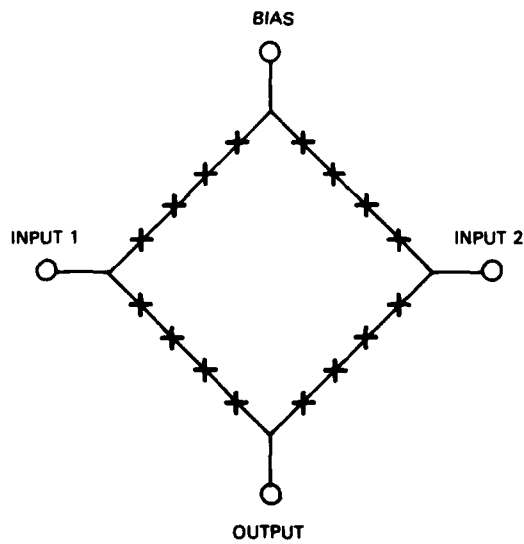
A photograph of a recently fabricated superconductive diode ring is shown in Figure 5-3. The structure has a series array of four tunnel junctions in each of its four legs. The junctions consist of a niobium base electrode, a niobium-oxide tunnel barrier, and a lead counterelectrode.⁵ Junction areas are defined by $4\text{-}\mu\text{m}$ -dia. windows etched in a silicon monoxide insulation layer. Signals are coupled into and out of the diode ring through microstrip transmission lines. Stray RF currents on the bias line are shunted through pad-type capacitors to an underlying ground plane.

The current-voltage characteristic of a diode ring mixer is shown in Figure 5-4. This characteristic was obtained by ramping the DC current flow between the bias and output



131104-N

Figure 5-1. Cutoff frequency of 50- Ω mixer rings as a function of individual superconductive junction area.



120066-N-01

Figure 5-2. Schematic of the diode mixer ring.

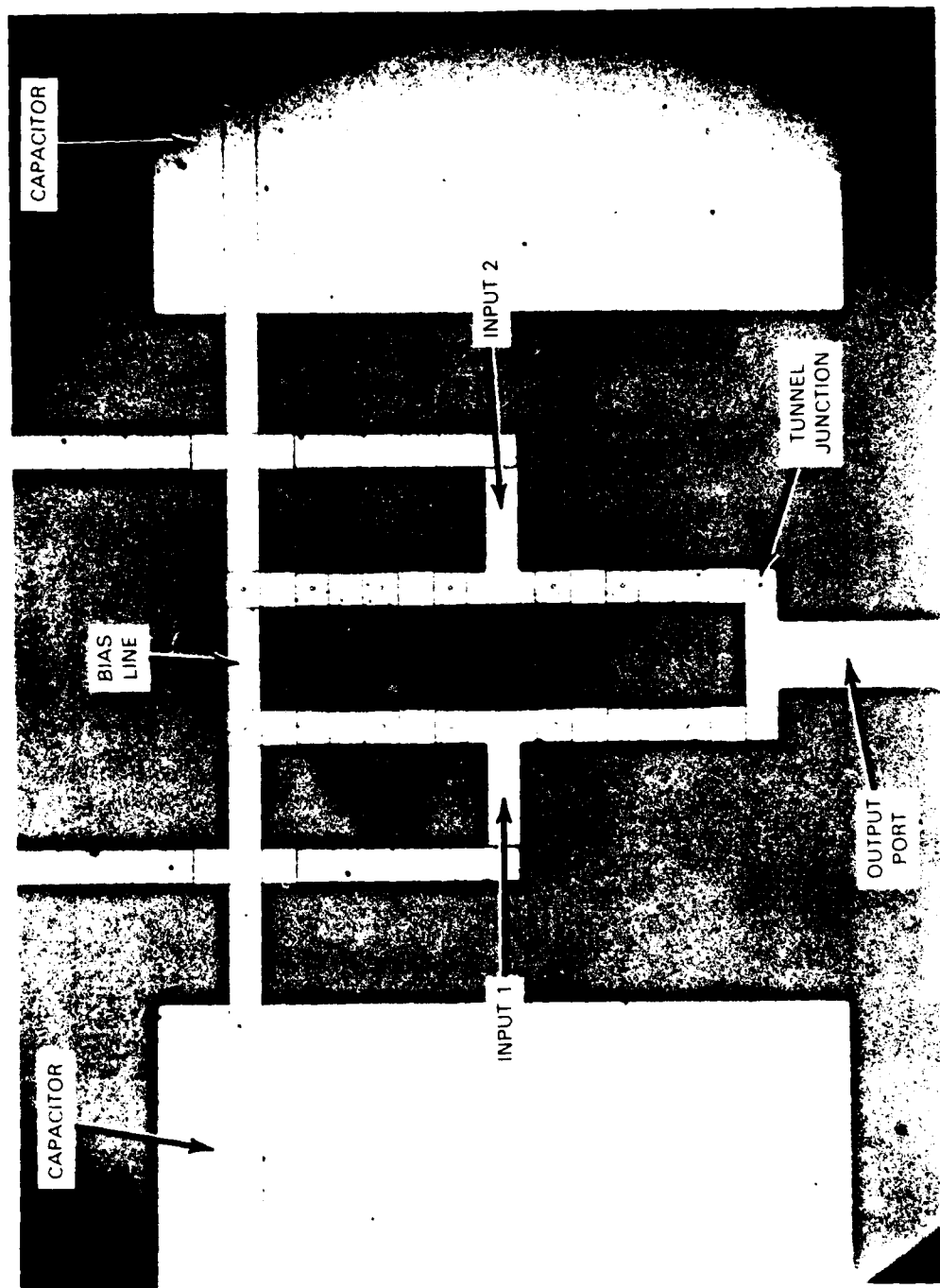
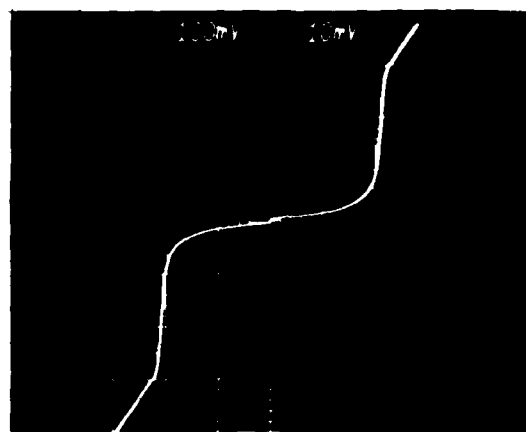
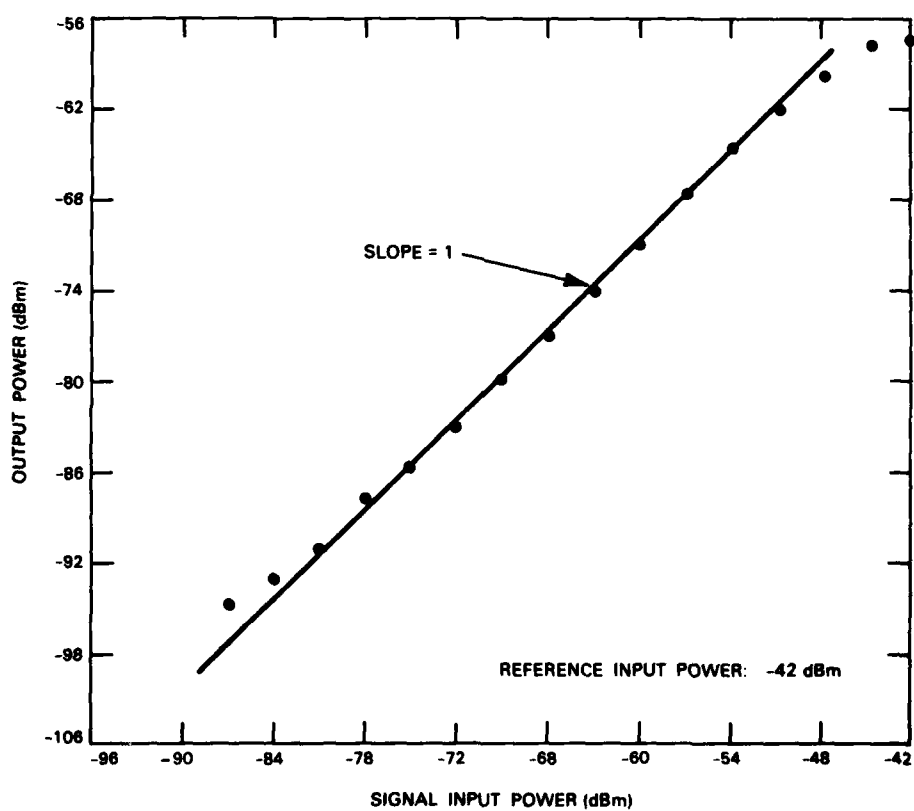


Figure 5-3. Photograph of a 16-junction diode mixer ring.



131106 S

Figure 5-4. Current-voltage characteristic of a 16-junction ring mixer at 4.2 K. Horizontal scale is 10 mV/div; vertical scale is 0.1 mA/div.



131107 N

Figure 5-5. Diode ring output level as a function of input signal level.

ports while observing the potential across these same ports. At DC the RF input ports are effectively open-circuited; thus with this test configuration there are two series arrays of eight junctions each, in parallel. The sharp nonlinearity which occurs at a potential of about 22 mV is due to the tunneling of normal electrons. The Josephson (superelectron tunneling) current, which normally appears with zero potential across the tunnel barrier, was suppressed intentionally with a strong magnetic field. The individual junctions in this array had a normal impedance of about 18Ω and a gap voltage of about 2.7 mV.

RF measurements made on the diode ring structure confirm our projections for saturation and efficiency. In operation, a current source is applied between the bias and output ports to bias the ring at ~ 22 mV in order to obtain efficient mixing. The RF signal $s(\omega t)$ and RF reference $r(\omega t)$ are introduced into both input ports, at one as $s(\omega t) + r(\omega t + \phi)$, at the other as $s(\omega t + \phi) + r(\omega t)$. The desired cross product $s \cdot r(2\omega t + \phi)$ between the signal and reference is formed in the two lower sections of the ring structure and appears at the output port. As described in detail elsewhere,¹ by choosing the phase shift ϕ between the two input ports to be 90° , the largest spurious products are suppressed: $s^2(2\omega t)$ cancels $s^2(2\omega t + 180^\circ)$ and $r^2(2\omega t)$ cancels $r^2(2\omega t + 180^\circ)$.

The measured output power level of a diode ring mixer as a function of input signal power for fixed reference power is plotted in Figure 5-5. With the nominal 12-dB improvement in saturation levels, output power levels of -60 dB are now obtained. Measured efficiency is within 4 dB of theoretical predictions. Incorporation of these mixer rings into an improved superconductive convolver will be described in a subsequent report.

S.A. Reible
E.M. Macedo

5.2 CONVOLVER-BASED WIDEBAND PROGRAMMABLE MATCHED FILTER

A 200-MHz-bandwidth programmable matched filter subsystem based on an acoustoelectric convolver has been designed, built, and tested. The convolver structure is of the air-gap type developed at Lincoln Laboratory.^{6,7} Electric fields accompanying counterpropagating acoustic waves on the surface of a LiNbO_3 piezoelectric delay line are mixed and integrated in a Si strip held in proximity (~ 300 nm) to the delay line surface. The device can be used as a programmable matched filter by providing a reference waveform which is the time-reversed replica of the signal to be filtered. Important advantages are gained through the use of a convolver as a matched filter. Continuous spreading of the transmitted spectrum over a wide bandwidth using pseudonoise (PN) codes reduces the jamming sensitivity and lowers the probability of intercept. Although not yet implemented in this subsystem, encoding waveforms can be changed from pulse burst to pulse burst, thus further reducing jamming sensitivity and increasing security. Additionally, nonrepeated codes eliminate range ambiguities in radar systems and reduce multipath degradation in communication systems.

The subsystem combines the convolver with a newly constructed waveform generator, which consists of a digital code generator and a minimum-shift-keyed (MSK) modulator. The code generator, built with emitter coupled logic, operates on a 200-MHz clock to produce a 5.12- μ s-long, 1023-chip PN code.

A maximal-length (M) sequence was selected as the code because it is easily produced with shift registers and has well-defined time sidelobe properties.⁸ The code generation scheme is shown in Figure 5-6. An n-chip shift register with feedback from flip-flop stages k and n produces a code containing $2^n - 1$ chips.

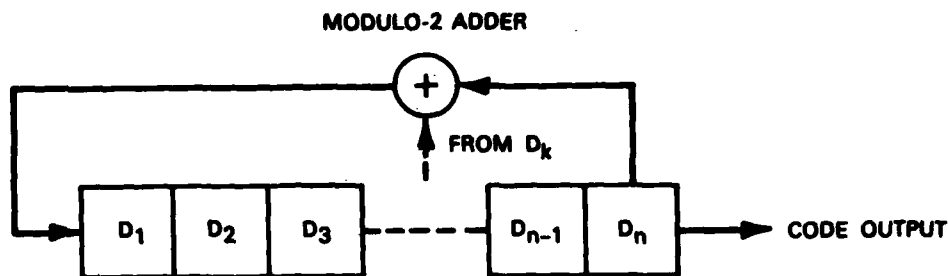


Figure 5-6. Code sequence generator.

The code is impressed onto a carrier through MSK modulation. MSK is a spectrally efficient modulation technique, with more than 99.5 percent of the signal energy contained between the first two nulls of its spectrum as compared to 92 percent of phase-shift-keyed (PSK) waveforms.⁹ In addition, it is less sensitive to quadratic phase errors than PSK since transitions between successive chips are separated by 90° rather than 180° .¹⁰ The MSK modulation scheme is shown in Figure 5-7. To implement the modulation, the code is first separated into odd and even chip streams. Each odd chip is gated through one flip flop while each even chip is gated through another. These information streams are used to phase modulate two signals, a cosine-modulated cosine and a sine-modulated sine, which are then summed.

Convolution of a 1023-chip M sequence should produce a peak-to-sidelobe ratio of 60 dB. However, this assumes spatial integration within the convolver of precisely 1023 chips. In the convolver used, the Si electrode length was $6 \mu\text{s}$ long while the code length is $5.12 \mu\text{s}$. This implies that an extra 177 chips are present, which translates to a degradation of 22.5 dB in the peak-to-sidelobe ratio. Thus, a peak-to-sidelobe ratio of 37.5 is expected.

As shown in Figure 5-8, a clean compressed pulse was obtained. The 3-dB width of the pulse in Figure 5-8(a) is 5 ns, and is consistent with the 200-MHz bandwidth of the waveform. The low time sidelobes are seen in Figure 5-8(b).

The equivalent rms power levels of the peak and the sidelobes were estimated as follows. A CW signal at the output carrier frequency of 1 GHz was substituted for the correlation spike to produce an equivalent deflection on the oscilloscope and then measured with a power meter. The sidelobe power was measured directly with the meter. Here care

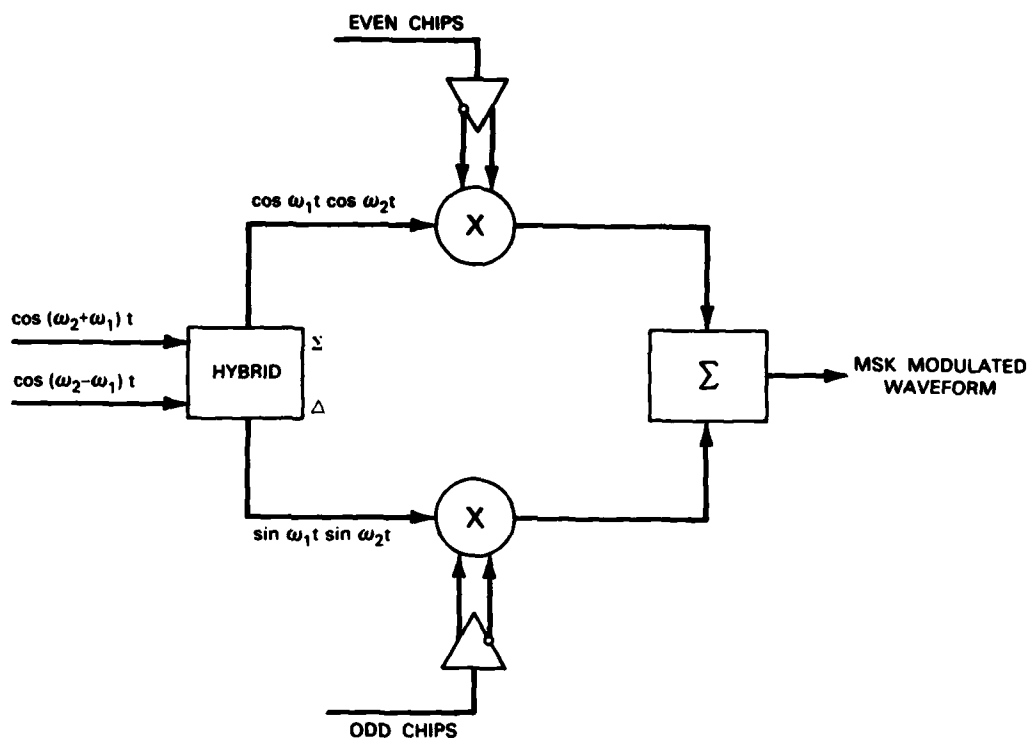


Figure 5-7. Minimum-shift-keyed modulator.

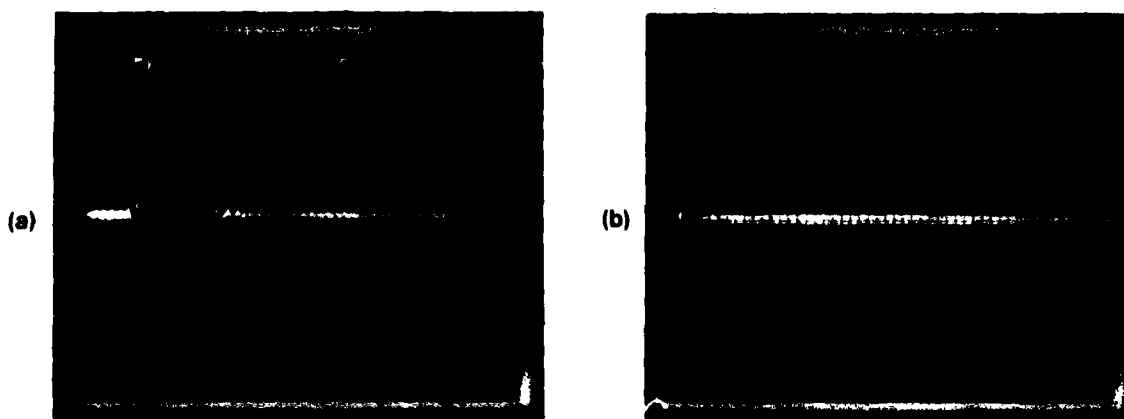


Figure 5-8. Compressed pulse output of convolver. Horizontal scale: (a) 5 ns/div. (b) 50 ns/div.

was taken to minimize the contribution of the correlation spike by choosing the output amplifier gain such that the peak saturated at a level only slightly above the sidelobe level. The estimated peak-to-sidelobe ratio is 35 dB. The difference between the expected ratio of 37.5 dB and that measured is believed to be attributable partly to implementation loss and partly to a roll-off in the response of the oscilloscope.

This programmable matched filter will now be integrated with additional modules in order to form a Doppler radar processor. One module will contain an electrooptic sample-and-hold circuit. The sampler will format the convolver output for subsequent processing in a module containing unique charge-coupled devices.

E.M. Hauser

REFERENCES

1. S.A. Reible, *1982 Ultrasonics Symposium Proceedings* (IEEE, New York, 1982), pp. 190-201.
2. Solid State Research Report, Lincoln Laboratory, M.I.T. (1983:1), p. 89, DTIC AD-A128894.
3. *Ibid.* (1981:3), p. 26, DTIC AD-A112696/0.
4. J.H. Magerlein, *IEEE Trans. Magn.* 17, 286 (1981).
5. Solid State Research Report, Lincoln Laboratory, M.I.T. (1983:2), p. 58.
6. I. Yao and S.A. Reible, *1979 Ultrasonics Symposium Proceedings* (IEEE, New York, 1979), pp. 701-705, DTIC AD-A090252/8.
7. Solid State Research Report, Lincoln Laboratory, M.I.T. (1980:1), p. 49, DTIC AD-A089822/1.
8. R.C. Dixon, *Spread Spectrum Systems* (Wiley and Sons, New York, 1976), p. 54.
9. J. Goll, *IEEE Trans. Microwave Theory Tech.* 29, 473 (1981).
10. S. Pasupathy, *IEEE Commun. Mag.* 17, 14 (1979).

UNCLASSIFIED

SECURITY CLASSIFICATION OF THIS PAGE (When Data Entered)

REPORT DOCUMENTATION PAGE		READ INSTRUCTIONS BEFORE COMPLETING FORM
1. REPORT NUMBER ESD-TR-83-051	2. GOVT ACCESSION NO. AD - A140027	3. RECIPIENT'S CATALOG NUMBER
4. TITLE (and Subtitle) Solid State Research	5. TYPE OF REPORT & PERIOD COVERED Quarterly Technical Summary 1 May - 31 July 1983	6. PERFORMING ORG. REPORT NUMBER 1983:3
7. AUTHOR(s) Alan L. McWhorter	8. CONTRACT OR GRANT NUMBER(s) F19622-80-C-0002	
9. PERFORMING ORGANIZATION NAME AND ADDRESS Lincoln Laboratory, M.I.T. P.O. Box 73 Lexington, MA 02173-0073	10. PROGRAM ELEMENT, PROJECT, TASK AREA & WORK UNIT NUMBERS Program Element No. 63250F Project No. 649L	
11. CONTROLLING OFFICE NAME AND ADDRESS Air Force Systems Command, USAF Andrews AFB Washington, DC 20331	12. REPORT DATE 15 August 1983	13. NUMBER OF PAGES 120
14. MONITORING AGENCY NAME & ADDRESS (if different from Controlling Office) Electronic Systems Division Hanscom AFB, MA 01731	15. SECURITY CLASS. (of this report) Unclassified	15a. DECLASSIFICATION/DOWNGRADING SCHEDULE
16. DISTRIBUTION STATEMENT (of this Report) Approved for public release; distribution unlimited.		
17. DISTRIBUTION STATEMENT (of the abstract entered in Block 20, if different from Report)		
18. SUPPLEMENTARY NOTES None		
19. KEY WORDS (Continue on reverse side if necessary and identify by block number)		
solid state devices	photodiode devices	surface-wave transducers
quantum electronics	lasers	charge-coupled devices
materials research	imaging arrays	acoustoelectric devices
microelectronics	LIDAR system	waveguide structures
analog device technology		
20. ABSTRACT (Continue on reverse side if necessary and identify by block number)		
<p>This report covers in detail the solid state research work of the Solid State Division at Lincoln Laboratory for the period 1 May through 31 July 1983. The topics covered are Solid State Device Research, Quantum Electronics, Materials Research, Microelectronics, and Analog Device Technology. Funding is primarily provided by the Air Force, with additional support provided by the Army, DARPA, Navy, NASA, and DOE.</p>		

DD FORM 1473 EDITION OF 1 NOV 65 IS OBSOLETE
1 Jan 73

UNCLASSIFIED

SECURITY CLASSIFICATION OF THIS PAGE (When Data Entered)

ND

DATE

LMED

-84

TIC